



SAPIENZA
UNIVERSITÀ DI ROMA



Faculty of Mathematical, Physical and Natural Sciences
Department of Earth Sciences

Landslide damming: implications for natural hazards and risks

PhD Candidate: Javad Rouhi
Cycle: XXXII
Curriculum: Geosciences

Tutor: Professor Salvatore Martino
Co-Tutor: Professor Marta Della Seta

Acknowledgement

Completion of this doctoral dissertation was possible with the scientific and spiritual supports of several individuals. I would like to express my sincere gratitude to all of them.

I am extremely grateful to my tutor Prof. Salvatore Martino and co-tutor Prof. Marta Della Seta who have been tremendous mentors for me. I would like to thank them for all their supports, patience with me during our regular meetings and all the great scholarly comments and suggestions for my thesis and for allowing me to grow as a researcher all along the way.

I would like to thank Mr. Luigi Marino for his great support during the laboratory tests.

I would like to thank the manager and staffs of Forest, Range & Watershed Organization of Pol-e-Dokhtar, Eng. Shahram Mir Rezai, Eng. Soleimani for their great supports and collaboration during my field survey in Pol-e-Dokhtar and their disponibility.

I would also like to thank my brother Dr. Jafar Rouhi for all his supports.

Finally, this thesis is dedicated to my father and my mother, whose encouragement made me motivated to reach a fruitful end in my studies. My heartfelt thanks are for all the sacrifices that they have made on my behalf.

Table of Contents

List of Figures	5
List of Tables	7
List of Equation	8
Abstract	9
Introduction	11
Chapter 1- State of the art	13
1.1 Landslide damming	13
1.2 Seymareh landslide	18
Chapter 2- Geological setting	21
2.1 Stratigraphic and Geo-structural features	21
2.2 Geomorphological features	26
Chapter 3- Morphometric analysis	48
3.1 Material and methods	48
3.2 Results	68
Chapter 4- Soil properties of the landslide debris	74
4.1 Introduction	74
4.2 Grain size analysis	75
4.2.1 Photographic technique	75
4.2.2 Classification based on USCS standard (D2487-17)	78
4.2.3 Statistical classification	79
4.3 In-situ density (D2167-15) and permeability tests (D2434-68)	82
4.4 Results	87
4.4.1 USCS classification	87
4.4.2 Statistical classification	89
4.4.3 Permeability tests	92
Chapter 5- Geological model of the landslide debris	95
5.1 Material and methodology	95

5.2 Results	104
Chapter 6- Discussion	105
Chapter 7- Conclusions	114
References	116
Web Site References	126
Annex A	127

List of Figures

FIGURE 1 LANDSLIDE DAM TYPES I–VI BY COSTA AND SCHUSTER 1988 AND NEW PROPOSED DAM TYPES BY HERMANNS ET AL. 2011	14
FIGURE 2 GEOLOGICAL MAP OF THE SEYMAREH LANDSLIDE AREA	22
FIGURE 3 CROSS SECTIONS ACROSS THE SEYMAREH LANDSLIDE DEBRIS ACCORDING TO THE REVISED STRATIGRAPHIC COLUMN FOR THE SEYMAREH RIVER VALLEY	23
FIGURE 4 EARTHQUAKE EPICENTER & MAJOR FAULTS MAP OF LORESTAN & ILAM, MAP N.12-B (COLLECTED BY DEZVARE, M., NASERIEH, S., ROUHI, A & BOROMAND, B. 2015) INSTITUTE OF GEOPHYSICS, IRANIAN SEISMOLOGICAL CENTER (IRSC)	25
FIGURE 5 MAIN MORPHO-STRUCTURES IN THE STUDY AREA	26
FIGURE 6 OMBRO-THERMIC CURVE OF POL-E-DOKHTAR	28
FIGURE 7 THE POL-E-DOKHTAR AND DARREH-SHAHR WATERSHEDS	29
FIGURE 8 MECHANICAL WEATHERING	31
FIGURE 9 CHEMICAL WEATHERING	32
FIGURE 10 BIOLOGIC WEATHERING	33
FIGURE 11 WATER EROSION	33
FIGURE 12 HEADWARD EROSION	34
FIGURE 13 GULLY EROSION	35
FIGURE 14 FLOOD EROSION	36
FIGURE 15 BAHRAM CHUBIN GORGE	37
FIGURE 16 GORGES	37
FIGURE 17 CLIFFS DUE TO THE DETACHMENT OF A PART OF THE ASMARI FORMATION	38
FIGURE 18 FLOOD PLAIN	39
FIGURE 19 ALLUVIAL DEPOSIT ON THE SEYMAREH LANDSLIDE DEBRIS	40
FIGURE 20 THE LACUSTRINE DEPOSIT OF THE SEYMAREH LAKE	41
FIGURE 21 ALLUVIAL FANS ON THE SEYMAREH LANDSLIDE DEBRIS	42
FIGURE 22 DENUDATION SCARP ON THE LANDSLIDE DEBRIS	42
FIGURE 23 RIDGES ON THE SEYMAREH LANDSLIDE DEBRIS	43
FIGURE 24 SPRINGS AND LAKES LOCATION	44
FIGURE 25 EXTENSIONAL TRENCHES ON THE LANDSLIDE DEBRIS	46
FIGURE 26 EXTENSIONAL TRENCHES ON THE LANDSLIDE DEBRIS	46
FIGURE 27 EXTENSIONAL TRENCHES ON THE LANDSLIDE DEBRIS	47
FIGURE 28 FLOW CHART ILLUSTRATING THE STRUCTURE OF THE SPECIFICALLY DESIGNED GEODATABASE	50
FIGURE 29 SCHEME OF HOW THE LINE DENSITY TOOL OPERATES	51
FIGURE 30 SCHEME OF HOW THE POINT DENSITY TOOL OPERATES	52
FIGURE 31 SCHEME OF HOW THE AGGREGATE TOOL OPERATES	53
FIGURE 32 THE LANDSLIDE DEBRIS ZONATION BASED ON THE TONE, TEXTURE AND STRUCTURE OF THE AERIAL PHOTOS	54
FIGURE 33 FLOWCHART SHOWING THE HERE ADOPTED PROCEDURE FOR RECOGNITION OF PRIMARY OR SECONDARY REGION	57
FIGURE 34 EXAMPLES OF ZONES WITH DIFFERENT EVIDENCES FOR PRIMARY CONDITIONS DEDUCED BY CONSIDERING DIFFERENT LANDFORM ASSOCIATIONS	60
FIGURE 35 EXAMPLES OF ZONES WITH DIFFERENT EVIDENCES FOR SECONDARY CONDITIONS DEDUCED BY CONSIDERING DIFFERENT LANDFORM ASSOCIATIONS	60
FIGURE 36 ZONATION OF ORIGINAL (PRIMARY) AND RESHAPED (SECONDARY) REGIONS OF THE SEYMAREH LANDSLIDE DEBRIS AND RELATED PROBABILITY	65
FIGURE 37 GRAPHICAL VIEW OF THE AZIMUTHAL DISTRIBUTION OF THE KINEMATIC INDICATORS FOR EACH CLASS	67

FIGURE 38 GEOMORPHOLOGICAL MAP INCLUDING THE MAIN LANDFORMS SURVEYED WITHIN THE DEBRIS OF THE SEYMAREH LANDSLIDE	68
FIGURE 39 RIDGES DENSITY ZONATION	69
FIGURE 40 GULLIES DENSITY ZONATION	70
FIGURE 41 BLOCKS DENSITY ZONATION	72
FIGURE 42 WATERSHED AND LONGEST FLOW PATHS	73
FIGURE 43 THE FULL IMAGE TO BE ANALYZED ON THE WORKING SURFACE OF THE BASEGRAIN SOFTWARE	75
FIGURE 44 FINAL RESULT OF AUTOMATIC OBJECT DETECTION PROCEDURE. STRAIGHT LINES (COLOR PRINT: BLUE) REPRESENT A-AXIS AND B-AXIS OF ELLIPSES FITTED TO EACH OBJECT USING NORMALIZED SECOND CENTRAL MOMENTS OF DETERMINED OBJECT AREAS. PIXELS OF GRAIN BOUNDARIES ARE HIGHLIGHTED (COLOR PRINT: RED). GRAINS WITH CONTACT TO ENCLOSING FRAME ARE BLANKED OUT. FIRST ESTIMATION OF FRACTIONAL WEIGHTED MEAN DIAMETER D_m IS GIVEN AT BASELINE INFORMATION BAR.	77
FIGURE 45 EFFECT OF INTERACTIVE POST-PROCESSING ON PRECISION OF OBJECT DETECTION PROCEDURE. LEFT: AFTER POST-PROCESSING, RIGHT: BEFORE POST PROCESSING.	78
FIGURE 46 GRAPH OF D10-D60 OF SOIL SAMPLES IN THE ASMARI FORMATION DEBRIS	79
FIGURE 47 GRAPH OF AVERAGE VALUE OF EACH CLASS BASED ON D10 AND D60 WITH THEIR STANDARD DEVIATION IN THE ASMARI FORMATION DEBRIS	80
FIGURE 48 GRAPH OF D50-CU OF ALL SAMPLES IN THE ASMARI FORMATION DEBRIS	81
FIGURE 49 GRAPH OF AVERAGE VALUE OF EACH CLASS BASED ON D50 AND CU WITH THEIR STANDARD DEVIATION IN THE ASMARI FORMATION DEBRIS	81
FIGURE 50 TEXTURE OF THE SEYMAREH LANDSLIDE DEBRIS	82
FIGURE 51 GRAPH OF EFFECTIVE STRESS VS. DENSITY AS DERIVED BY LABORATORY TESTS ON THE FINE-GRAINED PORTION OF THE SAMPLES	84
FIGURE 52 GRAPH OF PERMEABILITY VS. DENSITY AS DERIVED FROM THE PERFORMED LABORATORY TESTS	84
FIGURE 53 GRAPH OF STRESS-DENSITY-DEPTH	85
FIGURE 54 GRAPH OF STRESS VS. PERMEABILITY	85
FIGURE 55 GRAPH OF DENSITY VS. DEPTH	86
FIGURE 56 USCS CLASSIFICATION OF ALL SAMPLES	88
FIGURE 57 GRAIN SIZE DISTRIBUTION OF SAMPLES IN THE ASMARI FORMATION DEBRIS	89
FIGURE 58 GRAIN SIZE DISTRIBUTION OF SAMPLES IN THE PABDEH-GURPI FORMATION DEBRIS	90
FIGURE 59 DISTRIBUTION OF GRAIN SIZE CLASSES OF THE DEBRIS MATRIX IN THE ASMARI FORMATION AREA	91
FIGURE 60 AREAS WITH DIFFERENT PERMEABILITY BASED ON THE LABORATORY TESTS PERFORMED ON THE SAMPLES OF DEBRIS MATRIX	93
FIGURE 61 PERMEABILITY SECTION ON THE DEBRIS	94
FIGURE 62 OUT CROPS OF GACHSARAN FORMATION ALONG THE SEYMAREH RIVER	95
FIGURE 63 THE LOCATION OF OUTCROPS OF GACHSARAN FORMATION AND SECTIONS	96
FIGURE 64 SECTION 1-1' AND 2-2'	97
FIGURE 65 SECTION 3-3' AND 4-4'	98
FIGURE 66 SECTION 5-5' AND 6-6'	99
FIGURE 67 SECTION 7-7'	100
FIGURE 68 SECTION 8-8' AND 9-9'	101
FIGURE 69 SECTION 10-10' AND 11-11'	102
FIGURE 70 SECTION 12-12' AND 13-13'	103
FIGURE 71 KINEMATIC INDICATORS ON THE SEYMAREH LANDSLIDE DEBRIS	106
FIGURE 72 STRESS ZONES FORMED ON THE LANDSLIDE DEBRIS DURING MASS EMPLACEMENT	108
FIGURE 73 EVIDENCES THAT HELPS TO RECOGNIZE THE FAILURE MECHANISM OF THE LANDSLIDE DEBRIS (GULLIES AZIMUTHAL DIRECTION IN THE SECONDARY REGIONS, SPRINGS AND PERMEABILITIES)	111
FIGURE 74 USCS CLASSIFICATION OF THE FINE-GRAINED SAMPLES	129
FIGURE 75 USCS CLASSIFICATION OF THE FINE PART OF THE COARSE-GRAINED SAMPLES	130

List of Tables

TABLE 1 TOTAL MONTHLY AVERAGE PRECIPITATION OF POL-E-DOKHTAR	27
TABLE 2 TOTAL MONTHLY AVERAGE TEMPERATURE OF POL-E-DOKHTAR	27
TABLE 3 DETAILS OF THE LAKES ON THE THE SEYMAREH LANDSLIDE DEBRIS	45
TABLE 4 DETAILS OF THE SPRINGS AROUND THE SEYMAREH LANDSLIDE DEBRIS	45
TABLE 5 DIFFERENT ZONES ON THE LANDSLIDE DEBRIS BASED ON TONE, TEXTURE AND STRUCTURE OF AERIAL PHOTOS	54
TABLE 6 DENSITY RANGES ADOPTED FOR RIDGES, GULLIES AND BLOCKS	58
TABLE 7 THE RANGE OF TOALED DENSITY VALUE FOR EACH 1KM²	58
TABLE 8 THE RIDGES, GULLIES AND BLOCKS TOALED DENSITIES CLASSES	58
TABLE 9 LANDFORMS ASSOCIATIONS FOR DEFINING PRIMARY AND SECONDARY CONDITIONS	61
TABLE 10 PROBABILITY OF LANDFORM ASSOCIATIONS WHICH PROVIDE A RANK TO THE ATTRIBUTION OF PRIMARY OR SECONDARY CONDITIONS	61
TABLE 11 MATRIX OF PROBABILITIES	62
TABLE 12 RIDGES CLASSIFICATION BASED ON THEIR CURVATURE RANGE	66
TABLE 13 KINEMATIC INDICATORS CLASSIFICATION BASED ON THEIR AZIMUTHAL DIRECTION RANGES	66
TABLE 14 GULLIES CLASSIFICATION BASED ON THEIR AZIMUTHAL DIRECTION RANGES	67
TABLE 15 RANGE OF D10 AND D60 FOR EACH CLASS	80
TABLE 16 MORPHOMETRIC PARAMETERS OF THE SEYMAREH LANDSLIDE	112
TABLE 17 EVALUATION OF THE SEYMAREH AND KASHKAN LANDSLIDE DAMS BY SOME INDICES	112
TABLE 18 LOCATION OF THE PHOTOS	127
TABLE 19 DETAILS OF THE SAMPLES	127

List of Equation

LINE DENSITY = $(L1 * V1) + (L2 * V2)$ (AREA OF CIRCLE)

POINT DENSITY = (NUMBER OF POINTS) AREA OF CIRCLE

EQUATION 1 LINE DENSITY51

EQUATION 2 POINT DENSITY52

Abstract

Understanding the landslide debris emplacement kinematics and the landslide failure mechanisms is essential for the definition of hazard and for the reconstruction of risk scenarios functional to mitigation strategies. Landslides in the southwest of Iran are particularly numerous, especially in the Zagros sedimentary basins. According to some estimates based on studies and research conducted to date, between 10,000 and 11,000 years ago, a large landslide (estimated maximum volume of 44 Gm³) took place in the city of Pol-e-Dokhtar near the Lorestan region (west sector of Iran). Because this landslide has blocked the course of the Seymareh River, it is known as the Seymareh landslide. This giga-landslide is considered the largest on the Earth's surface.

In the present PhD thesis, in order to find key interpretative elements and parameters for describing the longevity, the emplacement kinematics and the rupture style of the Seymareh landslide debris, morphological elements were found with high detail visible in the enormous landslide debris. After mapping the morphological elements, a zonation of the landforms in the landslide debris was performed by computing the spatial density of the main surface features including ridges, gullies and blocks. In the next step, using the zonation of the main surface features, a statistical approach was applied to zone the landslide debris in primary (original) and secondary (modified) regions which are respectively referred to the original shape of the landslide debris and to the one modified by erosions. This statistical approach in combination with kinematics indicators deduced from ridges direction and blocks distribution in primary regions provides a useful interpretation for the landslide kinematics as well as for the landslide debris emplacement.

During a specific campaign, soil samples, representative of the landslide debris matrix, were also taken at different points of the debris, to be able to characterize them in the laboratory and classify them according to the USCS standard and to derive the permeability of finer portions in view of future hydraulic models aiming at quantifying the natural dam durability.

The obtained results were useful for understanding the mechanism and kinematics of the Seymareh landslide debris and its evolution. They also helped us to better constrain the failure mechanism of the Seymareh landslide and will be useful for obtaining risk scenarios, quantifying the related hazard and plan mitigation strategies.

Moreover, the landslide debris emplacement mechanism and kinematics deduced from kinematic indicators in the primary regions of the landslide debris as well as some outcrops of geological bedrock observed during field surveys led to the recognition of the basal surface of the landslide debris, making it possible to hypothesize the buried morphology of the paleo-valley of the Seymareh River.

Introduction

Understanding the physical property and emplacement of landslide debris by recognition and zonation of surface features and the matrix of landslide debris in giant landslide mass can provide insights for the zonation in sectors characterized by different behavior helping to better constrain failure mechanisms; moreover, it is useful to define hazard and consequent risk scenarios for mitigation strategies.

This current PhD thesis aims to find key interpretative elements and parameters for describing the longevity, the emplacement kinematics and the rupture style of the giant Seymareh landslide dam (western Zagros Mts., Iran), as a function of dam morphometry, sedimentology and geotechnical properties.

Since natural landslide damming can occur at different scales and in different contexts worldwide, definition of the hazard and consequent risk scenario due to the formation and failure of the Seymareh natural dam could be an extreme reference for future events.

This study infers to the management of risks associated to the effects of landslide damming. The first risk condition can be associated to the upstream submersion and downstream flooding of lands previously inhabited and/or exploited for rural activities. The second risk condition is associated to increasing erosion rate by the river after dam cutting, which can cause increased sediment to supply downstream. Furthermore, as an effect of landslide damming, slope instabilities can be activated in the areas surrounding the lake (due to both submersion by the lake and increased river erosion). All these features can be generally recognized in worldwide cases, but since the Seymareh is one of the largest known landslide dams in the world, this study could provide extreme reference hazard conditions and related risks associated to landslide damming.

The main steps performed in this doctoral thesis can be summarized as follows:

Chapter 1: it provides a literature review regarding the landslide damming and performed investigation for understanding their complex behavior. This chapter also provides a literature review specifically on the Seymareh landslide.

Chapter 2: it focuses on the study area, according to geological setting, seismicity, climate and geomorphological features. It introduces the most important parameters that plays a significant role in shaping different landforms. Then, describes the morpho evolutionary processes in the study area.

Chapter 3: in this chapter of the thesis, the Seymareh landslide debris boundary, as well as the ridges, gullies, denudation scarps, extensional features, springs and blocks on the landslide debris are recognized and mapped in GIS through the interpretation of satellite optical images (Google Earth and aerial photos) followed by a field survey. Then a new statistical approach based on analyzing the spatial density of main features is proposed that recognizes the primary and secondary zones on the landslide debris area. Following the results of this chapter are demonstrated.

Chapter 4: in this chapter of the thesis, the grain size distribution of Seymareh landslide debris is determined by applying 2 sampling techniques and 3 analyzing methods and the permeability of debris is measured. Following the results of this chapter are demonstrated.

Chapter 5: it defines the geological model of the landslide debris.

Chapter 6: this chapter discusses the emplacement kinematics, the longevity and the rupture style of the Seymareh landslide debris.

Chapter 7: this chapter summaries the general work and provides the conclusions.

Chapter 1- State of the art

1.1 Landslide damming

Landslide damming is a relatively common occurrence in hilly and mountainous areas caused by landslide which reaches a valley floor and closes the riverbed (Costa and Schuster 1988; Ermini and Casagli 2003; Korup 2004; Evans et al. 2011; Coico et al. 2013; Tacconi Stefanelli et al. 2016; Fan et al. 2017). If a lake forms upstream of a landslide dam, it may pose serious threats to people and their property due to upstream inundation and downstream flood generated by breaching of such dams, initiation of other landslides and debris flows (Chen et al. 2011; Evans et al. 2011; Peng and Zhang 2012; Fan et al. 2017). Most of the rockslide dams are emplaced during strong earthquakes and torrential rainfalls (Costa and Schuster 1988; Ermini and Casagli 2003; Korup 2004; Evans et al. 2011; Peng and Zhang 2012). The consequence of landslide damming in the regions with high population can be dramatic. By increasing the knowledge on landslide damming, in some cases, it is possible to mitigate these situations by planning some mitigation strategies. When this is not possible, for little knowledge on landslide damming and for technical limitations (related to available time and to size of the phenomenon), landslide dams may represent big hazards (Tacconi Stefanelli et al. 2015). Therefore, evaluation of the stability and potential hazard and risk of landslide dams is very important for the mitigation measures (Ermini and Casagli 2003; Dal Sasso et al. 2014).

Costa and Schuster (1988) by focusing on the relation between the landslide deposit and the underlying geomorphology classified landslide dams in six types (Figure 1). Despite the existence of different classification systems (Varnes 1978; Cruden 1996; Hungr et al. 2014) their classification system has been preferred since its development in 1988. Hermanns et al. (2011) by studying 20 landslide dams formed by landslides with volumes more than 10^6 m³ in Argentina found that some of them did not fit with the Costa and Schuster landslide dam classification and defined a further landslide dam type (Figure 1). The classes added are not new morphological forms of rock avalanche deposit, but instead represent varied river response to the Type II blockages of Costa and Schuster (1988).

Different morphological parameters control the emplacement mechanism, kinematics and behavior of landslide dams (Ermini and Casagli 2003, Tacconi Stefanelli et al. 2016, Rouhi et al. 2019). The parameters describing the geomorphology of the valley such as valley width, slope angle and the height of the release area exert control on the emplacement mechanism and

kinematics of the landslide deposit (Ermini and Casagli 2003, Tacconi Stefanelli et al. 2016, Rouhi et al. 2019), and indirectly control the likelihood of landslide dam formation (Nicoletti and Sorriso-Valvo 1991).

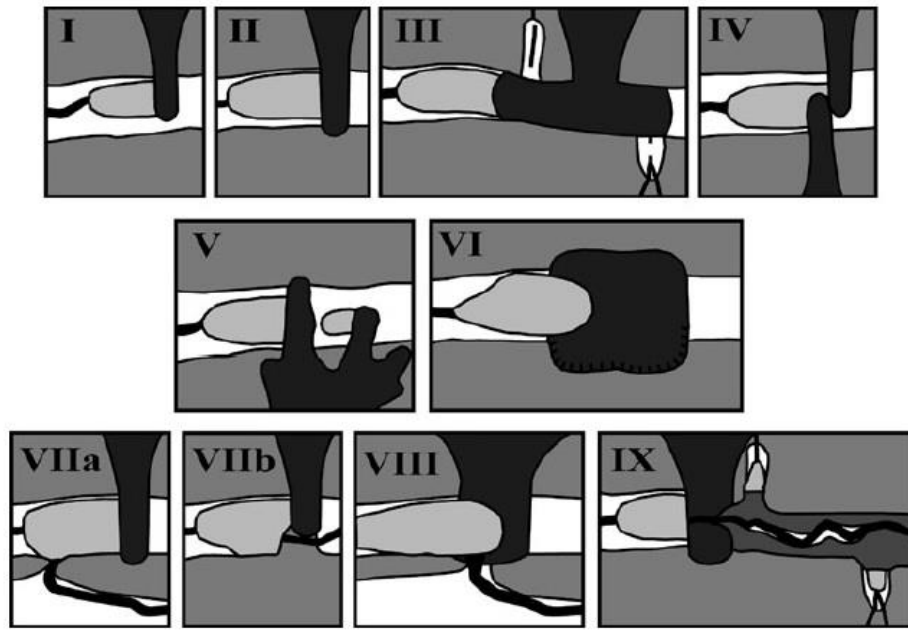


Figure 1 Landslide dam types I–VI by Costa and Schuster 1988 and new proposed dam types by Hermanns et al. 2011

Landslide dams can be characterized by morphological parameters such as: the size and shape of the depositional feature (Tacconi Stefanelli et al. 2015). In the case of cut landslide dams, the size, shape and distribution of features on their surface helps to forecast the cutting process.

Some authors by extracting the geomorphic parameters of landslide dams conducted inventories for some countries in the world. These include New Zealand inventories which consist of 232 dams (Korup 2004) the Swiss inventories with 31 cases (Bonnard et al. 2011), Chinese inventories with 1239 cases (Peng and Zhang 2012), 828 cases during Wenchuan earthquake (Fan et al. 2012a, b), 51 cases in the Cordillera Blanca Mountains, Peru (Tacconi Stefanelli et al. 2018) and in Italy, some authors compiled landslide dams inventories covering different portions of the Italian territory (Pirocchi, 1992; Casagli and Ermini, 1999; Coico et al. 2013) at different scales and with different standards of detail. Tacconi Stefanelli et al. (2015) homogenized these inventories and new data to set a national-scale archive of 300 landslide dams occurred in Italy.

Some inventories of landslide dams with the intention to investigate the longevity (Ermini and Casagli, 2003; Tacconi Stefanelli et al. 2015) and failure mechanism (Schuster and Costa 1988; Evans et al. 2011) of dams that fails were obtained so far. These inventories show that landslide dams fail by three processes including: overtopping, piping and sliding collapse. They also express that landslide dams may last for some minutes or several thousand days and 50% of failed rockslide dams, failed within 10 days of their formation.

The interpretation of landslide dam failure is a complex topic, because of the numerous variables involving the hydrodynamic interference between landslides, rivers and dam creation at the same time.

Numerous attempts have been made to investigate the complex behavior of the landslide dams. Some authors using landslide dams' inventories, proposed some geomorphic indexes (Swanson et al. 1986; Ermini and Casagli 2003; Coico et al. 2013; Dal sasso 2014) to predict the formation and evolution of landslide dams. These indexes result from the composition of two or more morphological attributes that characterize the landslide (e.g. landslide volume or length) and the involved river valley (e.g. valley width). They proved that these indexes could be a useful tool for making accurate predictions concerning the stability of landslide dams. Nash (2003) took into consideration the block size and proposed Modified Dimensionless Blockage Index (MDBI) and show that the average block size (D_{50}) of the dam material exerts significant influence on dam longevity and evolution.

Recently, Tacconi Stefanelli et al. (2016) to overcome some limitations of other indexes, introduced two new ones: The Morphological Obstruction Index (MOI) and the Hydro morphological Dam Stability Index (HDSI) and analyzed about 300 landslide dam events extended all over Italy. The newly proposed indexes (Tacconi Stefanelli et al. 2016) show an improvement in the forecasting effectiveness and have the advantage of being based on morphometric input parameters that can be easily and quickly assessed on a distributed way even over large area.

These indexes consider mainly geomorphic variables characterizing both the landslide (e.g. landslide volume or length) and the river channel (e.g. valley width) to understand the key parameters controlling the stability and evolution of landslide dams, and to use them for providing a better modified geomorphic index. Generally, the stability and evolution of a landslide dam should be assessed based on numerical simulations or an experimental model (Chen et al, 2011). In most cases, numerous accurate parameters and materials are not easily accessible, therefore for

an immediate evaluation of landslide dams' stability, geomorphic valley parameters and morphometric dam parameters should be analyzed (Jakobsen, 2016). A comprehensive formula or approach for assessing the behavior of landslide dams should consider all parameters related to the landslide, landslide dam and river.

Since the erosional processes on landslide dams which lead to their failures by overtopping or piping depends on grain size distribution of the debris material (Swanson et al., 1986; Costa and Schuster, 1988; Pirocchi, 1992; Casagli and Ermini, 1999) and its effects on the seepage rate through the debris, a branch of research activity directed to the prediction of landslide dam behavior is focused on the study of grain size distribution of the debris material composing a landslide dam (Casagli et al. 2003). The acquisition of grain size data is extremely important for the correct interpretation of the evolution of landslide dams. Despite its importance, the investigations aimed at determining the grain size distribution of landslide dams have never been standardized. This is mainly a consequence of the problems related to the phase of sampling debris materials and deposit heterogeneity that often range in size from blocks of tens of cubic meters, to very fine particles (Dufresne and Dunning 2017).

Casagli et al. (2003) applied different techniques for sampling and processing the grain size distribution of landslide dams in the Northern Apennines and concluded that the landslide dam debris sampling and grain size data processing remain very difficult and uncertain processes which requires further tests. They suggest that a complete description of the grain size distribution of heterogeneous materials composing landslide dams can be carried out only by integrating the results gathered by applying volumetric techniques to the finer material and grid by number to the coarser part.

Dunning et al. (2005) studied rock avalanche deposit and proposed three facies approach (the Carapace, Body, and Basal facies) for analyzing the rock avalanche deposits. Based on three facies approach, surface and near-surface material are Carapace facies and these facies can account for as much as 30 % of a deposit by thickness, but for considerably less by mass due to the large void spaces present. The Carapace is an assemblage of large, angular interlocking blocks created during the collapse of the bedrock slope and transported along the near surface of the rock avalanche and is characterized by high hydraulic conductivities, in the region of 0.1 ms^{-1} for a relatively fine carapace of argillite (Falling Mountain, New Zealand). The Body facies is beneath the carapace and forms the bulk of most rock avalanche deposits. The material of body facies is

angular, poorly sorted, and highly fragmented. The Body facies retains the original source stratigraphy in the final deposit, often as a series of sub-horizontal bands stretched during motion regardless of the original source rock orientations and an argillite sample in the interior of the Falling Mountain rock-avalanche deposit yielded hydraulic conductivity values of around $3 \times 10^{-3} \text{ ms}^{-1}$ and porosity of around 20 % (Dunning et al. 2005). Dunning (2006) carried out field and laboratory sieve method combined with laser granulometry to characterize the sedimentology of five rock avalanches deposits around the world and concluded that the grain size distributions of the deposits were controlled by their source lithological variation rather than transport mechanism. Therefore, different rock avalanches have different grain size distributions and compositions, but the broad grain-size distributions (from microns to meters) exist in all deposits. Dufresne et al. (2016) showed that rock avalanche and rockslide depositional facies are primarily process dependent, but that their degree of development can be strongly influenced by lithology, travel distance, and external influences such as shear-interruption by sediment injection. Later, in (2017) Dufresne and Dunning studied the deposits of two carbonate rock avalanches by sampling based on different defined facies for understanding the processes underlying rock avalanche emplacement and concluded that each facies produce a unique grain size distribution, and their histograms can serve as a tool for facies/process identification and for sensible comparison between deposits and lithologies.

Bianchi Fasani et al. (2011) evaluate possible erosion, overtopping and piping of the Scanno rockslide dam based on geological, geophysical and hydrogeological investigations and demonstrate the importance of geological models in understanding and predicting the longevity of rockslide dams. Later in 2014, Bianchi Fasani et al. hypothesized a cause-effect relationship between the geodynamic evolution of an orogenic belt and a rock avalanche. Della Seta et al. (2017) in the framework of morpho-structural evolution of an area has constrained the past rock avalanche events for depicting future hazard scenarios through numerical forward analysis. Longchamp et al. (2016) analyzed rock avalanche dynamics and deformation process by a detailed structural analysis of the deposits coming from data of 3-D measurements of mass movements which leads to the identification of three regimes (extensional, compressional and shearing) during the propagation of the mass.

Some authors tried to understand failure mechanism of landslide dam after their formation for mitigation measures based on experimental studies. For example, Zhang et al (2012) performed

13 flume experiments to calculate the erosion and sediment transport rate during the processes of dam break caused by overtopping and concluded that the maximum value of erosion coefficient always occurs near the downstream edge of the dam crest and the length of the dam crest, the inner slope and the dam composition affect the sediment transport during the dam breakage processes. Zhou et al (2013) through a set of model's experiments investigated the landslide dams' failures by upstream flows at Zhouqu and illustrated that both low and high flow discharges of upland flows can induce a cascading failure of landslide dams, after which the flow discharge can be significantly amplified. They also stated that the mechanisms behind the failures for the different flow rates are different. Okeke and Fawu (2016) studied the breach evolution mechanisms of landslide dams, as triggered by seepage and piping, they found that an increase in soil density and homogeneity of the dam materials reduced the potential to form a continuous piping hole through the dams. Furthermore, the potential for piping and progression of the piping hole through the dams increased with an increase in the percentage of fines and a decrease in hydraulic conductivity. The rate of pipe enlargement is related to the erodibility of the soil, which itself is inversely proportional to the soil density. Wang et al (2018) carried out four outdoor tests to investigate the premonitory factors of landslide dam failure, and stated that dam-crest settlement, seepage-water turbidity and self-potential changes can be regarded as premonitory factors of landslide dam failure. Experimental studies have mostly focused on dam failure triggered by overtopping and seepage.

1.2 Seymareh landslide

The prehistoric Seymareh landslide in the foreland margin of the Zagros Mountains, Iran is one of the largest known landslides on the Earth's continental surface. The landslide occurred along the provincial border between Ilam and Lorestan, 60 km west of the Iraq border (Figure 2). A huge avalanche crossed two valleys and travelled about 19 km far, damming up two major rivers. Two large lakes formed and remained filled for a long period of time until they eventually breached the natural dam and eroded a channel through it

The first studies on the Seymareh landslide were done by DeMorgan (1895) who mistakenly examined the landslide debris as a glacial deposit. Harrison and Falcon (1937) were the first researchers who studied this landslide as a slip and provided a general description of the dimensions and morphology of the slip. In 1938, the same authors studied more in detail the landslide debris, scar area and the movement of the debris and concluded that the Seymareh

landslide was a single event. This idea was confirmed by Roberts and Evans (2013) who studied the failure mode and debris morphology and strongly suggested that the Seymareh rock avalanche was an instantaneous single event. Oberlander (1965) included a short appendix on the landslide in his study of the Zagros streams and discussed its origin in relation to the activity of the Seymareh River. Watson & Wright (1969) characterized the geomorphology and stratigraphy of the debris, discussed the origin of the initial rockslide and examined the debris avalanche emplacement mechanisms. They also express that evidence of large blocks on the surface probably reflects that a thick layer of limestone rock was above other rocks when the slide began. This agrees with Roberts and Evans (2013) who based on the distribution of limestone rocks in the distal debris suggested that during initial failure the upper plate overrode the lower plates to travel the farthest. Shoaiei and Ghayoumian (2000) estimated that the volume of landslide is 24 to 32 billion cubic meters but according to new calculations performed by Roberts and Evans (2013), the volume of the landslide is estimated to be 44Gm³. Shayan (2006) based on geomorphologic field and documentary surveys and historical details concluded that the age of event was about 1100 years ago which is not in agreement with Roberts and Evans (2013) and Delchiaro et al. (2019a).

Roberts and Evans (2013) based on an accelerator mass spectrometry radiocarbon dates, indicates the rock avalanche occurrence between 8710 and 9800¹⁴C years BP and Delchiaro et al. (2019a) using OSL method, dated lacustrine terrace at a site with two different depths and reported that the age of the Seymareh lacustrine terrace is between 7.37 and 10.4 ka. Shayan (2006) also expressed that a thick layer of limestone rock departed from Kabir–Kuh anticline crest and moved by a NW direction toward Seymareh River valley but also this conclusion by Shayan (2006) is not in agreement with NE direction that has been reported by Roberts and Evans (2013) based on field measurements of bedding surface orientations. Yamani et al (2012) due to the thickness and extent of the lacustrine terrace, sedimentology of the lacustrine terrace, morphometric measurements of the lacustrine terrace and especially altitudes of lacustrine terrace argue that Seymareh landslide occurred in three or four stages which agrees with Azimi (2012) who investigated the morphological, geometric, and sedimentological characteristics of the Seymareh landslide, lake and its related terraces and concluded that Seymareh landslide occurred in 3 or 4 stages, too. Shoaiei (2014) based on the lacustrine thickness, river discharge and sedimentation rate, calculated the longevity of Seymareh landslide dam equal to 933 years. Beiranvand et al. (2016) calculated the morphometric parameters of landslide and based on these calculation, the width of rupture

(W_r), length of rupture (L_r), depth of rupture (D_r), length of displaced mass (L_d), width of displaced mass (W_d), depth of displaced mass (D_d) and volume of landslide are equal to 15.5 km, 7.81 km, 300 m, 16.06 km, 15.5 km, 300 m and 3.9 km³, respectively. Siamak Sharafi (2016) reconstructed the changes caused by the Seymareh landslide, and the formation of Seymareh and Jaidar lakes on ancient sites in various cultural periods. In ancient times, there might have been permanent living in the Seymareh River terraces where events such as landslides and the subsequent creation of a lake could have had a significant impact on the lives of the inhabitants of the area, because they had to leave or move from the place they were settled (Moghaddam et al. 2007). Delchiaro et al. (2019a) performed detailed geological and geomorphological surveys and mapped the Seymareh valley and dated with optically stimulated luminescence (OSL) two suites of fluvial terraces (one older and one younger than the Seymareh landslide) as well as a lacustrine terrace (formed after the temporary landslide damming), to provide time constraints to the main evolutionary stages of the valley before and after the emplacement of the landslide. Later, Delchiaro et al. (2019b) analyzed the multi-temporal hazard related to the sequence of events and processes linked to the landslide occurrence in terms of potential, effective, residual and inherited hazard.

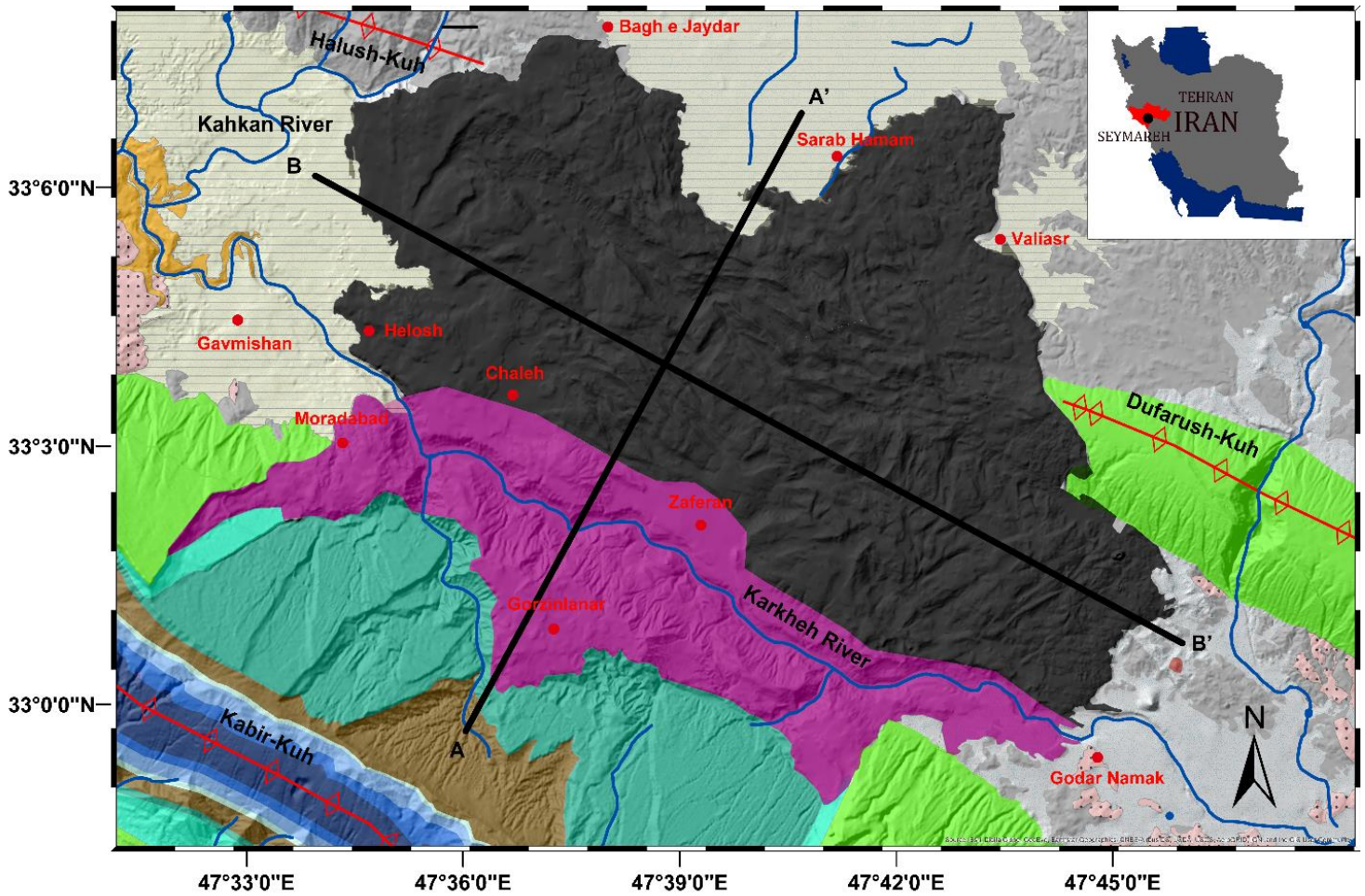
Although a lot of researches on landslide damming events in various parts of the world have been done, their evolution and behavior are not understood well. These studies didn't focus on the surface features of the landslide debris to recognize the original and reshaped regions in order to select the landforms more adapt for investigating the emplacement kinematics.

Chapter 2- Geological setting

2.1 Stratigraphic and Geo-structural features

The Seymareh landslide (SL) involved the north-eastern flank of the Kabir-Kuh fold, in the distinctive belt of Zagros (or Simply) folded belt (Talbot and Alavi 1996, Stampfli and Borel 2002, Golonka 2004, McQuarrie 2004, Agard et al. 2005, Mouthereau et al. 2012).

Structural setting of the outcropping formations represented an important predisposing factor for the giant landslide (Roberts and Evans 2013, Delchiaro et al. 2019a). In this regard, we referred to the geological map and the stratigraphic column of Figure 2 and Figure 3 and to the stratigraphy proposed by James and Wynd 1965, Alavi 2004 and by the detailed mapping of Kabir-Kuh conducted by Iran Oil Operating Companies (Setudehnia and Perry 1967, Takin et al. 1970, Macleod 1970). At the base of the stratigraphic column there is the Bangestan Group, composed by the Sarvak Formation (Cretaceous, thickness; 750 m) and the Ilam-Surgah Formation (Late Cretaceous, thickness about 250 m). The Sarvak Formation consists of a thick carbonate unit that represents one of the largest reservoirs for hydrocarbons in Iran (Elyasi et al. 2014). At the top of the Sarvak Formation there is the Ilam-Surgah Formation, consisting of limestone of transgressive-regressive foredeep facies deposited in the pro-foreland basin (Elyasi et al. 2014). The Ilam-Surgah Formation is limited at the top by Gurpi Formation (Late Cretaceous, thickness about 400 m) consisting of a marly limestone, marl and hemipelagic shales of deep marine facies associated to the progressive migration towards S of the pro-foreland areas, which are in unconformity with the Sarvak and in onlap with the Ilam-Surgah (Elyasi and Goshtasbi 2015). Within the Gurpi Formation it is possible to recognize a considerably more calcareous horizon called Emam Hassan Member (25 m thick). Above the Gurpi Formation there is the Pabdeh Formation (late Paleocene - early Oligocene, thickness about 350 m) consisting of hemipelagic-pelagic calcareous shales (Elyasi and Goshtasbi 2015). In the Kabir-Kuh anticline area, as described by the detailed mapping of Iran Oil Operating Companies and confirmed by direct field survey (Figure 2 and Figure 3), the Pabdeh Formation is composed of three members: i) the lower Pabdeh member (150 m thick), which is dominated by marls and shales, ii) the Taleh Zang member (50 m thick), consisting of platform limestone, and iii) the upper Pabdeh member (150 m thick), composed mainly of calcareous marl.



Legend

- | | | | |
|----------------------------------------|--------------------------------------------|------------------------------------------------------|--------------|
| Agha Jari Fm. (Miocene-Pliocene) | Pabdeh Gurpi Fm. (U. Cretaceous-Paleocene) | Alluvial Deposits | Main Streams |
| Gachsaran Fm. (Miocene) | Emam Hasan Mb. (U. Cretaceous) | Lacustrine Deposits | Fold Axis |
| Asmari Fm. (Oligocene-Miocene) | Gurpi Fm. (U. Cretaceous) | Area of landslide debris with Asmari Formation | |
| Upper Pabdeh Mb. (Paleocene-Oligocene) | Ilam-Surgah Fm. (M. Cretaceous) | Area of landslide debris with Pabdeh-Gurpi Formation | |
| Tale Zang Mb. (Paleocene) | Sarvak FM. (M. Cretaceous) | Conglomerates | |
| | Village | | |

Figure 2 Geological map of the Seymareh landslide area

The succession is completed by the Asmari Formation (Oligocene – Miocene, thickness about 200 m), which creates a carapace originally covering the top of the Kabir-Kuh fold. The Asmari Formation consists of alternating fossiliferous, massive, and thinly stratified gray-brown limestone, microcrystalline limestone, dolomitic limestone, and marly limestone (Khoshboresh

2013). In the synclinal valleys between the Kabir-Kuh fold and the adjacent ones, the Asmari Formation is overlapped by a Miocene-Pliocene succession (Homke et al. 2004). Referring to the Changuleh syncline studied by Homke et al. 2004, the latter foreland stratigraphy include: i) the Gachsaran Formation (early Miocene - 12.3 Ma, thickness about 400 m), composed of salt, anhydrite, marl and gypsum; ii) the Agha Jari Formation (12.3 Ma – 3 Ma, thickness about 1400 m); and iii) the Bakhtiari Formation (3 Ma – early Pleistocene, thickness about 900 m). The Agha Jari Formation consists of sandstones and conglomerates, linked to the epicontinental evolution of the environment (Elyasi et al. 2014), while the Bakhtiari Formation consists of conglomerates characterized by coarse and mud-supported grains, sandstones, shales and silts (Shafiei and Dusseault 2008).

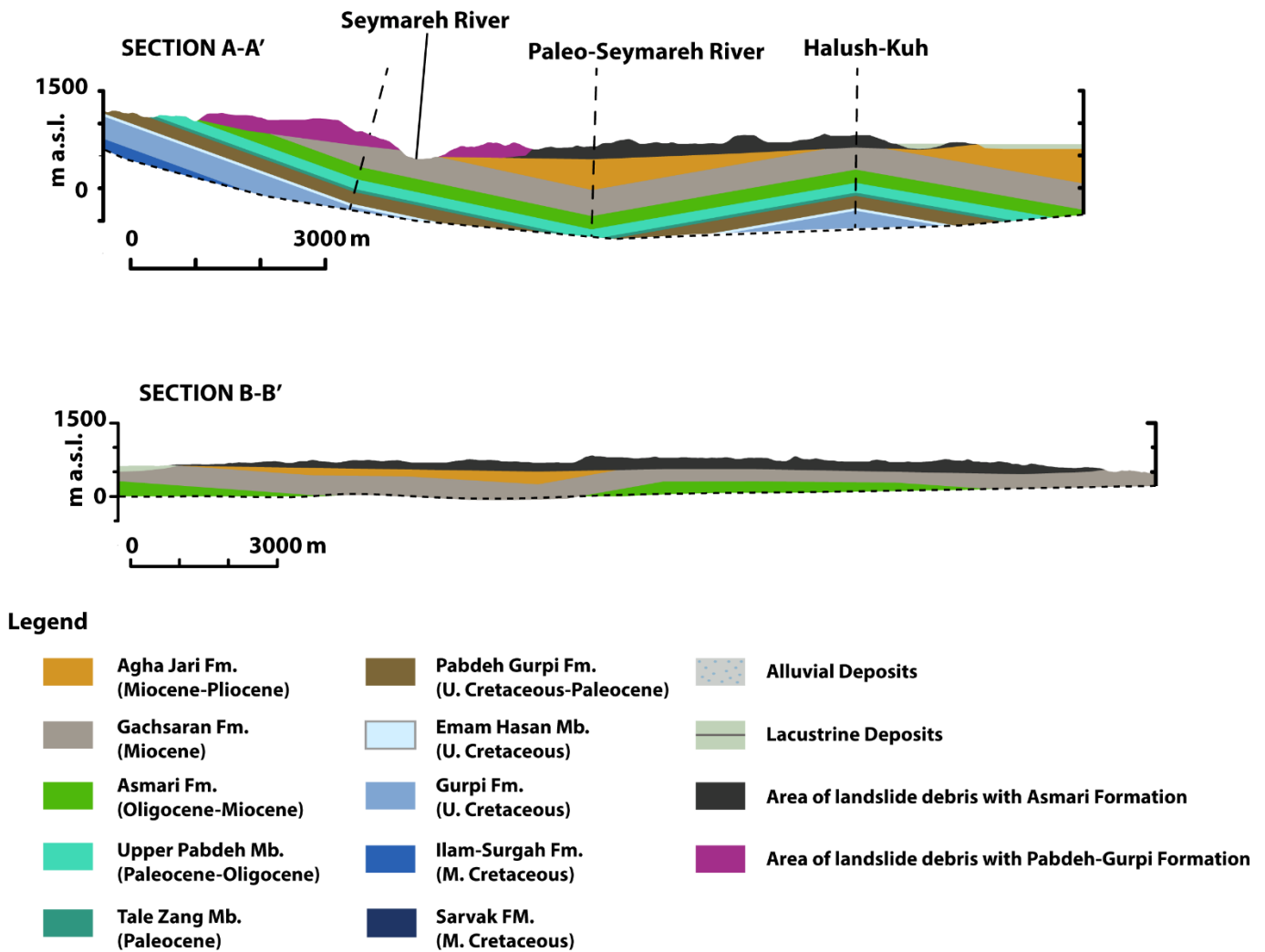


Figure 3 Cross sections across the Seymareh landslide debris according to the revised stratigraphic column for the Seymareh River valley

The Zagros mountain belt extends over 1800 km from Kurdistan in N Iraq to the Strait of Hormuz in Iran and results from the long-standing and ongoing convergence between the Eurasian and Arabian plates, during which time the Neo-Tethys oceanic basin was closed (Lacombe et al. 2011). The overall convergence of the two Eurasian and Arabian plates is estimated to be about 30 mm/year at 50°E and 40 mm/year at 60°E (De Mets et al. 1994, Jackson 1992). The Zagros is famous for its seismic activity and active deformation. The map in Figure 4 shows the earthquake epicenters and major faults of Lorestan and Ilam between 1900-2015. Based on the Iranian code of practice for seismic resistant design of buildings, named “Standard No. 2800”¹, Pol-e-Dokhtar is rated as region with average seismic risk.

¹ Buildings, Standard No. 2800” was published by the Building and Housing Research Centre (BHRC) in early 1988 and since then has contained the official requirements for seismic design in Iran. The second edition was published in 1999 while the third edition is currently published in 2007.

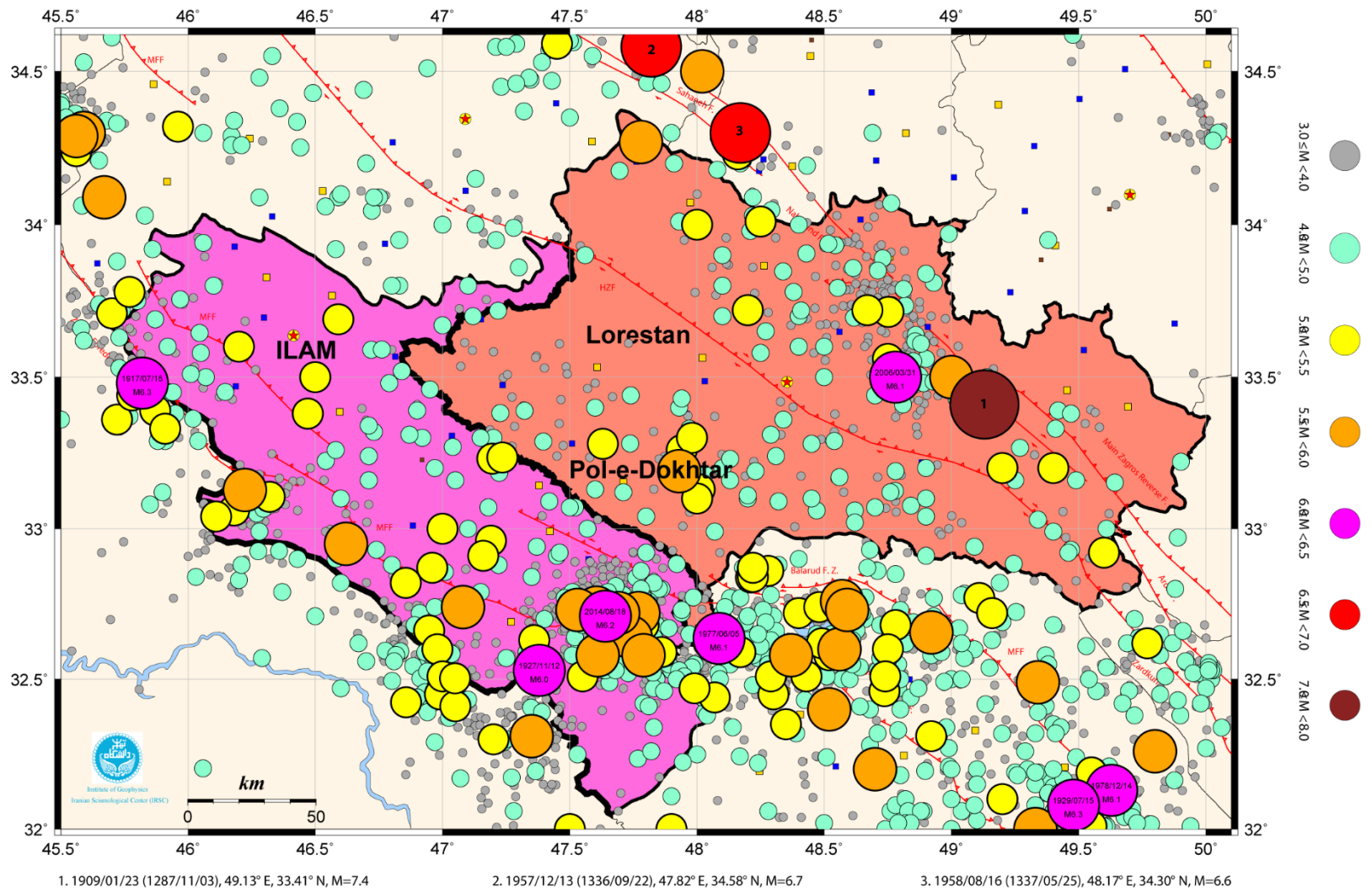


Figure 4 Earthquake Epicenter & Major Faults Map of Lorestan & Ilam, map n.12-B (collected by Dezvare, M., Naserieh, S., Rouhi, A & Boromand, B. 2015) Institute of Geophysics, Iranian Seismological Center (IRSC)

2.2 Geomorphological features

Ilam and Lorestan provinces are full of spectacular landforms shaped in response to active tectonics, therefore recognizing their characteristics in the study area is of great importance. The Lorestan province is part of the most external Zagros (western sector) characterized by "harmonic" fold systems passing eastward (i.e. in the internal zone of the Chain) to thrust-folds and imbricate systems. The study area consists of relatively high mountains with the general trend of northwest - southeast (Zagros process) (Figure 5).

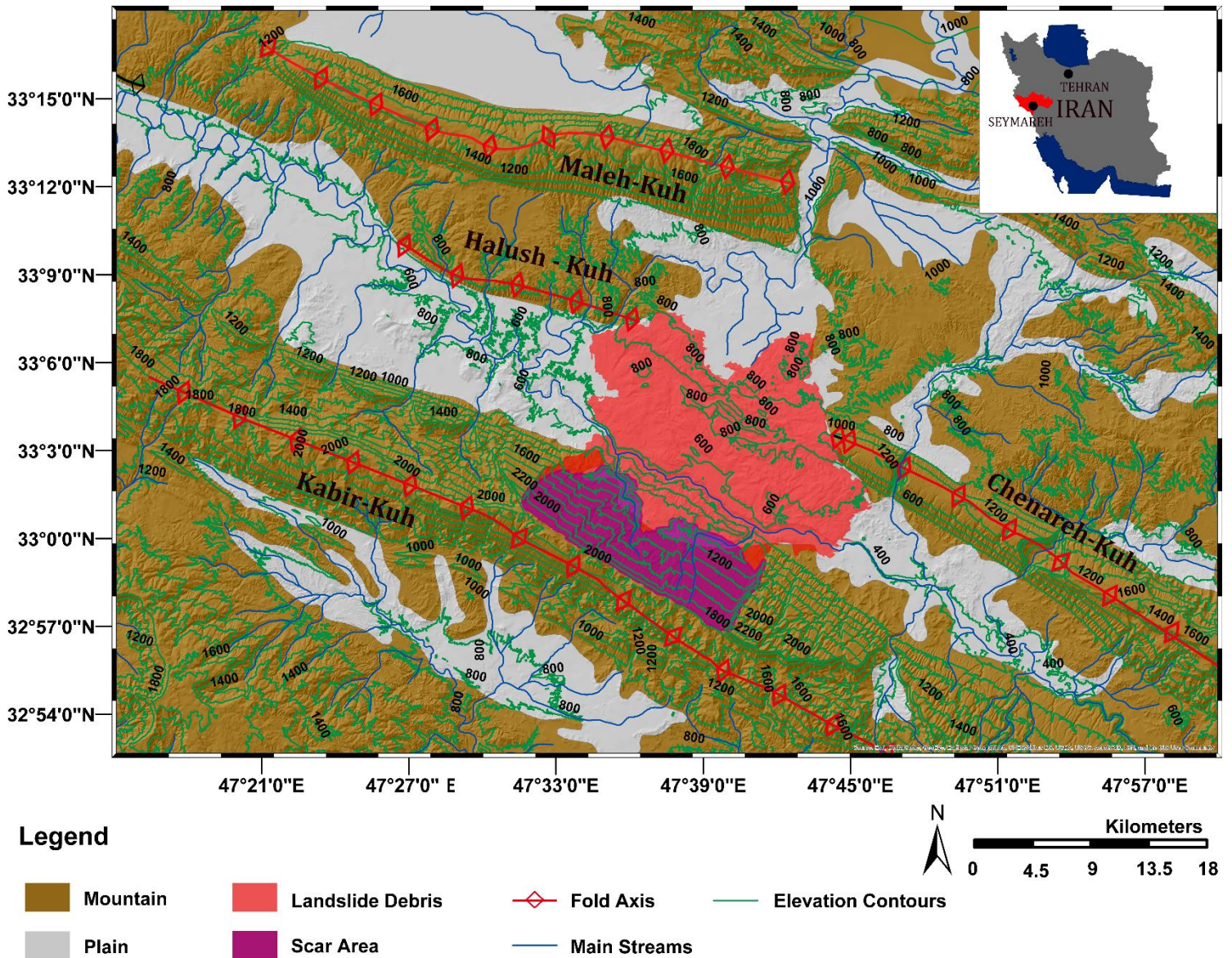


Figure 5 Main morpho-structures in the study area

The Kabir-Kuh and the Maleh-Kuh anticlines represent two main mountain range in the south and north of the study area, respectively (Figure 5). Maximum altitudes in the study area are in the Kabir-Kuh fold-ridge which reaches an altitude of about 2700 meters and minimum altitudes are in enclosed plains between the anticlines (the floor of the synclines) and in accordance with the Seymareh River with a height of less than 500 meters. The general trend of the Seymareh River is parallel to the general trend of the main structures of the region (northwest - south east) but in some parts due to the tectonic and geological reasons, its path is perpendicular to the structures of the region.

Meteorological information are important because firstly they specify the weather condition and the climate of each region and secondly, they play a decisive role in hydrologic (surface water) and hydrogeology studies. The use of meteorological stations data and statistics are essential to know the temporal and spatial variations of meteorological factors. Therefore, for understanding the climatic conditions of the study area, the average precipitation and temperature in the synoptic station of Pol-e-Dokhtar belongs to 16 years (from 2003 to 2018) were collected from the Ministry of Energy and Meteorology Organization of Iran and are reported in Table 1 and Table 2.

Table 1 Total Monthly Average Precipitation of Pol-e-Dokhtar

Total Monthly Average Precipitation of Pol-e-Dokhtar (mm)												
Month	Jan	Feb	Mar	Apr	May	Jun	Jul	Aug	Sep	Oct	Nov	Dec
Average Precipitation	56.55	45.9	50.1	62.98	22.96	0.36	0.01	0.85	1.3	26.03	63.50	63.10

Table 2 Total Monthly Average Temperature of Pol-e-Dokhtar

Total Monthly Average Temperature of Pol-e-Dokhtar (°C)												
Month	Jan	Feb	Mar	Apr	May	Jun	Jul	Aug	Sep	Oct	Nov	Dec
Average Temperature	9.43	11.81	16.50	21.33	28.11	34.73	37.43	36.78	32.17	25.4	16.04	11.13

The climate element of precipitation in the Pol-e-Dokhtar station shows that the average precipitation in the 16 years (from 2003 to 2018) was 32.80 mm. The study area in November with 63.5 mm had the highest precipitation and in July with 0.01 mm had the lowest precipitation.

Temperature is one of the most important parameters that, in addition to affecting other climatic elements, plays a significant role in shaping different landforms. As it is reported in Table 2, warm temperatures have coincided with the trend in the summer season and vice versa. The average temperature varies from about 9 degrees in the winter to 37 degrees in the summer. Due

to the influence of local factors and the regions low altitudes from the sea level, the temperature fluctuations in the hot seasons is lower. However, the effect of refrigeration systems in the cold season has led to a further decrease in the minimum temperature and the intensification of temperature fluctuations in the region. In the studied period, the lowest temperature was in the winter and the highest temperature was in the summer.

The Ombro-thermic curve (Figure 6) compares monthly changes in temperature relative to monthly rainfall changes throughout the 16 years period (2003-2018). The Ombro-thermic curve (Figure 6) demonstrate that from mid-April to mid-October, drought conditions dominate the area, and in other months the humidity conditions are above the drought. The simultaneous decrease of precipitation with increasing temperature in these months is a major cause of drought. Also, this curve represents two different seasons throughout the year. In spring and summer, with increasing the temperature and decreasing the precipitation, the region has warm and dry climate, in autumn and winter, with increasing rainfall and decreasing temperature, it has wet climate. Since the data of this curve has been extracted from 16 years period, the terms provided for each year can vary. In general, this diagram is suitable for understanding the general weather conditions of the area and do not have the details of other elements.

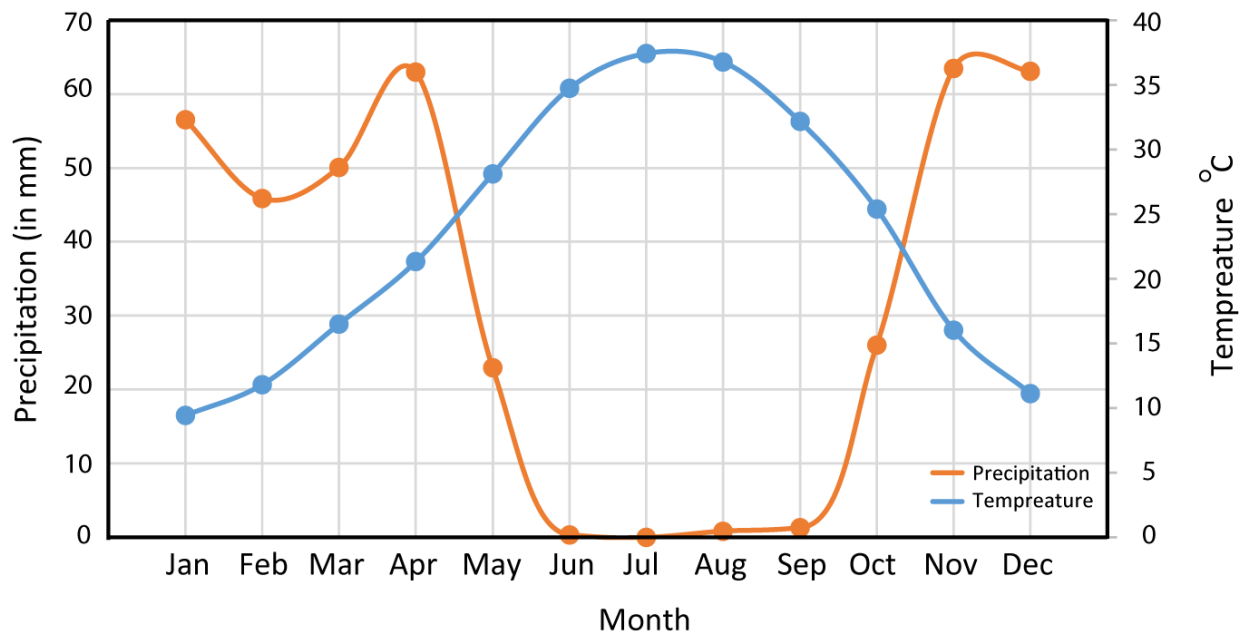


Figure 6 Ombro-thermic curve of Pol-e-Dokhtar

The Pol-e-Dokhtar and Darreh-Shahr watersheds terminate to the Seymareh landslide debris (Figure 7). Based on the report of Iranian Ministry of Energy, the total area of the Pol-e-Dokhtar and Darreh-Shahr watersheds are 2073.4 and 974.9km², respectively. The Kashkan and Seymareh Rivers are the main rivers inside the Pol-e-Dokhtar and Darreh-Shahr watersheds with 1.1 and 0.12% slopes.

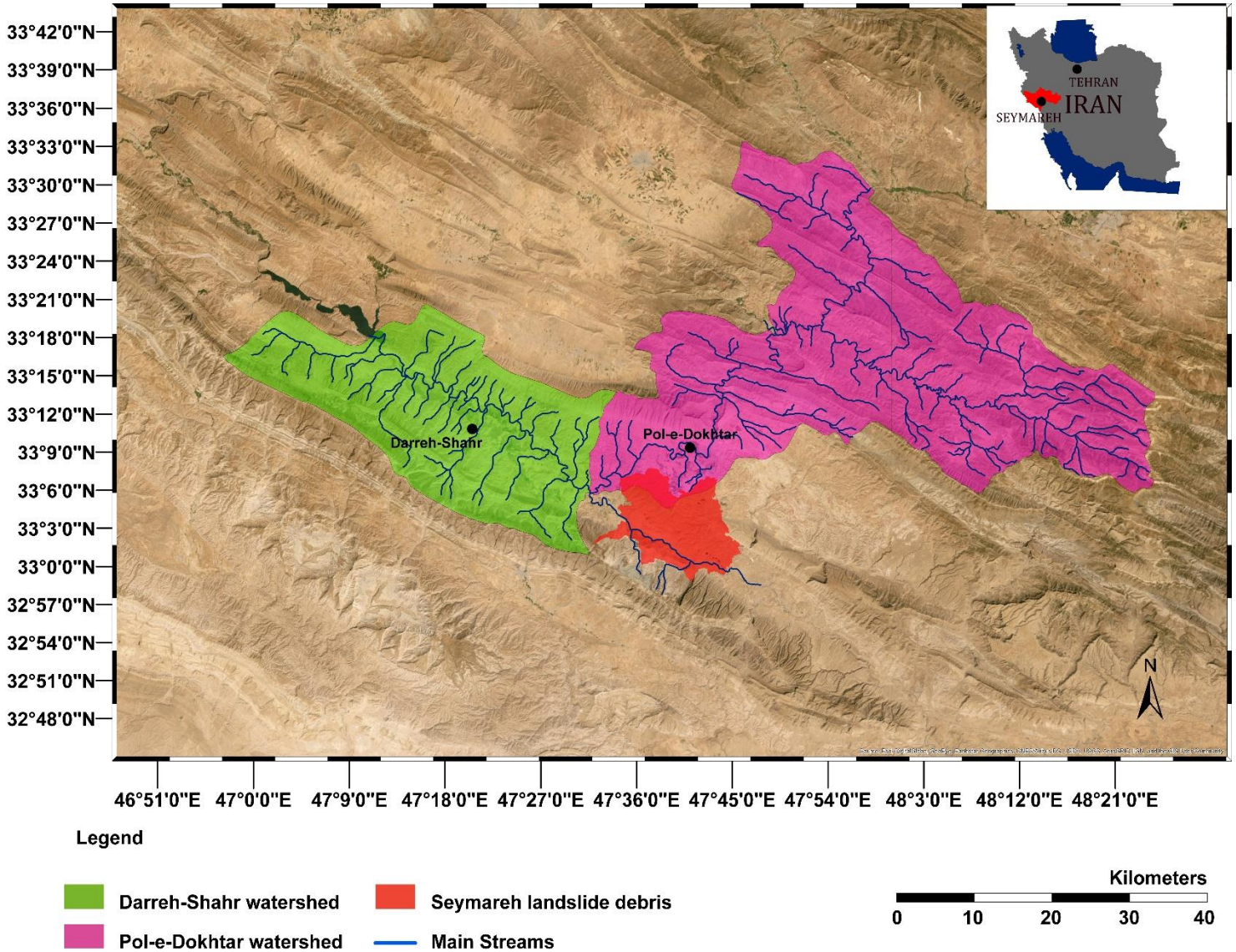


Figure 7 The Pol-e-Dokhtar and Darreh-Shahr watersheds

The outlet discharge of the Seymareh and Kashkan Rivers according to the Seymareh-Nazarabad and Pol-e-Dokhtar hydrometric station are 97.5 m³/s and 42.07 m³/s. By the reports of Iranian Ministry of Energy, the average discharge measured in the Seymareh-Nazarabad hydrometric station in the last 10 years leading up to 2012 has decreased by about 33% compared

to the long-term average of 45 years. The average discharge measured in the Pol-e-Dokhtar hydrometric station in the last 10 years leading up to 2012, also has decreased by about 28% compared to the average long-term average of 45 years. The statistics related to the discharge of the Seymareh and Kashkan Rivers shows that the joining of the Kashkan and Seymareh Rivers as the Karkheh River results in an unusual condition of high discharge and strong eroding force in the area.

The morpho evolutionary processes involving the study area are a function of mechanical and physical erosion of soil deposits and bedrock units outcropping in the mountain areas, erosion and degradation due to the simultaneous and combined operation of the dissolution and penetration of current water into the joints and fractures systems and rupture in the underlying layers. The study area has been affected by weathering, especially in past due to its high altitude, frosts and relatively high rainfall. Here the processes that are affected by the climatic factors are described below.

1. Mechanical weathering: in this type of weathering, the rocks are fragmented in pieces of different sizes without any significant changes in their nature. This type of weathering occurs by climatic elements such as temperature, freeze-thaw, wet-dry cycles. Frosts cause the rocks to change into the smaller particles due to the cracks and fissures in the rocks and faster soil formation occurs. At lower elevations, the effect of freezing on the destruction of rocks is less than the effect of temperature variations. The heat of the summer and the cold of the winter, but mostly the temperature fluctuations of the daytime, since the dilatation coefficient of the minerals forming the rocks are not equal, has caused the formation of fine particles in the mountains. These particles fall into the slopes of the mountains due to gravity. Temperature changes affect the shale surface. The effects of temperature from the surface to the depth of the stone decreases. As a result, between the surface and the depth, there is a tensile that creates cracks and fissures parallel to the surface

in the rocks and rocks shatters in laminate form. This type of erosion that separates rocks to different sheets, is called laminar erosion (Baharvand, 2008) (Figure 8).



Figure 8 Mechanical weathering

2. Chemical weathering: In this type of weathering, the nature of the rock changes and new materials forms. This type of weathering occurs in the presence of water and moisture and is usually by dissolution on carbonatic rocks. In the mountains of the region, due to cold and humidity in winter, this phenomenon prevails. The water mixes with carbon dioxide and solves the limestones which are made by calcium carbonate and changes them to the calcium bicarbonates which is soluble. This solution dissolves the rocks and creates holes and gaps when moving on the rock surface or inside it. All the karst forms are created by this phenomenon. The carbonate dissolved deposit in appropriate places and creates the cement (Figure 9).



Figure 9 Chemical Weathering

3. Biologic weathering: This weathering is caused by the activity of plants, animals and humans. Ants and worms increase the penetration of water and weathering of the soil. Animals by digging the soil and destroying the vegetation cause soil washing and accelerate the erosion process. Root of plants and trees degrade the rocks, but in most cases, they stick soil particles together and prevent flooding and soil degradation. Humans are the most destructive factor among living creatures that by destroying the vegetation causes soil degradation. In the marneous hills where the soil can be used for construction purposes, humans, by digging the hills, accelerate soil erosion by flooding and eliminate plant growth potential in soil (Figure 10).



Figure 10 Biologic Weathering

Due to the presence of erodible formations, conditions for the occurrence of various types of erosional processes are provided.

1. **Water erosion:** this type of erosion is most commonly found in the Agha Jari marly formation. In Jaydar plain, hills of marly formation can be seen. These striped hills are completely cut and destroyed in some areas by erosion caused by water erosion during heavy rainfall events. On the side of these hills, outcrops of Agha Jari Formation appear due to the destruction of vegetation and the resistant superficial layer which are ancient alluvial deposits. In all marly hills, this type of erosion is clearly visible (Figure 11).



Figure 11 Water Erosion

2. Badland erosion: in areas where the upstream erosion by drainage network removed the bottom of Tale Zang Formation characterized by a resistant lithology, the red or gray color of marls outcrop appears. Because of their high erodible nature, many parallel gullies are created which indicate severe erosion. This type of landscapes is called badlands. This type of erosion is most commonly seen in Pabdeh Formation (Figure 12).



Figure 12 Headward erosion

3. Gully erosion: is the removal of soil along drainage lines by surface water runoff. Once started, gullies will continue to move by headward erosion or by slumping of the side walls. Gully erosion occurs when water is channeled across unprotected land and washes away the soil along the drainage lines. Under natural conditions, run-off is moderated by vegetation which generally holds the soil together, protecting it from excessive run-off and direct rainfall. This type of erosion is abundant in the marly hills and on the landslide debris surface (Figure 13).



Figure 13 Gully Erosion

4. Floods: flood events dominate more than other processes related to surface running water. Autumn and winter rainstorms cause the soil to be washed at the surface of the mountains and plains. Agricultural lands and areas that lie on the slope water and river's path are under flood erosion. In the event of severe rainfall, flood erosion washes hundreds of hectares of land (Figure 14).



Figure 14 Flood Erosion

5. River incision and lateral erosion: this type of erosion takes place further along the margin of the rivers of the region, specially the Seymareh and Kashkan Rivers, the rivers that originate from the mountain range and seasonal rivers. Since the paths of these rivers flow on loose sediments, these rivers have eroded these margins in their paths and made several meanders. The Kashkan and Seymareh Rivers with their sinuous path have cut and destroyed many of fertile agricultural lands, especially in the downstream. These two rivers also have created many of fertile agricultural lands. Seasonal rivers cut and destroy lands due to winter flood.

One of the most important and spectacular geomorphological landforms in the Zagros mountains are gorges. These valleys, which appear on the sides and slopes of anticlines, gradually cut both sides of the anticlines until reaching to the basement. These valleys are influenced by various factors such as rocks type, cracks and fissures, folding shape and tectonics, slope gradient, layering and amount of water. These valleys in the karstic areas have a greater depth and width due to its pure carbonatic content and its dissolution. In the past, these valleys have played a significant strategic role due to the proper security conditions that they have created naturally and have played an important role in the formation of civilization in the region. An example of these gorges is the case of Bahram Chubin gorge, which was used during the Sassanid dynasty (Figure 15).



Figure 15 Bahram Chubin gorge

Gorges are abundant on the anticlines (Figure 16).



Figure 16 Gorges

V shape valleys are prospecting forms that are directly shaped by river erosion and slope processes. These valleys often formed along faults and have created various and spectacular landforms due to the resistance of rocks in the Seymareh landslide. The V shape erosion process affects pre-existing crack and fissures of rocks and it is strictly connected to the water discharge and slope gradient. If the rocks are hard, valley walls are vertical and dominant to the waterway and due to the hardness of the walls, water cannot erode the sides and erosion is vertical that creates V-shape valley. There are a lot of V-shaped valleys in the study area. Asmari limestone by the thin layer at the top and thick layer at the bottom causes more V-shape valleys form.

In loose and soluble areas, U-shaped valleys form more typically. These valleys are found in calcareous and karstic areas in the study area. Usually, both sides of the valley are in the shape of cliff which sometimes their heights are higher than 100 meters.

In the study area, cliffs due to landslide detachment are abundant. Some of these cliffs have been created due to the presence of transverse faults in the Maleh-Kuh on the north of Pol-e-Dokhtar. The walls of these cliffs have been stabilized due to the erosion of the valleys by the rivers and streams. In the Seymareh landslide (southwest Pol-e-Dokhtar), due to the detachment of a part of the Asmari Formation in the direction of the slope, there are lateral scarps on both sides of the Seymareh landslide scar area (Figure 17).



Figure 17 Cliffs due to the detachment of a part of the Asmari Formation

In the present climate conditions during the wet periods, precipitation is increased and as a result, the net power of the river is increased. Increasing the net power of the river, which is associated with increasing river discharge, causes the river bed to enlarge. Due to the high discharge volume and strong river floods in the Seymareh River, these flood plains are remarkably wide. According to the meandering pattern of the Seymareh River and its lateral erosion, these flood plains are formed on both sides of the rivers (Figure 18). These flood plains are composed of heterogeneous clay and gravel deposits which indicates the relevant transport power of the Seymareh River.

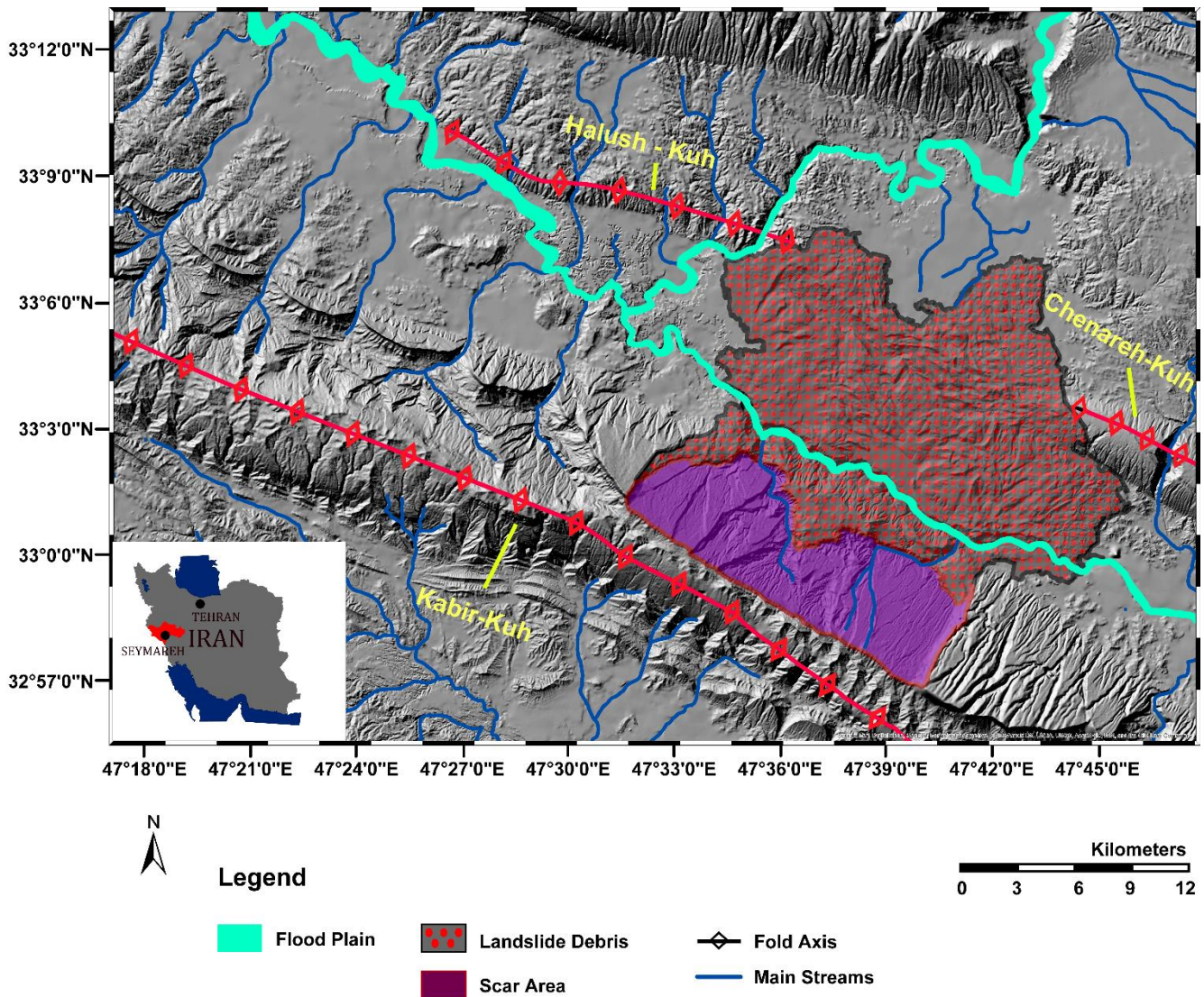


Figure 18 Flood Plain

The study area is characterized by a high frequency of landslides. The occurrence of these landslides upstream of the Seymareh landslide dam in some places has led to a redirection of Seymareh River.

The landslide dam was stable for a long period of time then it was cut (Delchiaro et al. 2019a). At present there is no lake at the back of the Seymareh landslide dam. Different geomorphological features are formed in the study area because of the formation and failure of the Seymareh landslide dam.

Alluvial deposits on the left and right bank of Kashkan, Seymareh and Karkhe River, as well as on the surface of Seymareh landslide debris with variable thicknesses can be observed (Figure 19). The old river terraces in the upstream of Seymareh landslide debris are buried under the lacustrine deposits and are visible, only in some places where the lacustrine deposits are eroded. Among the old and new lacustrine deposits, river terraces due to the sovereignty of the river environment during the formation of the lakes can be seen (Delchiaro et al. 2019a). There is a visible layering in the grain size of river terraces. In the periods when the net power of the Seymareh and Kashkan rivers increased, the sediments are thickened and less rounded. Conversely, in periods where the net power of the river has decreased, sediments tend to be smaller and more rounded. In the Jaydar lake, the remnants of river terraces in places where the valley has larger width can be observed (Figure 19).



Figure 19 Alluvial deposit on the Seymareh landslide debris

The lacustrine deposits represent the lakes fine-grained deposits formed after the formation of the Seymareh landslide dam. The vast range of these sediments are up to the downstream of Cham Borzu gorge and Maleh-Kuh Mountain range (up to 650 and 700 meters above sea level for Seymareh and Jaydar lakes) (Delchiaro et al. [2019a](#)) (Figure 20).



Figure 20 The lacustrine deposit of the Seymareh lake

Alluvial fans are mainly formed in the upstream of Seymareh landslide dam and in the Kabir-Kuh mountain range but there are some alluvial fans on the landslide debris surface (Figure 21). These alluvial fans originated from the drainage network of the basin, which, after reaching a low slope, or, in other words, exiting the valley and reaching the plain, formed the alluvial fans. The presence of alluvial fans in lacustrine sediments indicates the formation of some of these alluvial fans during the formation of Seymareh lake, while somewhere they formed also on the landslide debris.

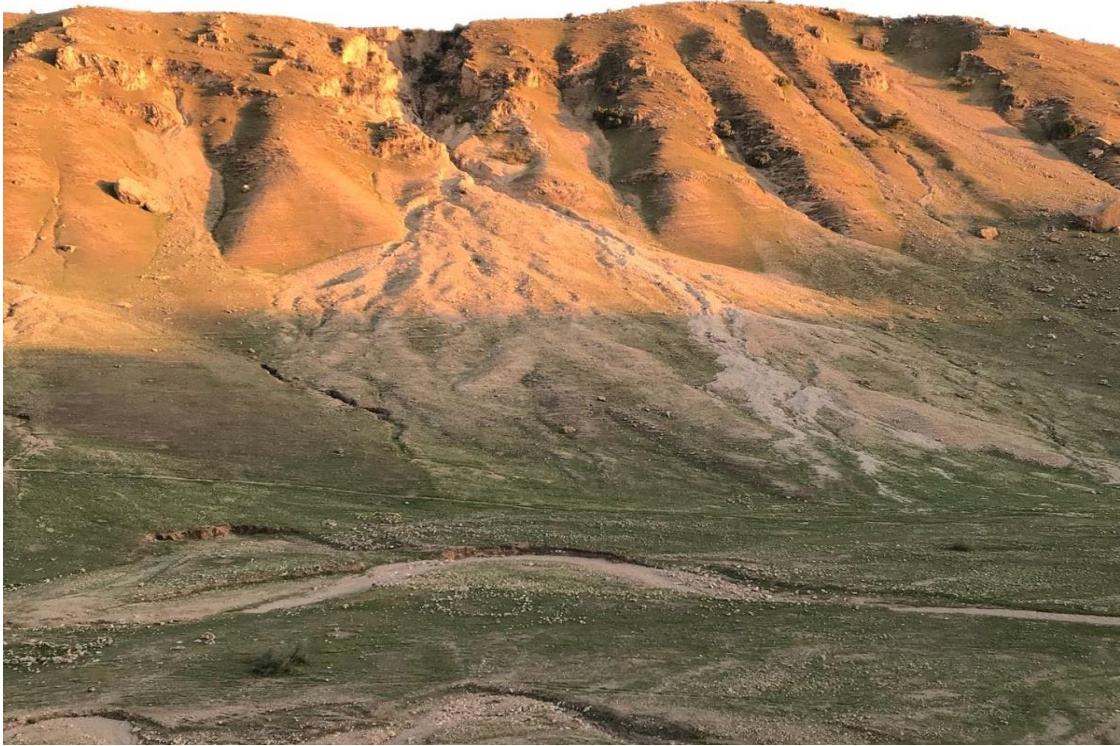


Figure 21 Alluvial fans on the Seymareh landslide debris

There are several denudation scarps on the Seymareh landslide debris which could be due to the combined effect of mechanical and chemical weathering and erosion by running water or wind (Figure 22).



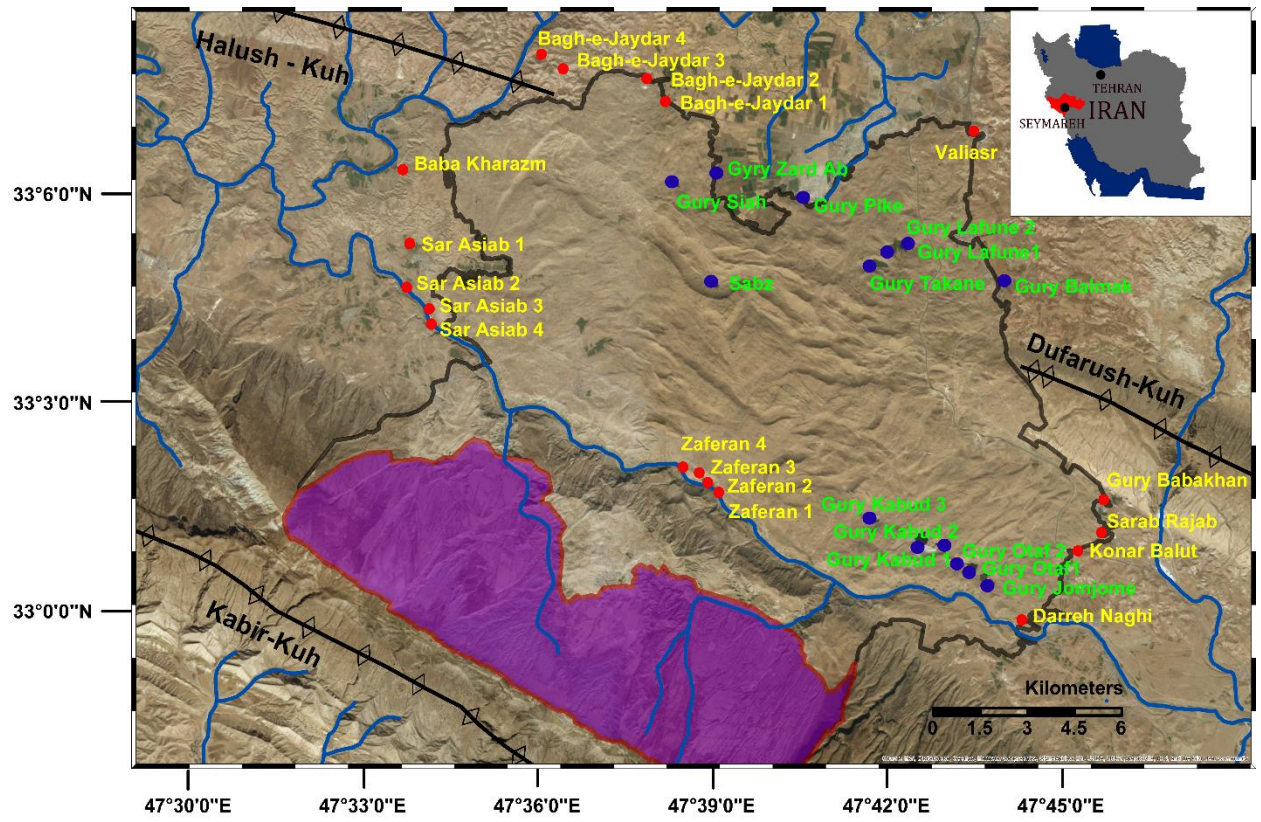
Figure 22 Denudation Scarp on the landslide debris

A ridge is a geomorphological feature consisting of elongated relief that form a continuous elevated crest for some distance. Ridges are usually termed hills or mountains as well, depending on size there are several main types of ridges (Karwariya 2013). On the Seymareh landslide debris there are many ridges which are formed due to the landslide debris emplacement or because of erosion processes (Figure 23). In the next chapter the ridges formation on the landslide debris will be discussed more in details.



Figure 23 Ridges on the Seymareh landslide debris

There are six lakes in the southeast region of the landslide debris in the downstream (Figure 24) known as Tang-e-Fanni lakes. The lakes are fed by springs (Watson and Wright 1969) (Figure 24) close to them in the downstream as well as a series of spring along the gorge in Zaferan area. There are also a set of three lakes in the northeastern lobe of the debris west of the Valiasr village and are known as Valiasr lakes. These lakes are also fed by springs (Watson and Wright 1969). The detail of all lakes and springs in the study area are presented in Table 3 and Table 4.



Legend


- | | | |
|------------------------------------------------------------------------------------------------------|---------------------------------------------------------------------------------------------|---------------------------------------------------------------------------------------------------|
|  Landslide Debris |  Springs |  Fold Axis |
|  Scar Area |  Lakes |  Main Streams |

Figure 24 Springs and lakes location

Table 3 Details of the lakes on the the Seymareh landslide debris

Lakes Name	H (Above sea level)	Type of the lakes	Situation	Max depth (m)	Perimeter (m)	Volume (m ³)	Discharge Regime	Water quality	Max Dimension (km)	Min Dimension (km)	Area (hectare)
Gury Pike	688	Natural	Dry	0	350	0	Seasonal	Salty	0.14	0.6	1
Gury Lafune 1	710	Natural	Wet	6	900	360000	Permanent	Fresh Water	0.26	0.24	6
Gury Lafune 2	710	Natural	Wet	2	400	20000	Permanent	Fresh Water	0.09	0.07	1
Gury Takane	705	Natural	Wet	10	1200	1000000	Permanent	Fresh Water	0.4	0.22	10
Gury Siah	761	Natural	Dry	0	380	0	Seasonal	Fresh Water	0.11	0.09	1
Gury Zard Ab	693	Natural	Dry	0	650	0	Seasonal	Fresh Water	0.3	0.1	3
Gury Otaf 2	501	Natural	Wet	7	700	420000	Permanent	Fresh Water	0.3	0.18	6
Gury Otaf 1	501	Natural	Wet	4	600	120000	Permanent	Fresh Water	0.2	0.08	3
Gury Balmak	750	Natural	Wet	1	8000	20000	Seasonal	Salty	3	2	20
Gury Kabud 3	500	Natural	Wet	10	750	70000	Permanent	Fresh Water	0.28	0.25	7
Gury Kabud 2	508	Natural	Wet	8	800	40000	Permanent	Fresh Water	0.3	0.2	0.5
Gury Kabud 1	508	Natural	Wet	8	900	40000	Permanent	Fresh Water	0.3	0.2	0.5
Gury Jomjme	484	Natural	Wet	8	1100	720000	Permanent	Fresh Water	0.3	0.25	9
Gury Golam Suze	720	Natural	Dry	0	500	0	Seasonal	Salty	0.1	0.02	0.2
Sabz	650	Natural	Dry	No data	No data	No data	No data	No data	No data	No data	No data

Table 4 Details of the Springs around the Seymareh landslide debris

Springs Name	H	Q_2000 (m ³ /s)	Q_2018 (m ³ /s)
Baba_Kharazm	578.99	15	5
Bagh-e-Jaydar1	715.18	5	1.2
Bagh-e-Jaydar2	727.94	2	2.9
Bagh-e-Jaydar3	873.04	No Data	0.8
Bagh-e-Jaydar4	739.22	No Data	1.6
Darreh Naghi	437.01	5	0.5
Gury Babakhan	560.057	10	4
Konar Balut	497.73	20	1
Sar Asiab 1	578.36	25	5
Sar Asiab 2	529.99	No Data	1
Sar Asiab 3	507.21	No Data	0.5
Sar Asiab 4	502.959	No Data	1.5
Sarab_Rajab	500	15	1.5
Valiasr	718.84	No Data	1
Zaferan1	494.34	25	6
Zaferan2	497.55	20	9
Zaferan3	471.76	No Data	5
Zaferan4	443.15	No Data	7

In the southeast part of landslide debris, where Tang-e-Fanni lakes are spaced apart, there are extensional features in both sides of the lakes. These extensional features start with a short distance from both sides of the lake and ends toward the center of the lakes. The scarp of these extensional features has 1 to 5 m height, 5 to 10 m width and 1 to 3 m depth. The reason that these extensional trenches are formed could be because of solution of the formation at the base of the landslide debris or the settlement of landslide debris at that region. These extensional trenches are shown in Figure 25, Figure 26 and Figure 27.



Figure 25 Extensional trenches on the landslide debris



Figure 26 Extensional trenches on the landslide debris



Figure 27 Extensional trenches on the landslide debris

Chapter 3- Morphometric analysis

3.1 Material and methods

In the last decades, Geographic Information Systems (GIS) and DEMs allowed the detailed analysis of land surface by remote surveying. Before the introduction of Digital Elevation Models (DEMs), landforms were only manually identified by means of surveys when available through interpretation of aerial photographs (Schillaci et al. 2015) but over the years, scientists have conducted research and shown the usefulness of spatial technologies, remote sensing and field studies in landform mapping and understanding of geomorphic processes (Karwariya et al. 2013).

Landforms are both the result of past geomorphic processes and the stage for present geomorphic processes which reshape it again for future geomorphic processes (Swanson et al. 1988; Dehn et al. 2001). Sparks (1986), Etzelmüller and Sulebak (2000) propose a switch from process study as the key for understanding landforms to morphologic description as key for assessment of process. Summerfield (1991) emphasizes both the form and the processes which create the form as equally important subjects for geomorphology and argued the need to think about physical processes and explain how forms are related to them.

Within geomorphology itself a distinction can be drawn between a qualitative and a quantitative branch (Straumann et al. 2009). The latter refers to a specific way of exploring geomorphological questions and takes its roots in the early debates between qualitative and quantitative approaches. Geomorphology now fundamentally relies on quantification to answer different questions, to characterize the magnitude and frequency of events and critical geomorphic phenomena, and to assess the evolution and organization of forms and their connections (Piégay 2017). Therefore, quantification is helpful for understanding land surface complexity as it can provide a wider set of solutions and make interpretations more robust.

In the present thesis, Aerial Photos of Geographical Mapping Organization of Iran related to the Seymareh landslide debris taken in 1955 and 2002 with the scale of 1:55000 and 1:40000, have been interpreted respectively in a preliminary step using stereoscope by separating the area of the debris in terms of tone, texture and structure characteristics.

Geological maps with the scale of 1: 100000 and 1: 250000 of Geological Survey of Iran, the digital elevation models of the area with a resolution of 10 and 30 meters² and Google Earth

² The digital elevation models of the area with a resolution of 10 meters was interpolated from vector topographic data and 30 meters is the free available SRTM

images (CNES/Airbus from 2011 to 2017) for identification of different geomorphological features and measuring the blocks size were observed and interpreted.

This research required extensive field surveys, which were carried out in two 3-month periods, June to September 2017 and May to August 2018. To carry out the surveying activity, topographic map 1: 25000 of Geographical Mapping Organization of Iran and Google Earth image (CNES/Airbus 2017) for planning the routes been used. Field surveys have been performed for detection of the boundary surface between the landslide debris and the bedrock and of different outcrop location inside landslide debris, ground truthing of interpretations made from remotely sensed datasets, identifying the location of springs and measuring their discharge, sampling for laboratory tests, measuring the density of the debris at the surface in different part of the landslide debris for permeability tests. During the field surveying some more geomorphological features have been recognized and a part of blocks identified by remote surveying, some more blocks were measured by tape.

The ArcGIS 10 software package was used to manage and analyze the data acquired through remote surveying and field survey. A specifically designed geodatabase was populated with surface features on the landslide debris, firstly surveyed by remote sensing analysis and successively verified in the field. As the flowchart reported in Figure 28 shows, the structure of this geodatabase has been created in the Arc Map environment with line, point and polygon feature classes. Point features have been used to represent the location and specific details of the features that were too small to be represented as lines or polygons as well as point locations (such as GPS observations). Linear elements have been used in this research to represent the shape and location of the geographic objects and Polygon features represents the shape and location of homogeneous features. The reference system considered in this research is UTM projection system, with datum WGS84 (World Geodetic System of 1984) and zone 38North.

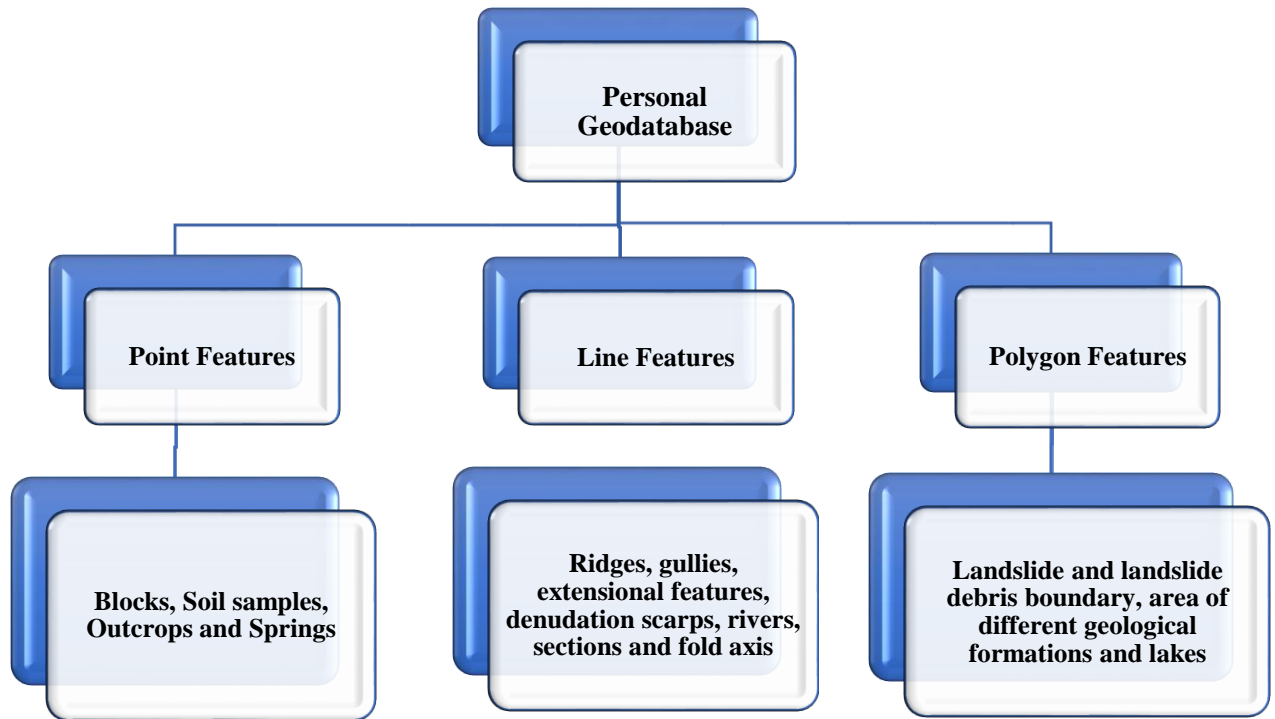


Figure 28 Flow chart illustrating the structure of the specifically designed geodatabase

Among the instruments for the analysis of the field survey and with the aim of zonation, the calculation procedure of the main spatial analysis tools is described in the following.

Once the significant surface features have been recognized, their spatial density has been calculated. We calculated the density of linear features (e.g. ridges and gullies) by Line Density tool in GIS, for which an output cell and a search radius should be defined. The density tool calculates the density of all linear features inside the defined circle around each raster cell center using the search radius. The length of the portion of each line that falls within the circle is multiplied by its population field value. These values are summed, and the total is divided by the circle's area.

Line Density tool calculates the density in units of length per unit of area. Figure 29 and Line Density Equation illustrates this concept:

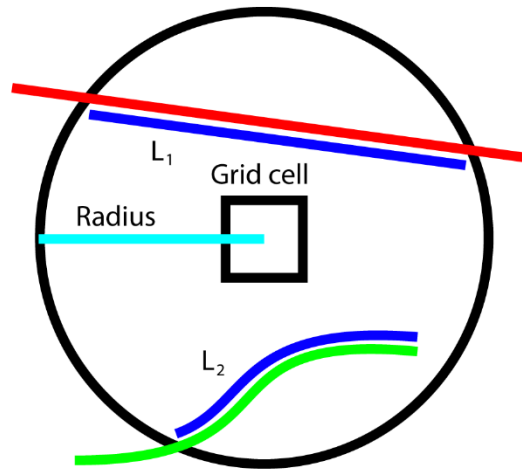


Figure 29 Scheme of how the Line Density tool operates

In the illustration above, a raster cell is shown with its circular neighborhood. Lines L₁ and L₂ represent the length of the portion of each line that falls within the circle. The corresponding population field values are V₁ and V₂. Thus:

$$\text{Line Density} = \frac{(L_1 * V_1) + (L_2 * V_2)}{(\text{Area of circle})} \quad \text{Equation 1 Line Density}$$

If a population field other than NONE is used, the length of the line is considered to be its actual length times the value of the population field for that line.

The density of point features (e.g. blocks) was calculated by Point Density tool in GIS, for which an output cell and a search radius should be defined. The Point Density tool calculates the density of point features around each output raster cell. Conceptually, by defining a neighborhood around each raster cell center, all point features that fall within the neighborhood are summed and divided by the area of the neighborhood. Increasing the radius will not greatly change the calculated density values. Although more points will fall inside the larger neighborhood, this number will be divided by a larger area when calculating density. The main effect of a larger radius is that density is calculated considering a larger number of points, which can be farther from the raster cell. This results in a more generalized output raster. Figure 30 and Point Density Equation show this concept.

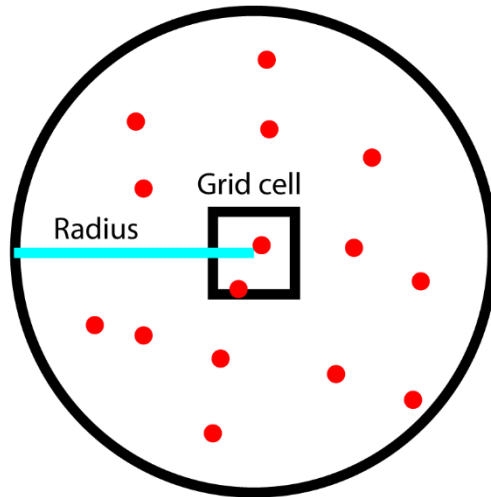


Figure 30 Scheme of how the Point Density tool operates

$$Point\ Density = \frac{(Number\ of\ points)}{(Area\ of\ circle)} \qquad \qquad \qquad Equation\ 2\ Point\ Density$$

The Aggregate tool resamples an input raster to a coarser resolution based on a specified aggregation strategy (Sum, Min, Max, Mean, or Median).

Conceptually, the tool works as follows:

1. It multiplies the cell resolution of the input raster by the factor specified by the cell factor parameter. The resulting value corresponds to the cell resolution of the output raster.
2. It maps the spatial extent of the output cells onto the input raster.
3. It identifies the cells on which to perform the aggregation calculations. Cell locations from the input raster that fall within the extent of an output cell are included in the calculations for determining that cell's output value.
4. It calculates the output value by determining the sum, minimum, maximum, mean, or median value of the cells from the input raster that fall within the output cell's spatial extent.

Figure 31 shows this concept.

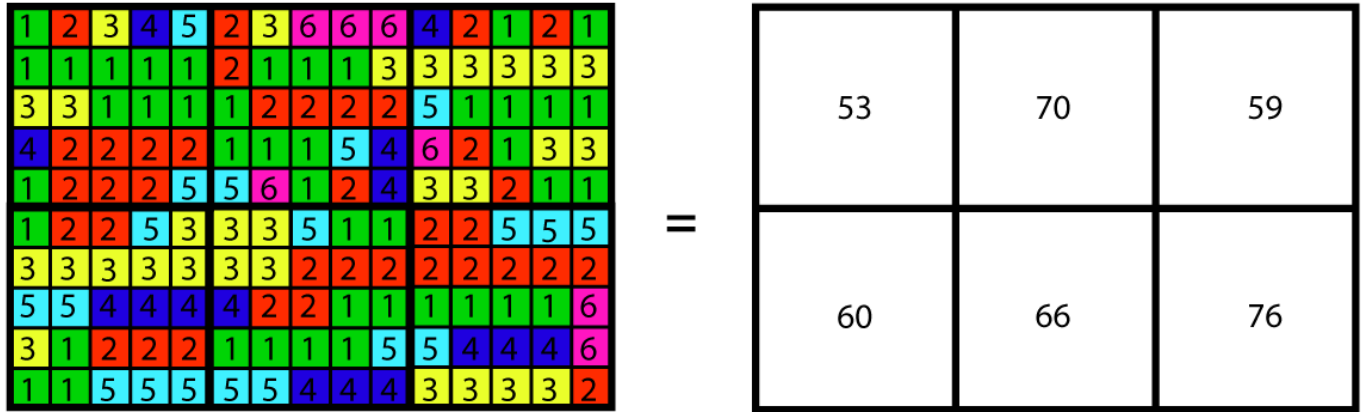
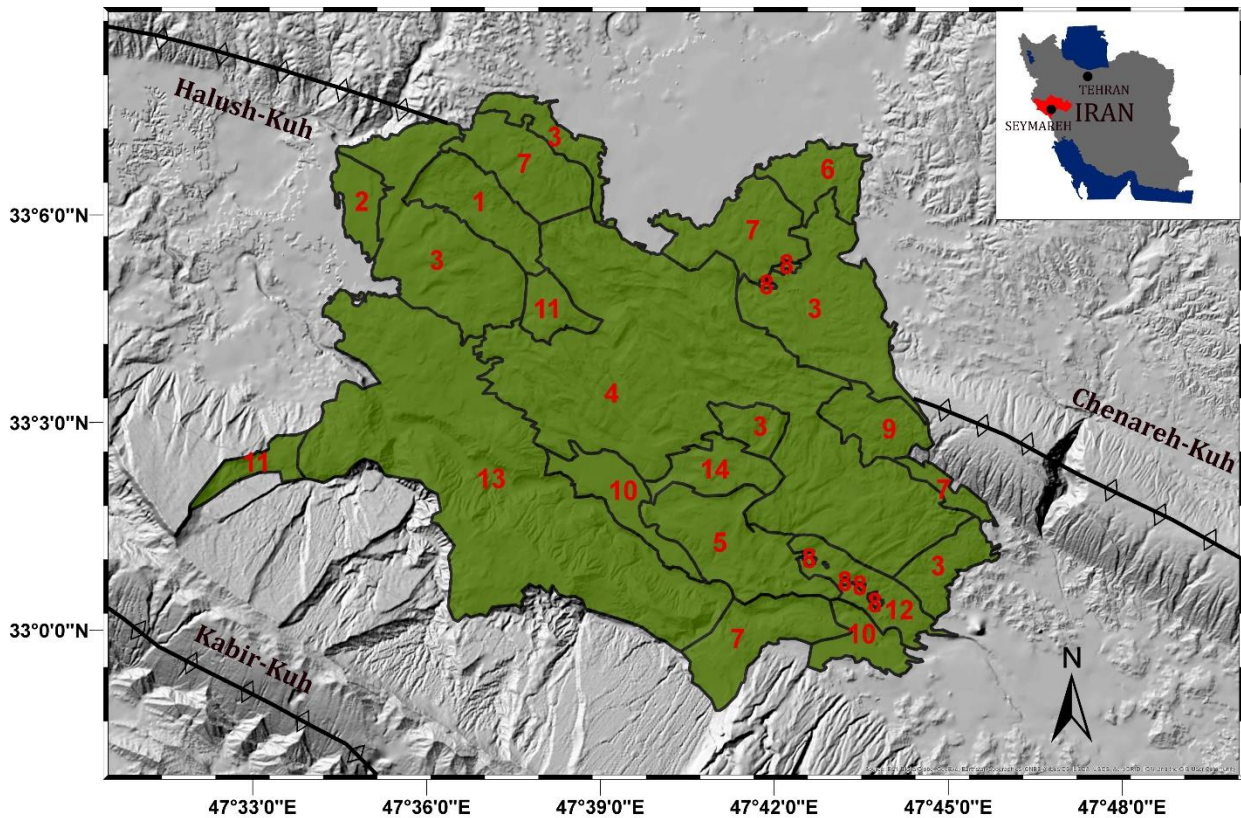


Figure 31 Scheme of how the Aggregate tool operates

The Reclassification tools reclassify or change cell values to alternative values using a variety of methods. You can reclass one value at a time or groups of values at once using alternative fields; based on a criterion, such as specified intervals (for example, group the values into 10 intervals); or by area (for example, group the values into 10 groups containing the same number of cells). The tools are designed to allow you to easily change many values on an input raster to desired, specified, or alternative values. When applying an alternative value to an existing value, all the reclassification methods apply the alternative value to each cell of the original zone. No reclassification method applies alternative values to only a portion of an input zone.

If the input raster has an attribute table, it will be used to create the initial reclassification table. If the input raster does not have an attribute table, a reclassification table will be created for it by first applying geoprocessing environment settings, such as extent and cell size, and scanning the raster. When the input raster is a layer from the Table of Contents, the default reclassification table will import the unique values or classified break values as specified by the layer symbology; otherwise, the reclassification table will default to natural breaks with nine classes. By interpreting the aerial photos related to the Seymareh landslide debris surface, in terms of tone, texture and structure characteristics, the landslide debris surface was divided in 14 zones (Figure 32). The description of each zone is presented in Table 5.



Legend

- Landslide Debris Zones
- Fold Axis



Figure 32 The landslide debris zonation based on the tone, texture and structure of the aerial photos

Table 5 Different zones on the landslide debris based on tone, texture and structure of aerial photos

Tone	Texture	Structure	Zone Number
Between white and dark gray	Mixed	Irregular	1
Between white and medium gray	Mixed	Irregular punctual and Irregular Linear	2
Between very light gray and medium gray	Mixed	Irregular punctual and Irregular Linear	3
Between very light gray and dark gray	Mixed	Irregular punctual and Irregular Linear	4
Between very light gray and medium gray	Mixed + Prevalent fine	Irregular punctual and Irregular Linear	5
Between very light gray and medium gray	Mixed + Prevalent fine	Irregular punctual	6
Between very light gray and medium gray	Mixed	Irregular punctual	7
Lake	Lake	Lake	8
Between white and light gray	Mixed	Irregular punctual and Irregular Linear	9
Flat	Flat	Flat	10
Between light gray and medium gray	Mixed	Irregular punctual and Irregular Linear	11
Between white and medium gray	Mixed	Irregular linear	12
Between white and light gray	Fine	Irregular linear	13
Between very light gray and dark gray	Mixed + Prevalent fine	Irregular punctual and Irregular Linear	14

Watershed features on the Seymareh landslide debris was extracted from DEM using Arc Hydro Tools. The procedure used for watershed delineation in Arc Hydro involves several steps accessed through the toolbar menus. The first step was DEM Reconditioning. DEM Reconditioning is an implementation of the AGREE method of hydrological correction. AGREE is a surface reconditioning system for DEMs. This function modifies its initial value by introducing a linear feature class (such as a hydrographic network) to DEM. Reconditioning is necessary to raise the base level of the DEM values to prevent negative values in the DEM (Li 2014). In this process, the original DEM was input, and the main streams were also input as a linear feature class. The next step was Fill Sink. This function fills the sinks in the raster. If a cell is surrounded by larger cells, the water is surrounded by this cell and it cannot flow. This function corrects elevation values to eliminate these sinks. Once sinks were filled, the flow direction was calculated using Flow Direction function. The flow direction by eight values indicate eight possible direction of the flow in each cell. Flow accumulation network was then created based on the flow direction using the Flow Accumulation function. This function calculates the flow density and represents the accumulated weight of all cells flowing into each downslope cell in the output raster. With the Stream Definition function, all the cells in the input flow accumulation grid that had a value greater than the given threshold grid was given a value of 1 and defined as stream grid. After linking the stream grid using the Stream Segmentation function, the Stream Link grid map was produced. The resulting link grid was used in the next step to generate a catchment grid based on the values held by each stream segment. The number of catchments was equal to the number of stream segments defined in the previous step. These catchment grids were converted to polygon vector features in the next step, with single cell catchments automatically dissolved within the process topology. Additionally, the link grid from earlier processing was converted to a line feature class using the drainage line-processing tool in the next step. Each of these line segments is assigned an ID value corresponding to the catchment polygon in which it resides. In the next step by Adjoint Catchments Processing tool, the cumulative upstream area of each stream segment that was not a headwater segment was represented. In the next step by Drainage Points Processing, common points between drainage line and watersheds were extracted. In a final step, the longest flow path for each watershed was calculated by Longest Flow Path for Catchments tool.

The minimum eroded volume of the landslide debris by using watershed on the landslide debris and DEM has been calculated as following steps: using Feature Vertices to Points tool, the

watershed polygon of the landslide debris was converted to point file. Then by Extract Values to Points tool the elevation values of the points was extract from the DEM. Using Create TIN tool, a TIN surface was created and converted to a raster. The raster file was then clipped to the watershed boundary and the difference between clipped raster file and DEM topography was calculated. In a final step, the minimum eroded volume of the Seymareh landslide debris was calculated by multiplying the values of each pixel in the difference raster per area of a single pixel (which is 100 m²) as it resulted from this computation, the minimum eroded volume of the Seymareh landslide debris was 4.98 km³.

Several studies have been performed so far on the Seymareh landslide, but few studies focused on the Seymareh landslide debris as a possible indicator of its emplacement kinematics after the slope collapse (Rouhi et al. 2019). For this PhD research, a new statistical approach is applied which involves a detailed geomorphological study using Geographic Information System (GIS), Google Earth Images @ CNES/Airbus 2017, aerial photo interpretation and field investigation to identify regions with original and deformed landforms on the Seymareh landslide debris and to derive indicators of its emplacement kinematics. In a first step, the landslide debris boundary, as well as the ridges, gullies, denudation scarps, extensional features and blocks on the landslide debris have been mapped in GIS through the interpretation of satellite optical images (Google Earth and aerial photos). In a second step, a field survey been carried out to confirm the presence of all recognized features mapped.

The coincidence of ridges, gullies and blocks at different location on the debris give clues that there is a relationship between these features that, by defining some conditions, could allow to identify the original and reshaped landforms on the debris. Therefore, primary deformational elements (ridges) secondary landforms (gullies) and blocks (larger than 10m) have been chosen to be analyzed based on a new statistical approach. The flowchart reported in Figure 33 shows the procedures of new statistical approach for recognition of primary or secondary zones.

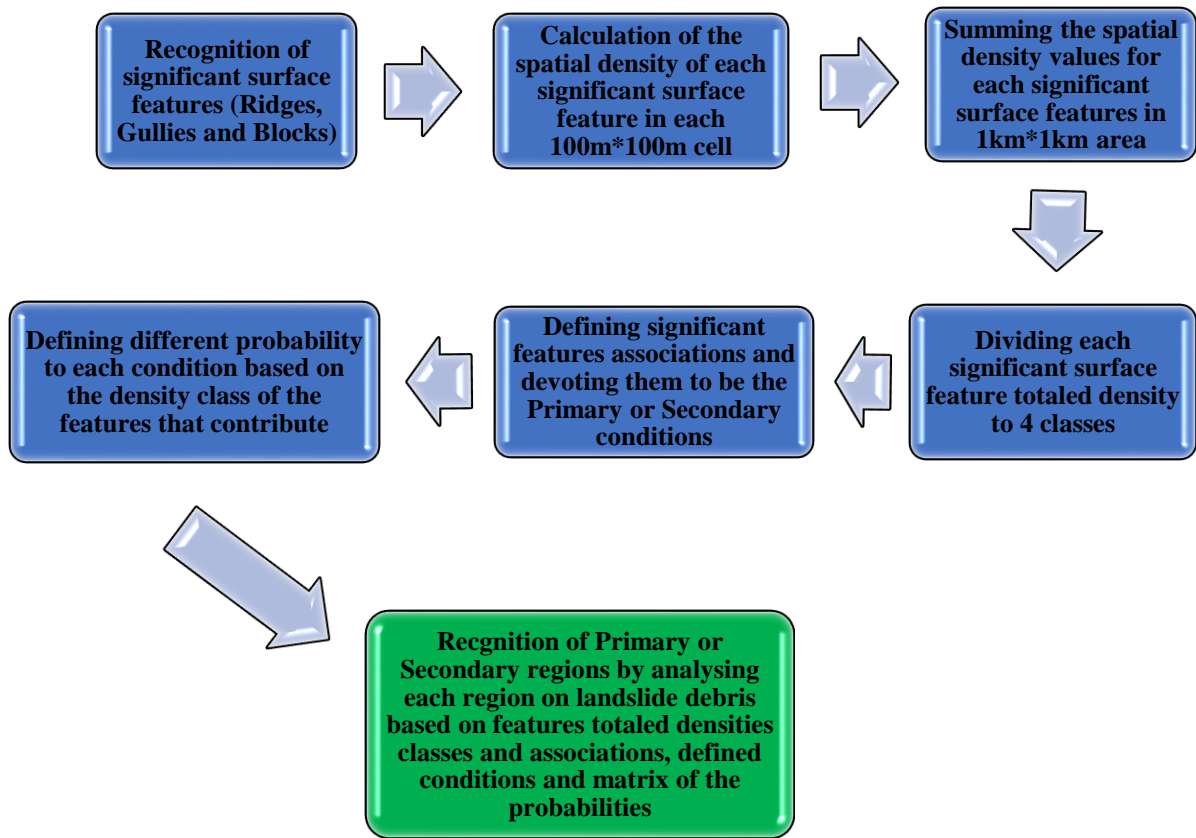


Figure 33 Flowchart showing the here adopted procedure for recognition of primary or secondary region

Spatial densities of the ridges, gullies and blocks were calculated with a defined 100m*100m output raster cells to proceed in the next steps. Different values for the neighborhoods around output raster cells from their center were defined to be considered in densities calculation of the ridges and gullies, based on their mean length. These values were defined as 250 and 200m for the ridges and gullies, respectively. Regarding the long dimensions of ridges and the distance between two ridges the value for their population field were chosen as their length. Since the dimensions of the gullies were long like the ridges, the values of population fields for them were also chosen as their length. The blocks mean length were 15m and for having more generalized output raster in the block's density calculations, value of 150m for the neighborhoods around output raster cells which was close to the ridges and gullies neighborhood calculation area was assigned. Table 6 shows the density ranges adopted for ridges, gullies and blocks.

Table 6 Density ranges adopted for ridges, gullies and blocks

Ridges density range (km ² /km ²) *1000	Gullies density range (km ² /km ²) *1000	Blocks density range (Number of blocks/km ²)
0-8005.03	0- 18,285.70	0- 254.64

As the Seymareh landslide debris area is huge, densities calculation for each 0.01km² was not enough for zonation of each feature. Therefore, for proceeding the analysis, by using aggregate tool in GIS the area of each cell was extended to 1 km². Using Aggregate tool in GIS and by summation of the density values of all cells in 1km², a new zonation was done for each feature. Table 7 shows the range of totaled density value for each 1km².

Table 7 The range of totaled density value for each 1km²

Aggregate ridges density range (km ² /km ²) *1000	Aggregate gullies density range (km ² /km ²) *1000	Aggregate blocks density range (Number of blocks/km ²)
0-320,724	0- 550,181	0- 4,937

Once surface features densities for each 1km² area were calculated, for each surface feature, the density was classified to 4 groups. These classifications are present in Table 8.

Table 8 The ridges, gullies and blocks totaled densities classes

Class	∑ Ridge density range (km ² /km ²) *1000	∑ Gullies density range (km ² /km ²) *1000	∑ Blocks density range (Number of blocks/km ²)
1	0	0	0
2	0 - 33,959.00	0 - 15,102.99	0 - 309.79
3	33,959.001- 83,010.89	15,102.991- 71,199.85	309.791- 910.01
4	83,010.891- 320,723.90	71,199.851 - 550,180.68	910.011- 4,937.33

Once performed the classification, the Reclassification tool in GIS been used to simplify the information in the raster and to group together the cells with the same range of density for each surface feature into one class.

As described before, on the Seymareh landslide debris there are primary (original) and secondary (reshaped) landforms because of erosion process by different natural phenomena and differential movement between the landslide debris and the underlying material. Ridges, gullies and blocks are indicative of different kinds of phenomena. Combination of them in a logical way can provide information related to the original and modified regions on landslide debris. In the current study among all recognized landforms, the ridges, gullies and blocks have been chosen for this new statistical approach because the combination of them can represent in the best way the original and deformed regions on the landslide debris.

After zonation based on spatial density of the ridges, gullies and blocks, to attribute a specific landform association to a primary or secondary region of the landslide debris the following criteria were assumed. The presence of ridges with no gullies (Figure 34-c₁) and ridges with blocks on the flanks of ridges (Figure 34-c₁, c₄) are attributed to regions with original surface features, i.e. that are related to the landslide event and have not been significantly eroded up today. The presence of blocks with no evidence of ridges (Figure 34-c₂) are attributed to the middle and distal area that are preserved with respect to the original features of the landslide debris. Also, the presence of blocks with gullies (Figure 34-c₃) indicates preserved regions because the formed gullies are not deepened and this means that channeled waters had not the suitable energy to move blocks and carve ridges. Based on these criteria, four landform associations were defined for recognition of regions which are not eroded and have the original morphology. These conditions are considered as "primary conditions" (Table 9). On the contrary, the coincidence of ridges and gullies in some locations can be attributed to a secondary landform evolution, i.e. the ridges are formed through erosion by gullies (Figure 35-c₅), the presence of ridges with no blocks on its flanks is a evidence that these ridges are formed during erosion process by overflowing of water from upstream of landslide dam, torrent or storm (Figure 35-c₆), the presence of gullies with no blocks and ridges are representative of eroded area (Figure 35-c_{7,8}). These landform associations are representative of regions where the primary conditions were significantly modified because of channeled and sheet water erosion. In Table 9, four associations are defined based on these coincidences for recognition of the regions with "secondary conditions".

Eight landform associations are defined (Table 9) at all: four associations for recognition zones where the primary conditions can be attributed and four associations for recognition of zones where the secondary conditions can be attributed. Each of these associations are based on the aggregate density zonation of couples of surface features and has 3 probabilities (high, medium and low) depending on which class of ridges, gullies or blocks aggregate density that contributes. Table 10 shows probabilities of each conditions based on the classes of aggregate density that contribute.

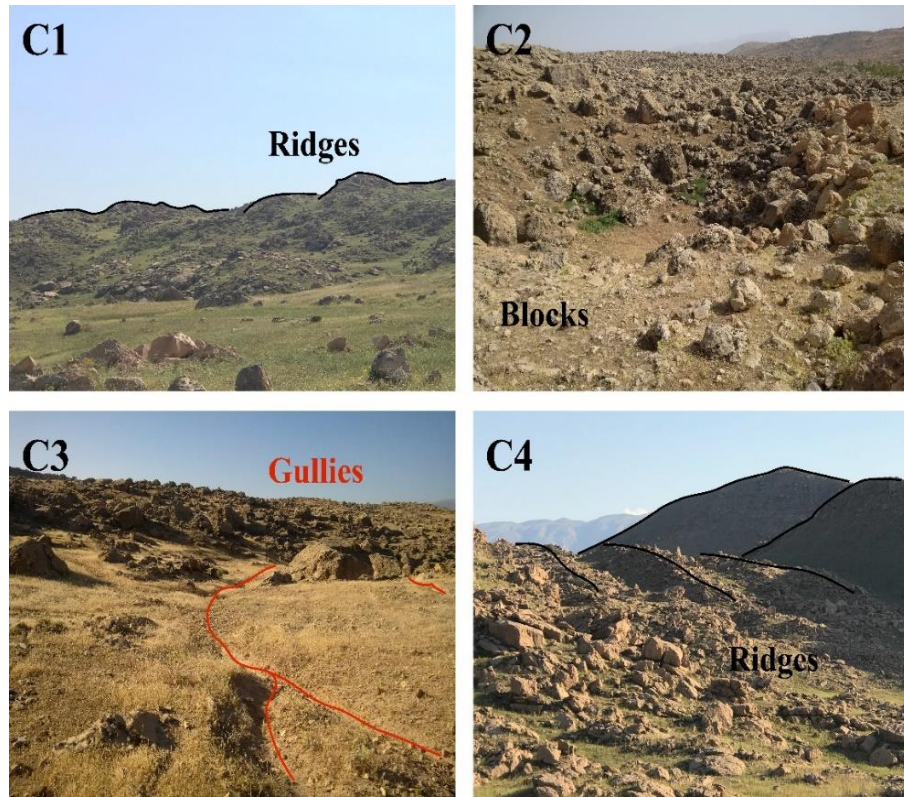


Figure 34 Examples of zones with different evidences for primary conditions deduced by considering different landform associations

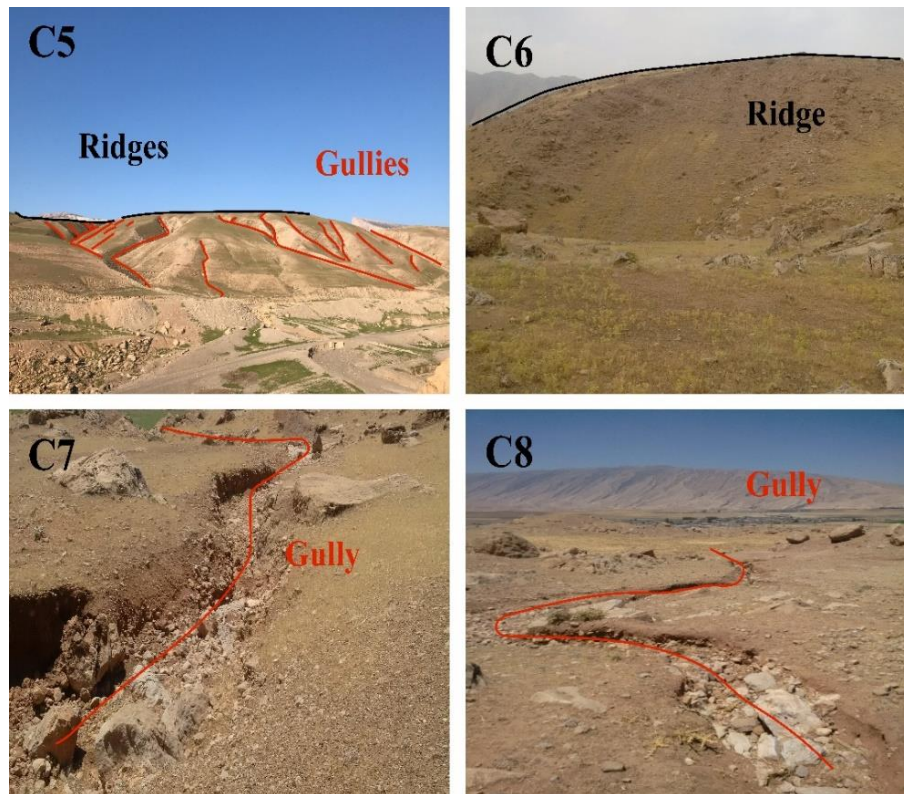


Figure 35 Examples of zones with different evidences for secondary conditions deduced by considering different landform associations

Table 9 Landforms associations for defining primary and secondary conditions

Primary conditions	Secondary conditions
C-1- Ridge - No Gully	C-5- Ridge - Gully
C-2- Block - No Ridge	C-6- Ridge - No Block
C-3- Block – No Gully	C-7- Gully - No Block
C-4- Block - Ridge	C-8- Gully - No Ridge

Table 10 Probability of landform associations which provide a rank to the attribution of primary or secondary conditions

Association number				Association number			
1	aggregate ridge density class	aggregate gully density class	Primary condition probability	5	aggregate ridge density class	aggregate gully density class	Secondary condition probability
	4	1	High		4	4	High
	4	2	Medium		4	3	Medium
	3	1	Medium		3	4	Medium
	3	2	Low		3	3	Low
2	aggregate block density class	aggregate ridge density class	Primary condition probability	6	aggregate ridge density class	aggregate block density class	Secondary condition probability
	4	1	High		4	1	High
	4	2	Medium		4	2	Medium
	3	1	Medium		3	1	Medium
	3	2	Low		3	2	Low
3	aggregate block density class	aggregate gully density class	Primary condition probability	7	aggregate gully density class	aggregate block density class	Secondary condition probability
	4	1	High		4	1	High
	4	2	Medium		4	2	Medium
	3	1	Medium		3	1	Medium
	3	2	Low		3	2	Low
4	aggregate block density class	aggregate ridge density class	Primary condition probability	8	aggregate gully density class	aggregate ridge density class	Secondary condition probability
	4	4	High		4	1	High
	3	4	Medium		4	2	Medium
	4	3	Medium		3	1	Medium
	3	3	Low		3	2	Low

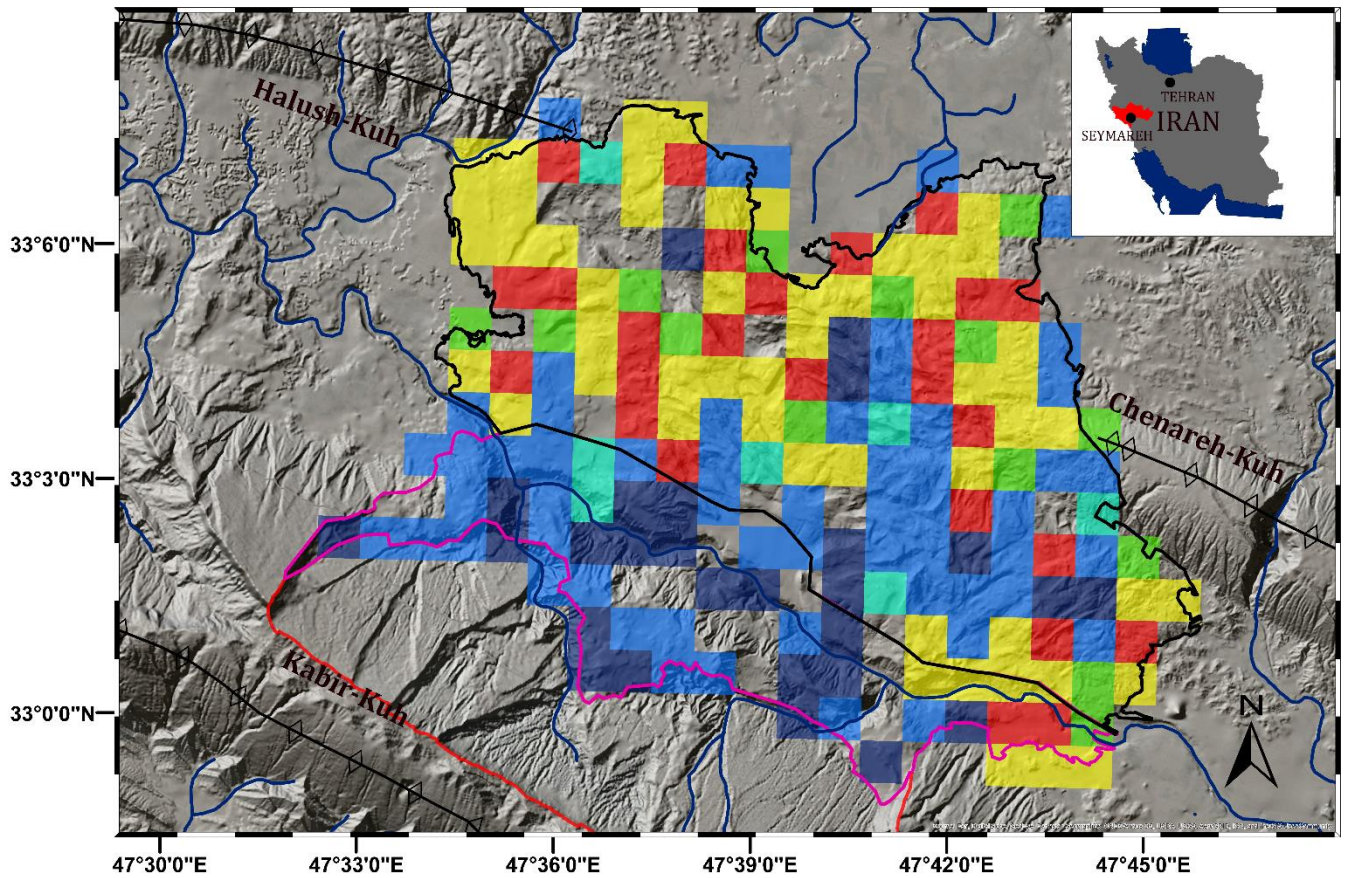
There are some zones of the landslide debris which match with more than one association and related probability. The final probability devoted to these zones is attributed referring to the matrix of probability (Matrix 1) reported in Table 11. As an example, if a zone matches with more than one primary condition with different probabilities, the zone was considered as primary zone with highest probability. If a zone matches with both primary and secondary conditions, in the case that both have the same probability, the zone was considered as secondary zone. Otherwise the zone was considered as one that has higher probability. There was only one exception, if the probability of both was low, because of low reliability, no probability was given to that zone and it was considered as uncertain zone.

Table 11 Matrix of probabilities

Primary Zone Probability			Secondary Zone Probability			Uncertain Zone
High	Medium	Low	High	Medium	Low	Undefined

	1	2	3	4	1	2	3	4	1	2	3	4	5	6	7	8	5	6	7	8	5	6	7	8
	P	P	P	P	P	P	P	P	P	P	P	P	S	S	S	S	S	S	S	S	S	S	S	S
	H	H	H	H	M	M	M	M	L	L	L	L	H	H	H	H	M	M	M	M	L	L	L	L
1P-H																								
2P-H																								
3P-H																								
4P-H																								
1P-M																								
2P-M																								
3P-M																								
4P-M																								
1P-L																								
2P-L																								
3P-L																								
4P-L																								
5S-H																								
6S-H																								
7S-H																								
8S-H																								
5S-M																								
6S-M																								
7S-M																								
8S-M																								
5S-L																								
6S-L																								
7S-L																								
8S-L																								
Undefined																								

Once the Seymareh landslide debris was zoned based on the ridges, gullies and blocks densities, the eight defined landform associations (Table 9), the related probability of conditions (Table 10) and the matrix of probabilities of Table 11 were applied to distinguish and map, the primary and secondary landform zones within the Seymareh landslide debris (Figure 36). As shown in Figure 36, secondary regions are more frequent nearer to the landslide scarp. The first cause could be the presence of the landslide debris related to the Pabdeh-Gurpi Formation in this area which is more erodible respect to the Asmari Formation debris. The second cause could be the lower altitude of the mentioned area respect to other areas on the landslide debris. Such a zonation allows to provide an interpretation for the kinematics of debris emplacement after the slope collapse. On the other hand, the distribution of secondary regions can be used as a basic criterion for discussing the landslide debris durability as well as the role of eroding factors over the time.



Legend



Figure 36 Zonation of original (primary) and reshaped (secondary) regions of the Seymareh landslide debris and related probability

After the landslide debris zonation, only the ridges within the primary zones were regarded as kinematic indicators. Therefore, the curvature of the ridges, just in the primary region was calculated and divided in four classes (Table 12). The ridges within the secondary zones were excluded as kinematic indicators.

Table 12 Ridges classification based on their curvature range

Class	Ridges curvature range (Ridge length/ length of a direct line from start to end of the ridge)
1	1.000111 - 1.005920
2	1.006252 - 1.015261
3	1.015400 - 1.032138
4	1.032722 - 1.303303

To perform such a computation, segment from start to end of the ridgeline were drawn and the direction perpendicular to this segment was regarded as a possible kinematic indicator, i.e. mass movement occurred parallel to the ridge arrow. All the ridges with curvature equal to 1 were excluded since they cannot represent the emplacement kinematics. The azimuthal directions of the kinematic indicators respect to the north were measured to classify them into four main classes including four subclasses (Table 13). Each subclass shows a range of azimuthal directions respect to the north. It was decided to classify the azimuthal direction of the kinematic indicators into the different classes because of the possibility that some parts of some ridges were eroded. By making these subclasses it was possible to recognize the ridges that had the same direction. Subclasses which were from the same class are shown in Figure 37 by the same colors.

Table 13 kinematic indicators classification based on their azimuthal direction ranges

Class	Ridge azimuthal directions ranges
1	0-22.5, 157.5-202.5, 337.5-360
2	22.5-45, 135-157.5, 202.5-225, 313-337.5
3	45-67.5, 112.5-135, 225-247.5, 292.5-315
4	67.5-112.5, 247.5-292.5

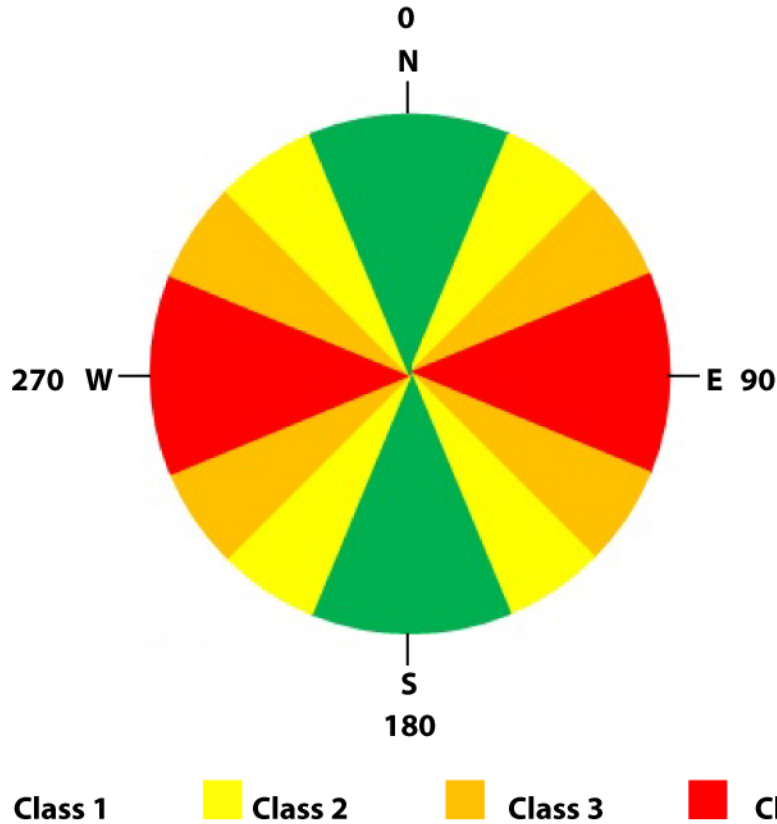


Figure 37 Graphical view of the azimuthal distribution of the kinematic indicators for each class

The flowing water direction only in the secondary zones can give clues for better interpreting the failure mechanism of the Seymareh landslide dam. Therefore, it was needed to recognize the flowing water direction on the surface of the Seymareh landslide dam only within the secondary zones. To this aim, the azimuthal direction of the gullies only on the secondary zones were calculated and divided in two classes (Table 14).

Table 14 Gullies classification based on their azimuthal direction ranges

Class	Gullies azimuthal direction ranges
1	0-90
2	90-180

3.2 Results

In a first step in this chapter of the thesis, the Seymareh landslide debris boundary, as well as the ridges, gullies, denudation scarps, extensional features, springs and blocks on the landslide debris are shown in GIS maps obtained through the interpretation of satellite optical images (Google Earth and aerial photos) followed by a field survey carried out to confirm the presence of all recognized landforms mapped in Figure 38.

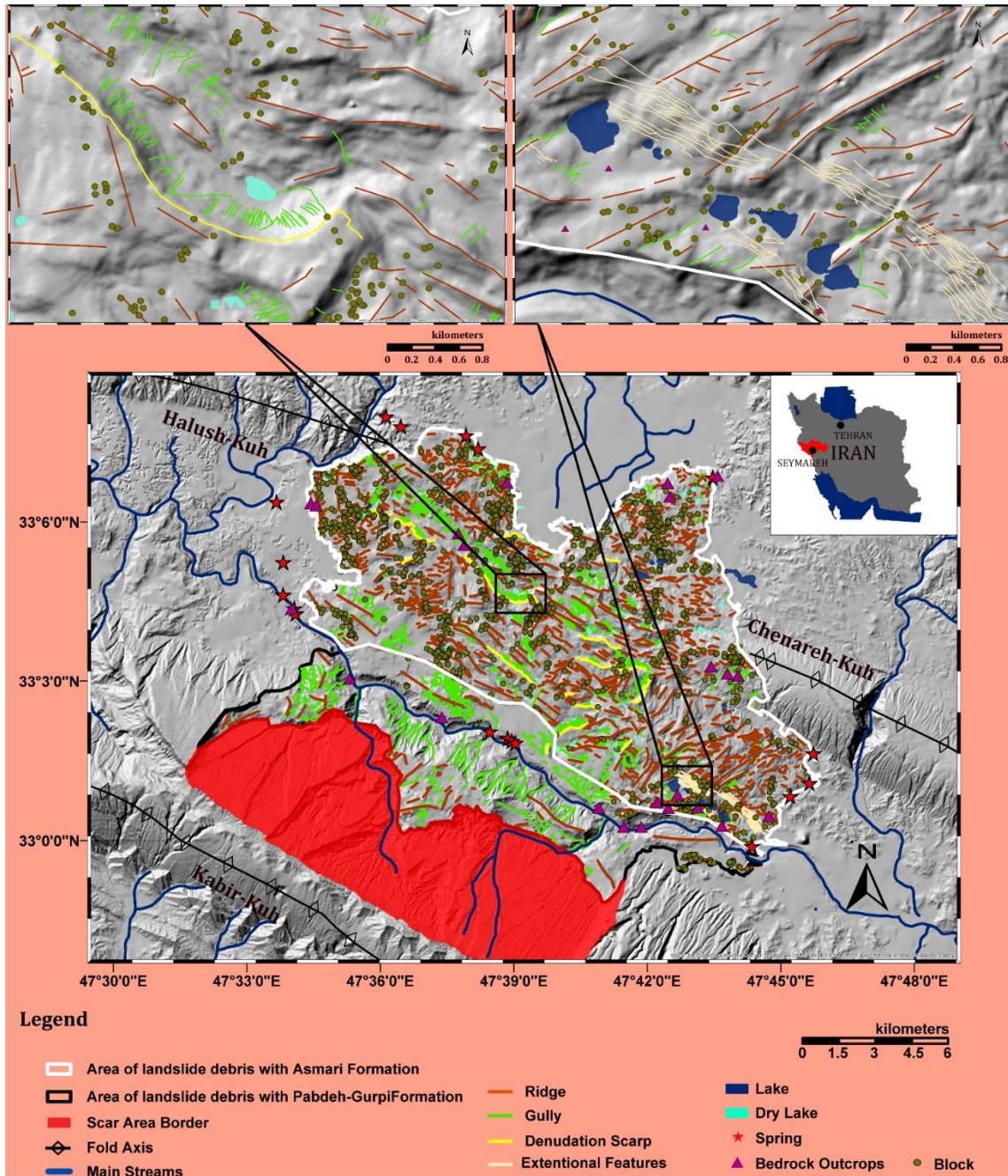


Figure 38 Geomorphological map including the main landforms surveyed within the debris of the Seymareh landslide

Spatial density of ridges in each 0.01km² were calculated using line density subset of spatial analyst tools in GIS, and then density values in each square kilometer were summed and divided in four classes (Table 8). In this way the Seymareh landslide debris was divided in four zones based on the distribution of the ridges. As it can be seen in Figure 39, the density of ridges in the middle portion of the debris is more intense than in other zones. It means that during the landslide debris emplacement, part of the debris dissipated its energy over passing the two anticlines of Chenareh-Kuh and Halush-Kuh and the rest of debris swept back into the Seymareh paleo valley. This also justify the lower distribution of ridges at distal and perimetral areas.

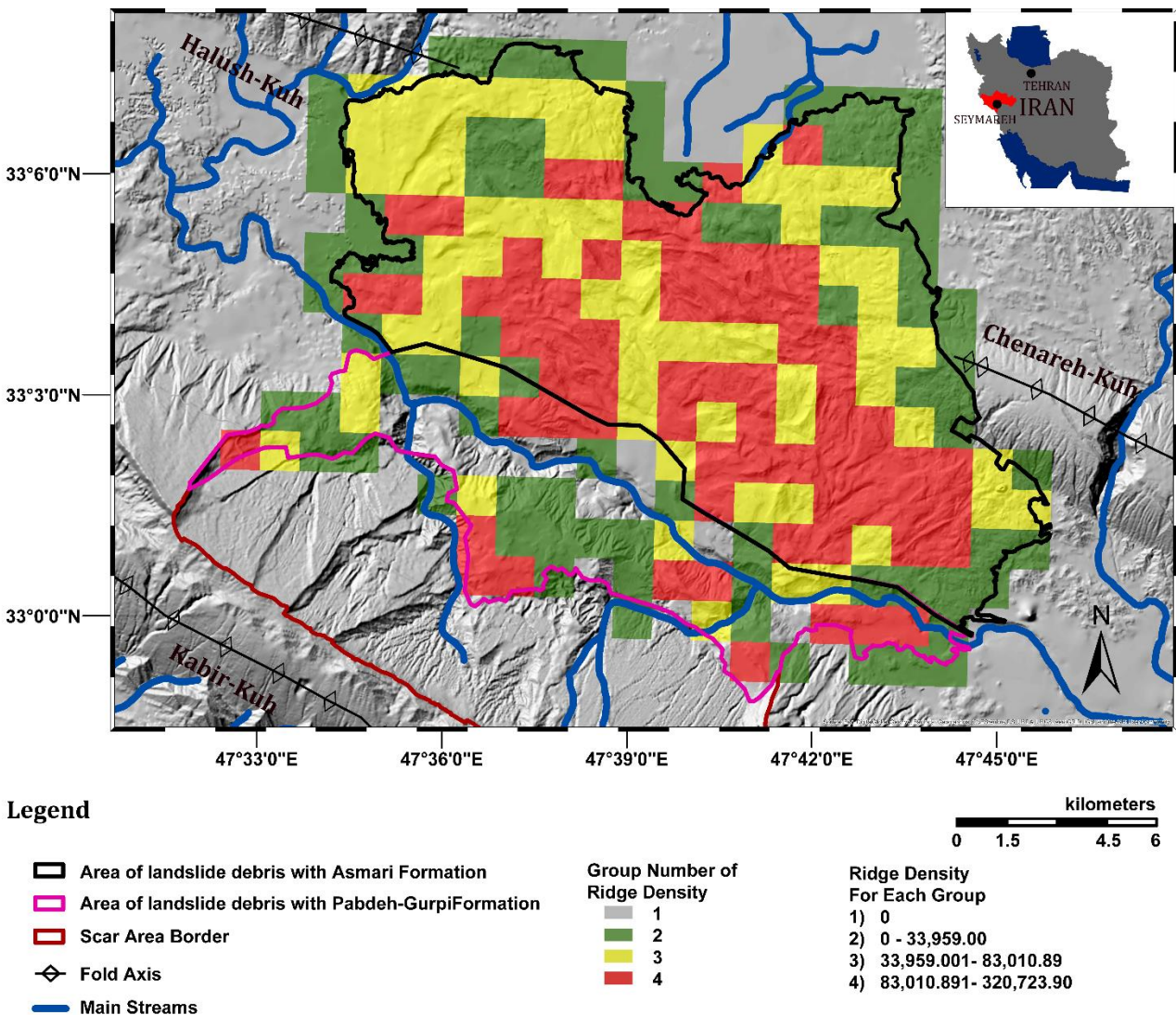
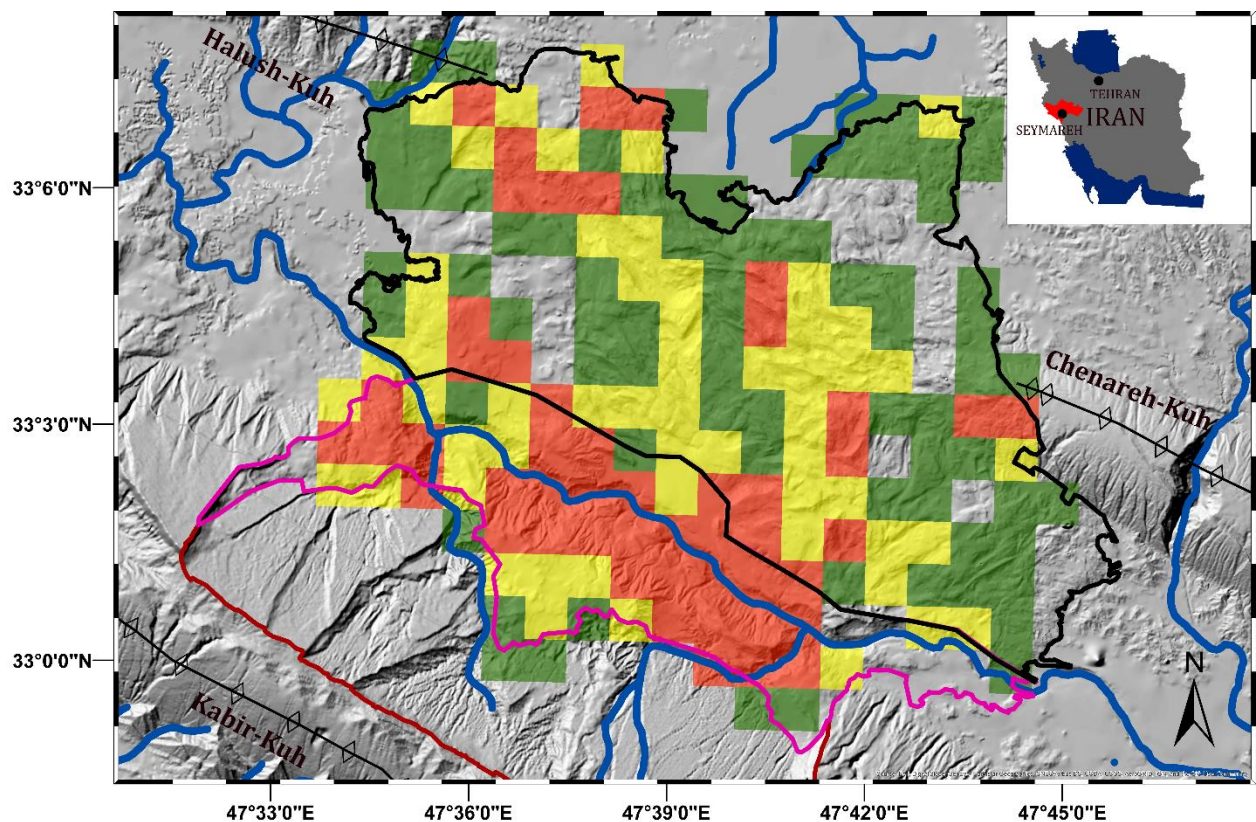


Figure 39 Ridges density zonation

Spatial density of the gullies in each 0.01km² were calculated using line density subset of spatial analyst tools in GIS and then density values in each square kilometer were summed and divided in four classes (Table 8). Figure 40 shows that the density of gullies in the proximity of the detachment area as well as of the distal area in the NW part of the debris are higher, indicating that the erosion in this area was more intense than in other parts. The reason could be the presence of the landslide debris related to the Pabdeh-Gurpi Formation in these areas which is more erodible respect to the Asmari Formation debris. In the area along the present Seymareh River there is the highest density of gullies that can be related to the landslide dam cutting. The mentioned area has lower altitude respect to other areas on the landslide debris. Where density of gullies is lower, the density of blocks and ridges increases, and the depth of the gullies decreases. Therefore, it can be



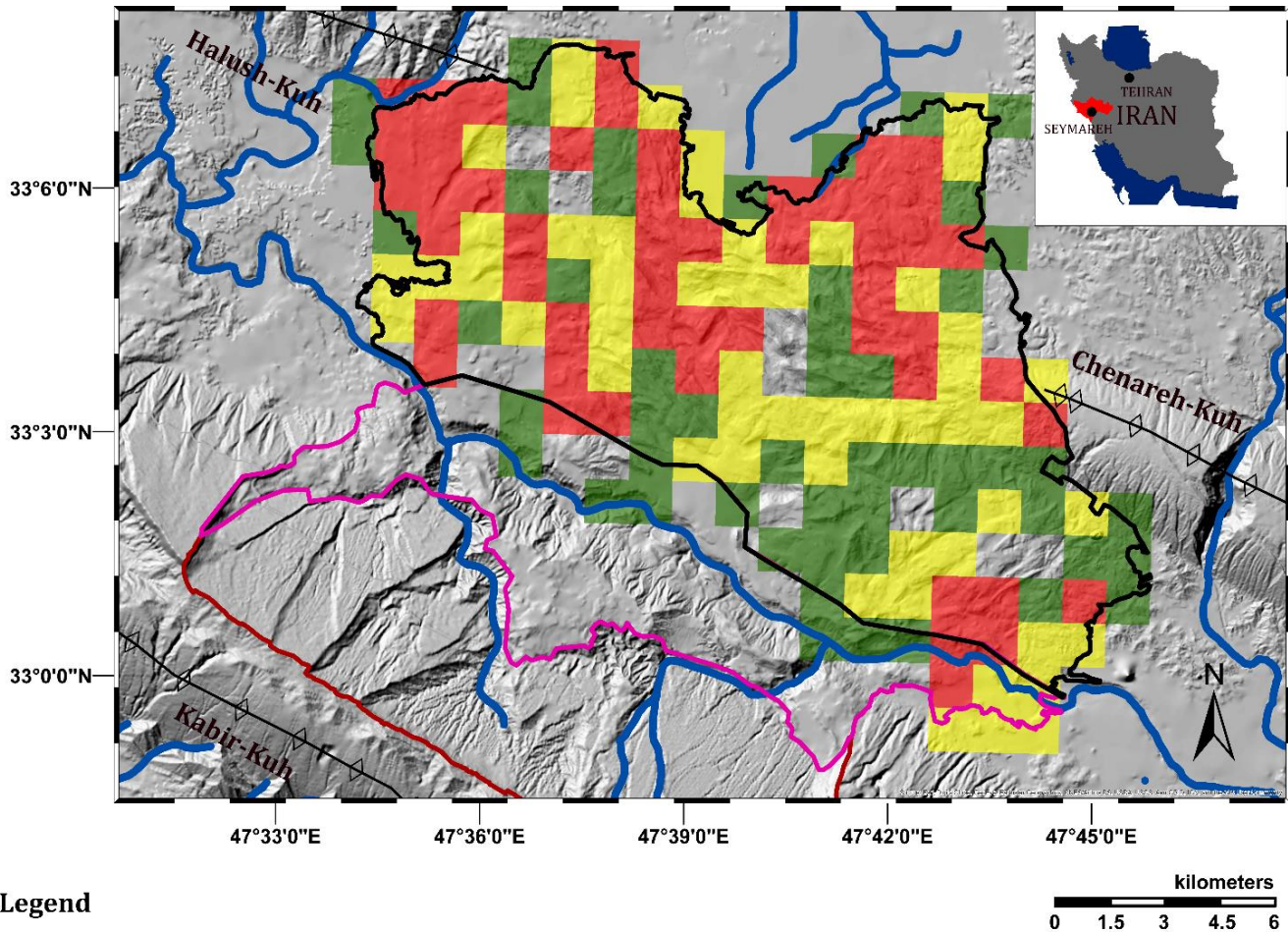
Legend

- | | | |
|------------------------------------------------------------------------------------------------------------------------------------------------------------------------------------------------------------------------------------------------------------------------------------------------------------------------------------------------------------------------------------------------------------------------------------------------------------------------------------------------------------------------------------------------------------------------------------------------------------------------------------------------------------------------------------------------------------------------------------------------------------------------------------------------------------------------------------------------------------------|----------------------------------------------------------------------------------------------------------------------------------------------------------------------------------------------------------------------------------------------------------------------------------------------------------------------------------------------------------------------------------------------------------------------------------------------------------------------------------------------------------------------------------------------------------------------------------------------------------------|-------------------------------------------------------------------------------------------------------------------------------------------------------------------------------------------------|
| <ul style="list-style-type: none"> Area of landslide debris with Asmari Formation Area of landslide debris with Pabdeh-Gurpi Formation Scar Area Border Fold Axis Main Streams | <p>Group Number of Gully Density</p> <ul style="list-style-type: none"> 1 2 3 4 | <p>Gully Density For Each Group</p> <ul style="list-style-type: none"> 1) 0 2) 0- 15,102.99 3) 15,102.991- 71,199.85 4) 71,199.851- 550,180.68 |
|------------------------------------------------------------------------------------------------------------------------------------------------------------------------------------------------------------------------------------------------------------------------------------------------------------------------------------------------------------------------------------------------------------------------------------------------------------------------------------------------------------------------------------------------------------------------------------------------------------------------------------------------------------------------------------------------------------------------------------------------------------------------------------------------------------------------------------------------------------------|----------------------------------------------------------------------------------------------------------------------------------------------------------------------------------------------------------------------------------------------------------------------------------------------------------------------------------------------------------------------------------------------------------------------------------------------------------------------------------------------------------------------------------------------------------------------------------------------------------------|-------------------------------------------------------------------------------------------------------------------------------------------------------------------------------------------------|

Figure 40 Gullies density zonation

deduced that in these areas the erosion rate was lower respect to other zones, allowing to better preserve the original landforms.

The measurement of blocks was performed via remote surveying, i.e. through high resolution satellite images, and verified during field survey as well as some other blocks were recognized and measured by meters during field survey. A total of 1295 blocks larger than 10 meters were recognized and measured. The density of blocks in each 0.01km^2 using point density subset of spatial analyst tools in GIS were calculated and then density values in each square kilometer were summed and divided in four classes (Table 8). It can be seen in Figure 41 that the blocks have higher density in the perimeter and middle area of the debris. The distribution of huge blocks density is in good agreement with the ridge density and can represent the original regions of the debris where both (ridges and blocks) are present. The block density distribution also reveals what has been deduced by ridges density i.e. that portions of Chenareh-Kuh and Halush-Kuh are buried under the landslide debris and their presence caused back motion of blocks during the emplacement of the Seymareh landslide debris emplacement.



Legend

- Area of landslide debris with Asmari Formation
 - Area of landslide debris with Pabdeh-Gurpi Formation
 - Scar Area Border
 - Fold Axis
 - Main Streams
- | Group Number of Block Density | Block Density For Each Group |
|-------------------------------|------------------------------|
| 1 | 1) 0 |
| 2 | 2) 0- 309.79 |
| 3 | 3) 309.791- 910.01 |
| 4 | 4) 910.011- 4,937.33 |

Figure 41 Blocks density zonation

By connecting the Halush-Kuh ridge axis to the Chenareh-Kuh one and considering the watersheds (Figure 42), it can be observed that there are separate watersheds in two side of hypothetical line which can confirm that parts of Halush and Chenareh anticlines are buried under the Seymareh landslide debris. Most of longest flow path of the watershed in the south part of the debris terminate to the current Seymareh River gorge thus justifying the higher power of water which caused the surface debris to be eroded until reaching the bedrock and the primary landforms to be changed into secondary ones.

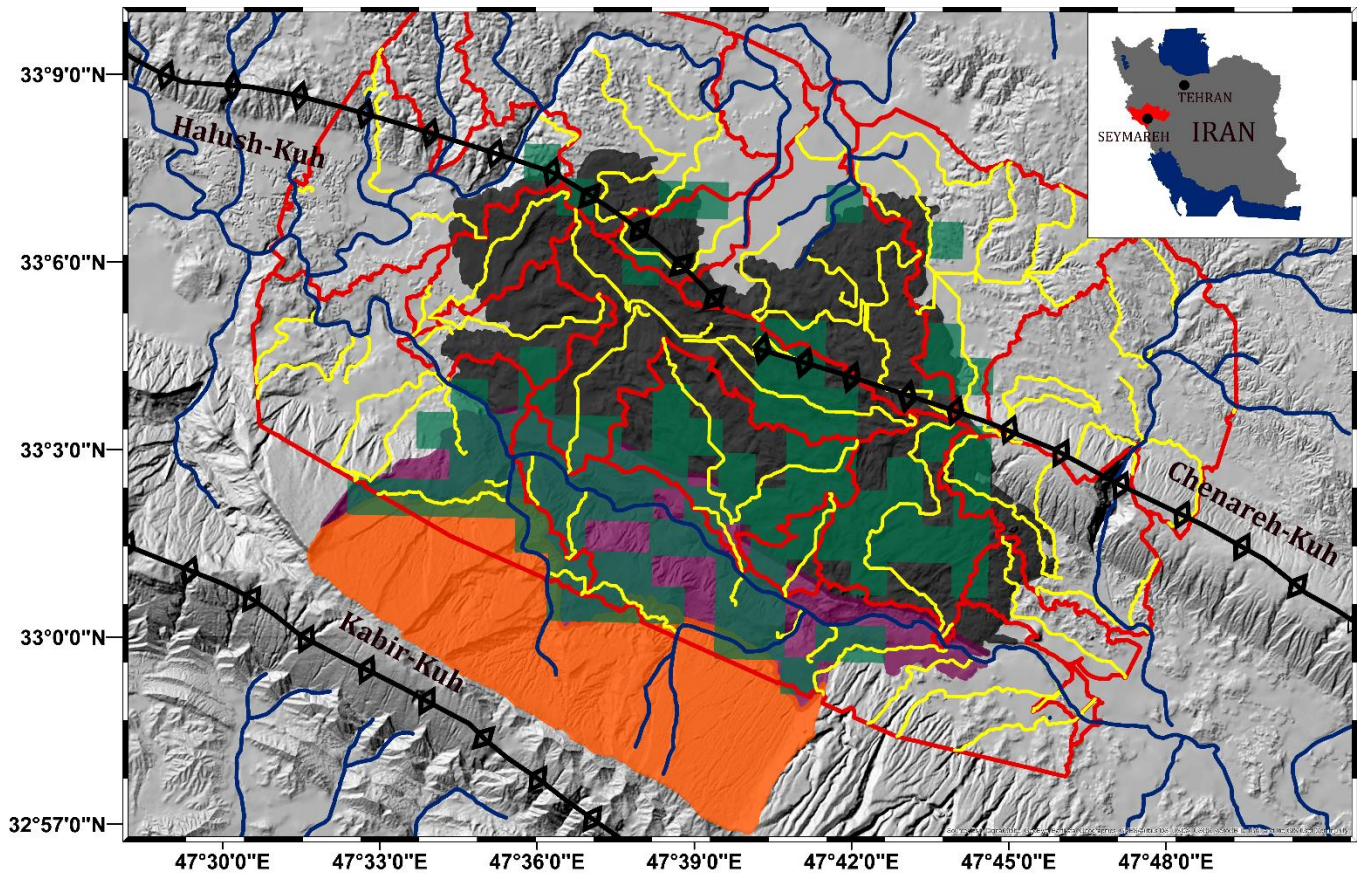


Figure 42 Watershed and longest flow paths

Chapter 4- Soil properties of the landslide debris

4.1 Introduction

It is known that the geotechnical characterization of landslide dams is closely related to the grain size distribution of the composing materials. Grain size analysis provides important clues to the sediment provenance, transport history and depositional conditions (Blott and Pye 2001). It also exerts a control on dam stability, influencing the strength and the permeability of the dam material (Casagli et al. 2003). The deposit resulting from a rock avalanche is sedimentologically distinctive and can thus form an important basis for classification (Dunning et al 2005). To date, several common sedimentological features of rock avalanche, rockslide, and volcanic debris avalanche deposits are recognized and provide insights into their emplacement processes (Ruiz-Carulla et al. 2015, Dufresne et al. 2016).

For several decades, classic sedimentation methods (hydrometer and pipette) combined with sieve method have been adopted as the international standard to determine quantitatively grain size distribution of soils (Cooper et al. 1984, Wen et al. 2002). With recent technological developments, new methods are introduced for determination of grain size distribution of soils, including laser diffraction, electrical sensing, X-ray sedimentation (attenuation), and image analysis (Singer et al. 1988, McCave and Syvitski 1991, Detert and Weitbrecht 2012, Mustafa and Orhan 2015).

In this research 2 sampling techniques and 3 analyzing methods were applied to determine the grain size distribution of Seymareh landslide debris. Because of the possibility that the original distribution of grain sizes and therefore the permeability have changed due to local geomorphological processes after the landslide, it was decided to sample for both techniques according to the zonation based on tone, texture and structure of aerial photos.

The first technique was the photographic one where vertical windows of the outcrop area were cleared with hand, then vertical exposures were made as flat as possible and finally orthogonal photographs from each zone³ of the landslide debris were taken. This technique was applied to the particles larger than 9.5mm and up to 1m. The second technique consisted in a sampling and laboratory testing; at this aim, the area of each sampling point was cleaned to a depth of 5cm and a total number of 63 matrix samples related to the landslide debris in the order of 1kg

³ Zonation based on tone, texture and structure of aerial photos

in weight and up to 9.5mm in size were taken to be analyzed by laboratory sieve method combined with sedigraphy with an x-ray sedigraph. For the second technique, it was decided to take at least 3 samples from each zone of the landslide debris in order to evaluate the efficiency of the zonation by aerial photos.

4.2 Grain size analysis

4.2.1 Photographic technique

The photographic technique was carried out using BASEGRAIN software. After starting BASEGRAIN the user must upload an image. Once image uploading is finished, the full image to be analyzed appears on the working surface of the main menu. Figure 43 shows a typical screenshot at this state of analysis. Preprocessing involves scaling and image cropping. The user can downsize the image to decrease the time needed for automatic object detection. If the image scale in [mm/px] is known, the user can type in the value in the related text field. Otherwise, the image scale can be introduced to the software by a known distance points on the photo, e.g. a marker or a leveling rod. The known distance in [mm] must be typed in the request field. Then, the baseline of the working menu shows the scaling factor in [mm/px].

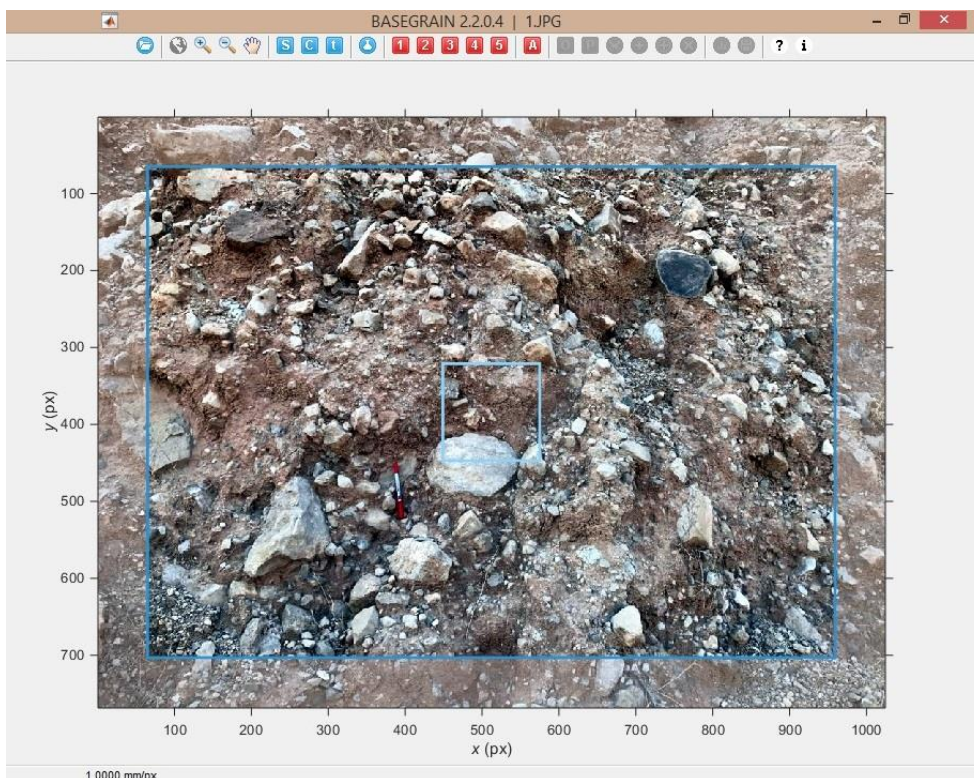


Figure 43 The full image to be analyzed on the working surface of the BASEGRAIN software

Next, the BASEGRAIN software recognize the grain size based on 5 detection steps as following:

In a first step, the software detects interstices using a double grayscale threshold approach. The first grey-thresh level initially determines definite interstices. The second grey-thresh level gives an estimation to possible interstices. The resulting possible interstices are confirmed if they are connected to the definite interstices as found by the first grey-thresh level.

In a second step, for detecting further possible interstices, the software performs a morphological bottom-hat filtering on the grayscale image. Possible interstice areas in the bottom-hat filtered image typically are confirmed if they are connected by $\geq 5\%$ to the definite interstices from first step.

Then, the software applies two gradient filter techniques, the Sobel method (MATLAB, 2012) and Canny method (1986) to detect strong and weak edges, respectively. If $\geq 25\%$ of Canny edges area are congruent to previously confirmed interstices, the software confirms these edges. Using the same way and based on the same criteria, Sobel edges confirms further Canny edges. At the end of this step using morphological operations, the software clears the confirmed interstices.

Once the detection of interstice areas was completed, the software focuses on the separation of single grain areas by applying a watershed algorithm twice. First, by identifying watershed bridges from the inverted binary outcome matrix and dilation by a disk-shaped element of radius 4 px. The software confirms areas of Canny edges by these watershed bridges if they get completely masked and if their interrelated orientation angle differs by $< 10^\circ$. Second, the software identifies watershed bridges from the actual binary outcome matrix. The software confirms bridges if their area is smaller than a threshold of typically 40 px to suppress over-segmentation.

Last step relates to final operations with the goal of detecting the region properties of each grains top-view area. Ellipses are fitted to object areas using normalized second central moments of determined object areas. Their minor axes, i.e. the b -axes, are taken as proxies of characteristic grain diameters. Boundary grains that are not fully included within the analyzed frame are blanked out to avoid a misleading statistical analysis of the characteristic diameters. Once the object detection process is finished, the result is visualized on the working surface. Figure 44 shows a typical screenshot at this state.

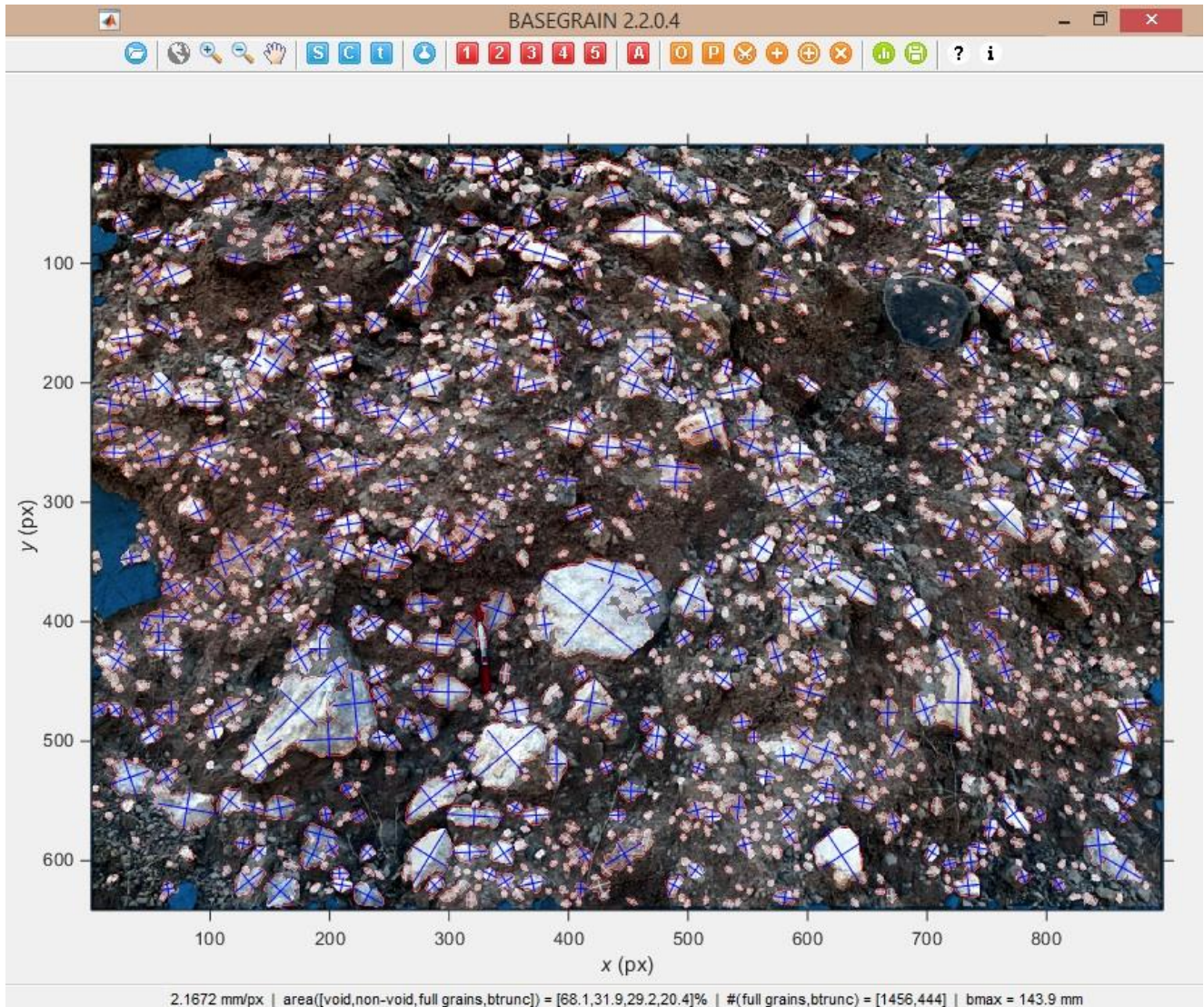


Figure 44 Final result of automatic object detection procedure. Straight lines (color print: blue) represent a-axis and b-axis of ellipses fitted to each object using normalized second central moments of determined object areas. Pixels of grain boundaries are highlighted (color print: red). Grains with contact to enclosing frame are blanked out. First estimation of fractional weighted mean diameter d_m is given at baseline information bar.

With finishing the automatic object detection process, the grains recognized by the software were observed. As it can be seen in Figure 44, there are some errors in the recognition of the object that should be modified. In this step, the unique objects that have been recognized as more than one object during automatic object detection were corrected by the post processing process. Figure 45 illustrates an example on how the post-processing affects the result of the detected object areas.

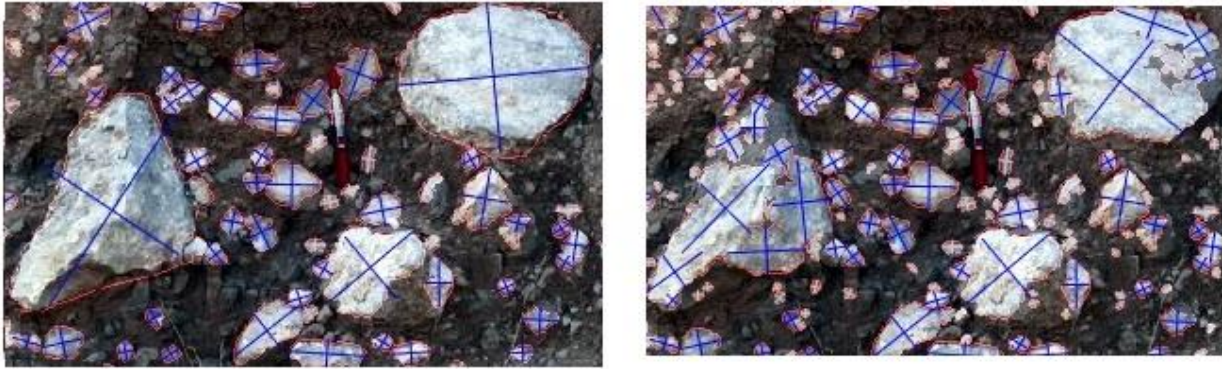


Figure 45 Effect of interactive post-processing on pre-precision of object detection procedure. Left: after post-processing, right: before post processing.

Once the post processing process were finished, the results were saved as EXCEL spreadsheets file. The exported data contents are grain-size curves, grain size statistics, all known properties on each detected grain, and further data including the total void area and the total non-void (grain) area.

4.2.2 Classification based on USCS standard (D2487-17)

The second and third analyzing methods (Sieve test and x-ray sedigraph) were applied to the samples collected by the second sampling technique explained before. Sieve test (D422-63) was used to quantitatively determine the particle size distribution of the landslide debris matrix in size range between $75\mu\text{m}$ (held up by the sieve No.200) and 9.5mm (held up by the sieve No.3/8) while the distribution of particles smaller than $75\mu\text{m}$ was carried out through sedigraphy with an x-ray sedigraph.

At the end of these tests, the results of sieving and sedigraphy with x-ray sedigraph were coupled by the laboratory modulus directly from the computer. This made it possible to reconstruct the granulometry curves of the landslide debris matrixes for particles up to 9.5mm .

After reconstruction all the granulometry curves belongs to all samples, to classify the soil samples of the landslide debris matrix based on the USCS classification system (D2487-17), the Atterberg limits (D4318-17e1) needed to be determined. The Atterberg limits are index properties that express the limit value of water contents (W) corresponding to the transition phase between a physical state assumed by the ground to the next. For the purposes of this study, the liquid limit (LL) and the plastic limit (PL) were measured.

Through the analysis of the limits, carried out previously, it was possible to go back to the determination of the plasticity index (PI), which indicates the plasticity of the fine-grained portion of a soil as a function of its water content. It been defined as: $PI = LL - PL$.

Based on the results of laboratory tests and utilizing the unified soil classification chart and the plasticity chart, the matrix samples of the landslide debris were classified by USCS classification system.

4.2.3 Statistical classification

In the next step, the results of granulometry by x-ray sedigraph and sieving were correctly coupled with the results obtained by the application of the photographic technique for boulders up to 80cm. These combinations terminate to the reconstruction of complete granulometric curves of Seymareh landslide debris at different locations on its surface for particles in size range from 1 μ to 80cm. In order to statistically classify the complete granulometric curves of the landslide debris belongs to the Asmari Formation area, the values of D10 and D60 for all samples in this area were measured and the graph of D10-D60 was drawn (Figure 46).

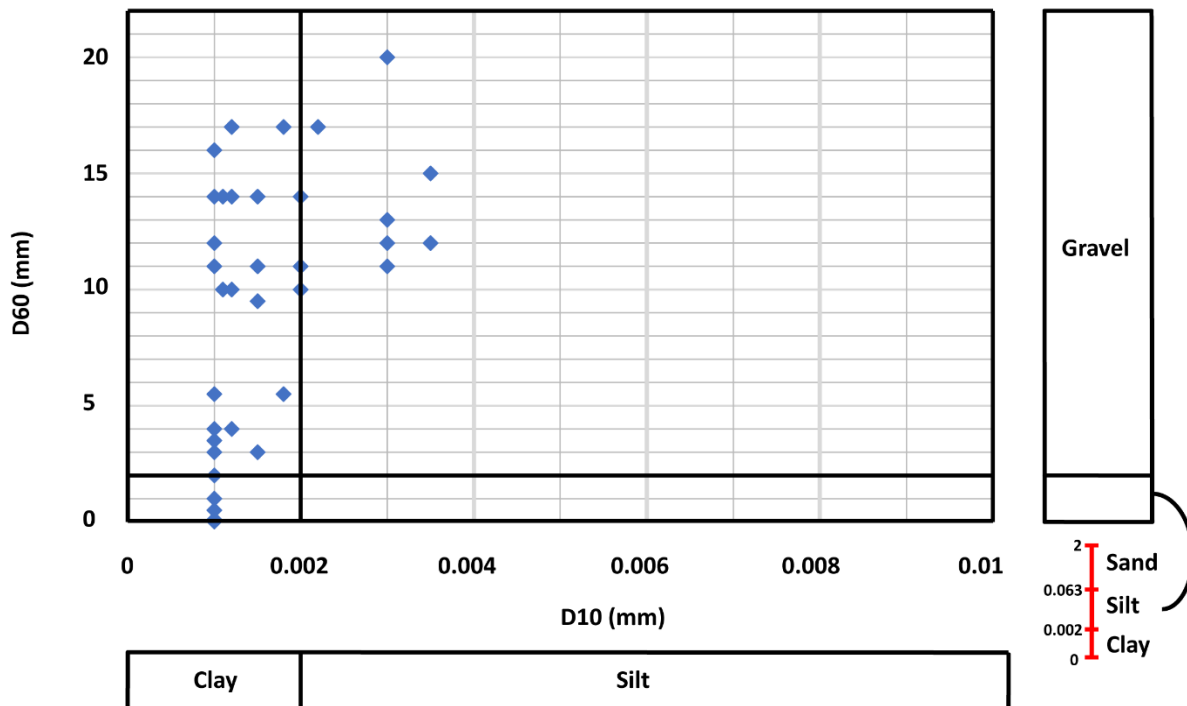


Figure 46 Graph of D10-D60 of soil samples in the Asmari Formation debris

Then based on the combinations defined in the Table 15, the samples were classified into 3 classes and the average value and standard deviation of D10 and D60 values for each class been calculated and graphed (Figure 47).

Table 15 Range of D10 and D60 for each class

Class Number	Range of D10 values (mm)	Range of D60 values (mm)
1	0-0.0025	0-7
2	0-0.0025	7.1-20
3	0.0026-0.0045	7.1-20

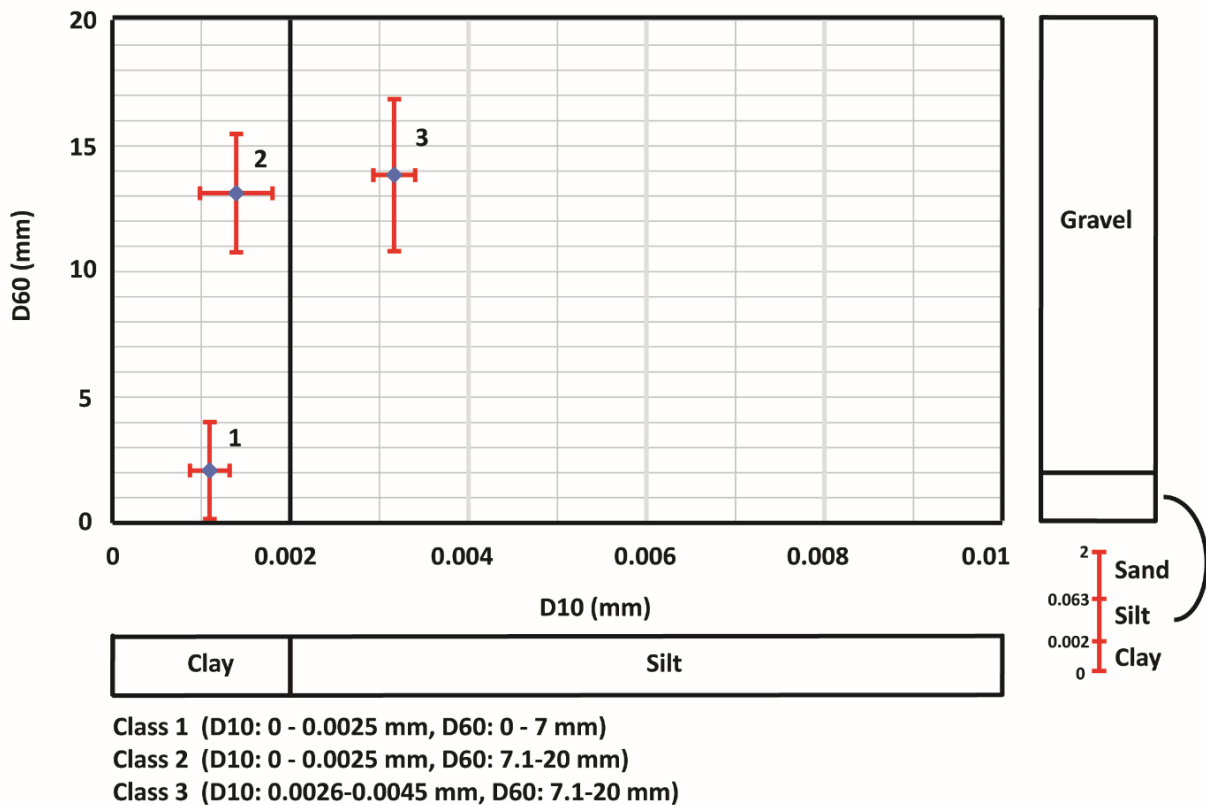


Figure 47 Graph of average value of each class based on D10 and D60 with their standard deviation in the Asmari Formation debris

In order to test the degree of accuracy of defined granulometric classes, the values of D50 and Cu for all samples were then calculated and graphed (Figure 48) and based on the classes of D10-D60, the average values and standard deviation of D50 and Cu for each class were calculated and graphed (Figure 49).

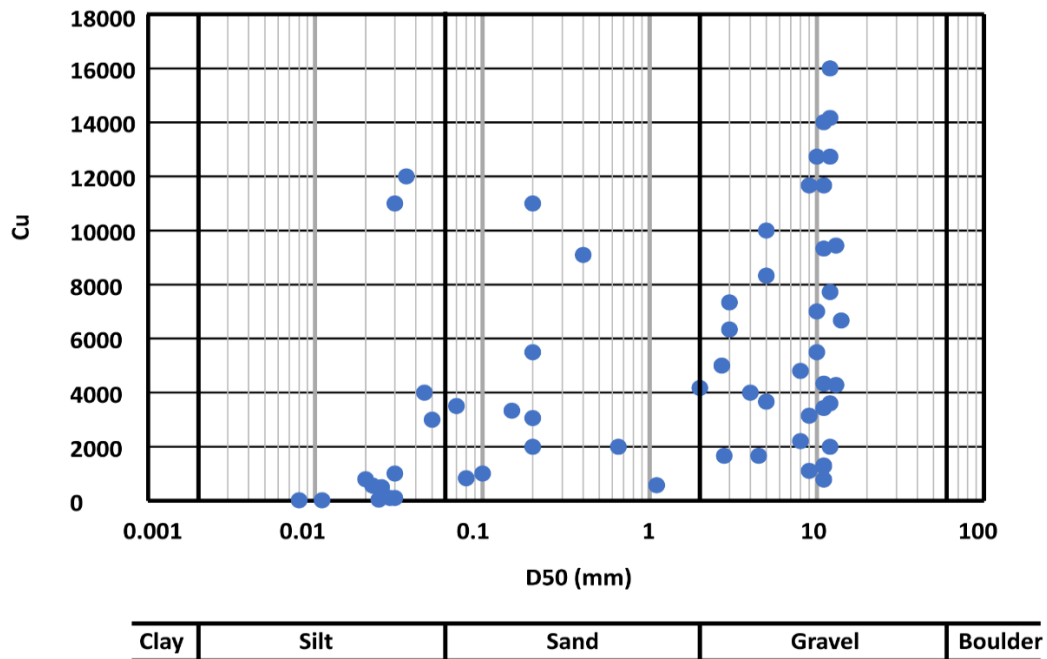
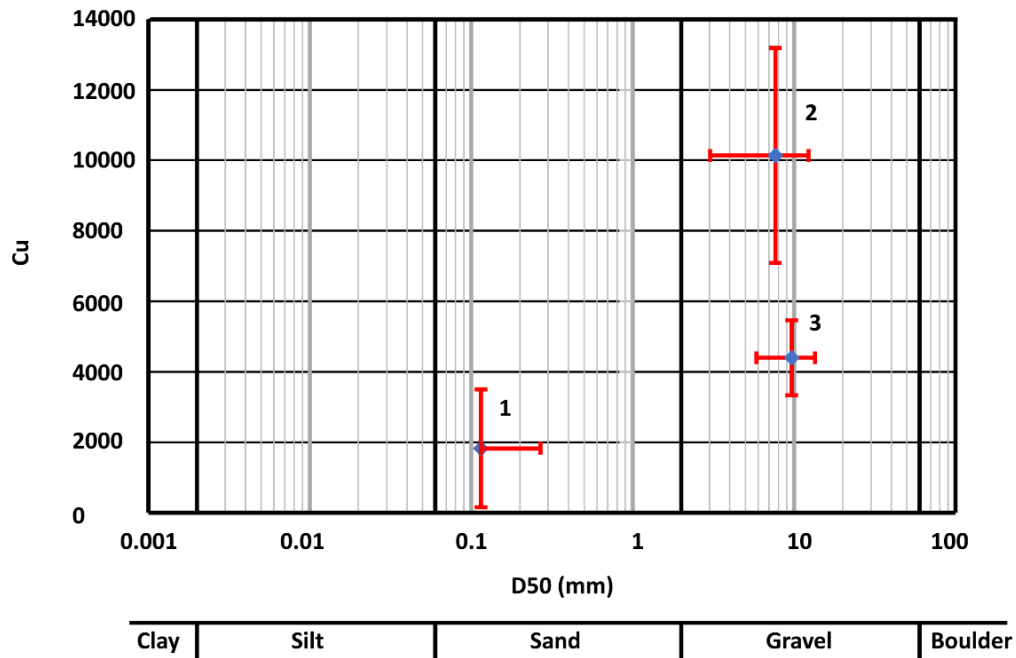


Figure 48 Graph of D50-Cu of all samples in the Asmari Formation debris



Class 1 (D10: 0 - 0.0025 mm, D60: 0 - 7 mm)
 Class 2 (D10: 0 - 0.0025 mm, D60: 7.1-20 mm)
 Class 3 (D10: 0.0026-0.0045 mm, D60: 7.1-20 mm)

Figure 49 Graph of average value of each class based on D50 and Cu with their standard deviation in the Asmari Formation debris

4.3 In-situ density (D2167-15) and permeability tests (D2434-68)

The Seymareh landslide debris shows a chaotic texture (Figure 50) characterized by a mixture of angular clasts of different sizes (up to 10s meters) and fine matrix resulting from the dynamic fragmentation and comminution of the material. As it can be seen in Figure 50, the landslide debris is matrix-supported. The coarse particles forming the debris are scattered inside a prevailing fine matrix and they are not in contact with each other. Therefore, the permeability of the debris is mainly depending on the finer material.



Figure 50 Texture of the Seymareh landslide debris

To carry out the permeability test in the laboratory, it was necessary to measure the in-situ density of the landslide debris in order to obtain a reconstituted laboratory sample. Therefore, the rubber balloon method with some changes for measuring the in-situ density was used. For performing the test (D2167-15), after cleaning and leveling the test location, a base plate was located on the test surface and a hole was excavated inside the base plate. Using the rubber balloon instrument, the volume of the hole was measured. The removed soil from the hole in the laboratory was placed in the oven at a temperature of 110 °C for about 12 hours. Then, the grains larger than 2mm were separated by standard sieve N.10 and their volume and weight were measured using graduated cylinder containing water and a balance. The particles passed from sieve N.10 (2mm) were weighed and their ρ_d was calculated. This test was done for 28 location on the landslide debris surface and represented an average density value of 12kN/m³ for the finer part of the landslide debris.

Once the in-situ density of the landslide debris at different location on its surface was measured, samples with the same group name based on USCS classification system were collected and tested together. There was only one exception, as most of the landslide debris matrix samples in the Asmari Formation area were from ML group of USCS classification system, in this case, ML samples were divided into three groups. The permeability (k) represents the measure of the speed with which a porous medium is crossed by a fluid. To determine this, various falling head permeability tests were performed using a variable load permeameter, with the laminar flow directed from bottom to top. The falling head permeability test is a common laboratory testing method used to determine the permeability of fine grained soils with intermediate and low permeability such as silts and clays. Therefore, it was decided to do the permeability tests on granular finer than sieve N.40 (0.425mm). It was also necessary to reconstitute the samples according to different densities corresponding to different depths. Therefore, for estimating density variation respect to depth, in a first step, the variation of the stress respect to density was estimated. In the laboratory, the maximum reachable density by 600kN.m/m² stress of standard proctor test was 17kN/m³. It was hypothesized that the density at surface is equal to zero stress and a quite linear relation between effective stress and density were defined (Figure 51).

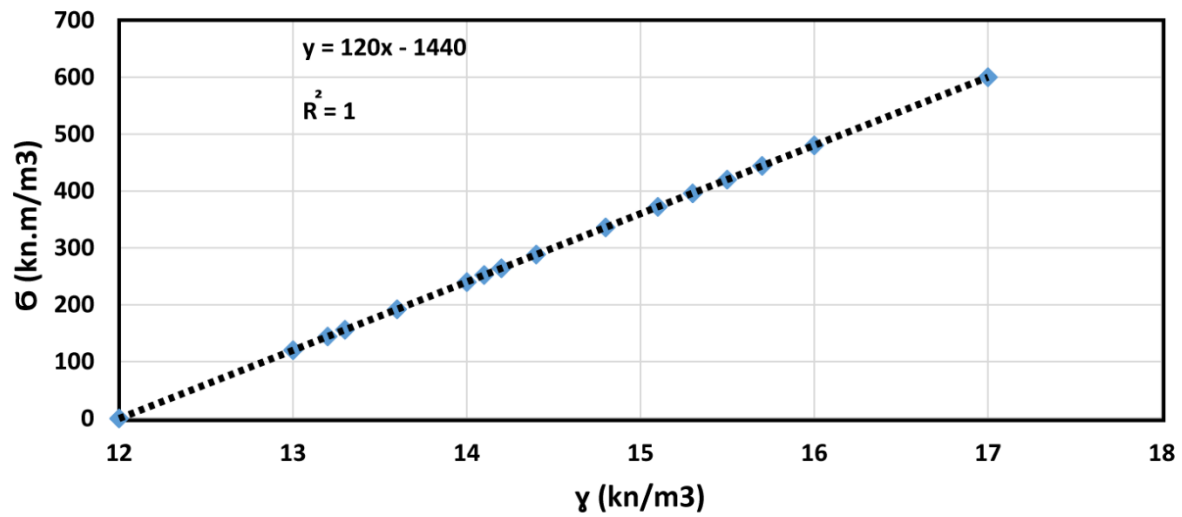


Figure 51 Graph of effective stress vs. density as derived by laboratory tests on the fine-grained portion of the samples

In a second step, a series of permeability tests were performed inside a 4-inch cylinder by density values between 12 and 17kN/m³ and 10% moisture and for each group of the matrix samples, the permeability values correspond to different density were measured (Figure 52).

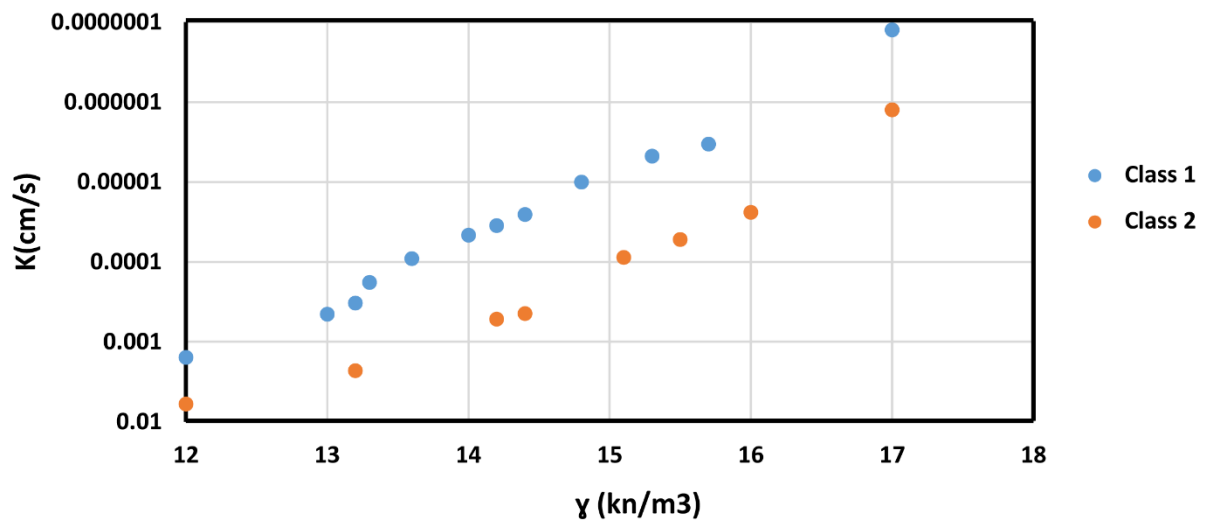


Figure 52 Graph of permeability vs. density as derived from the performed laboratory tests

By merging the experimental distributions in Figure 51 and Figure 52, the graph of permeability vs. effective stress was derived (Figure 54). Then, using the following formula: $\sigma = \gamma H$, the relation between the density, stress and depth were defined (Figure 53).

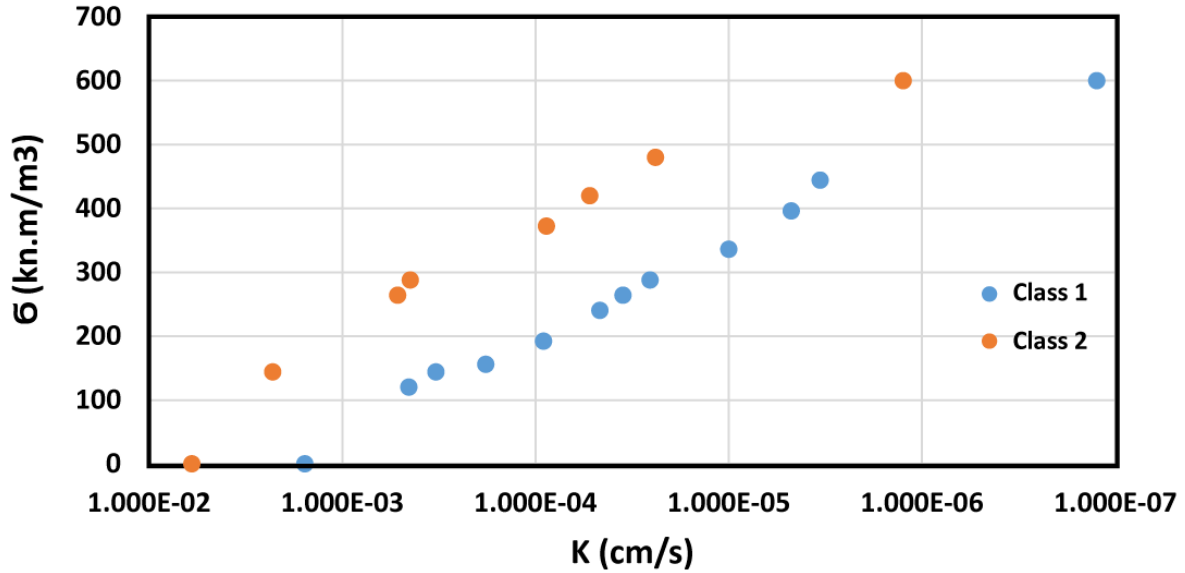


Figure 54 Graph of stress vs. permeability

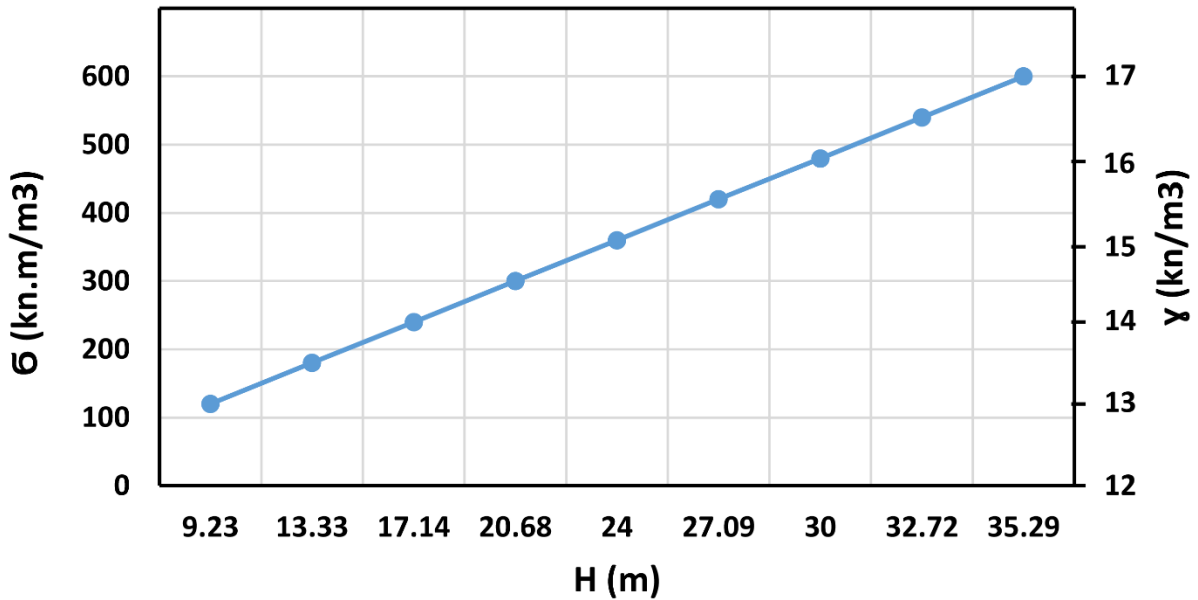


Figure 53 Graph of stress-density-depth

In a final step, the graph where K is related to H by merging Figure 54 and Figure 53 was extracted (Figure 55).

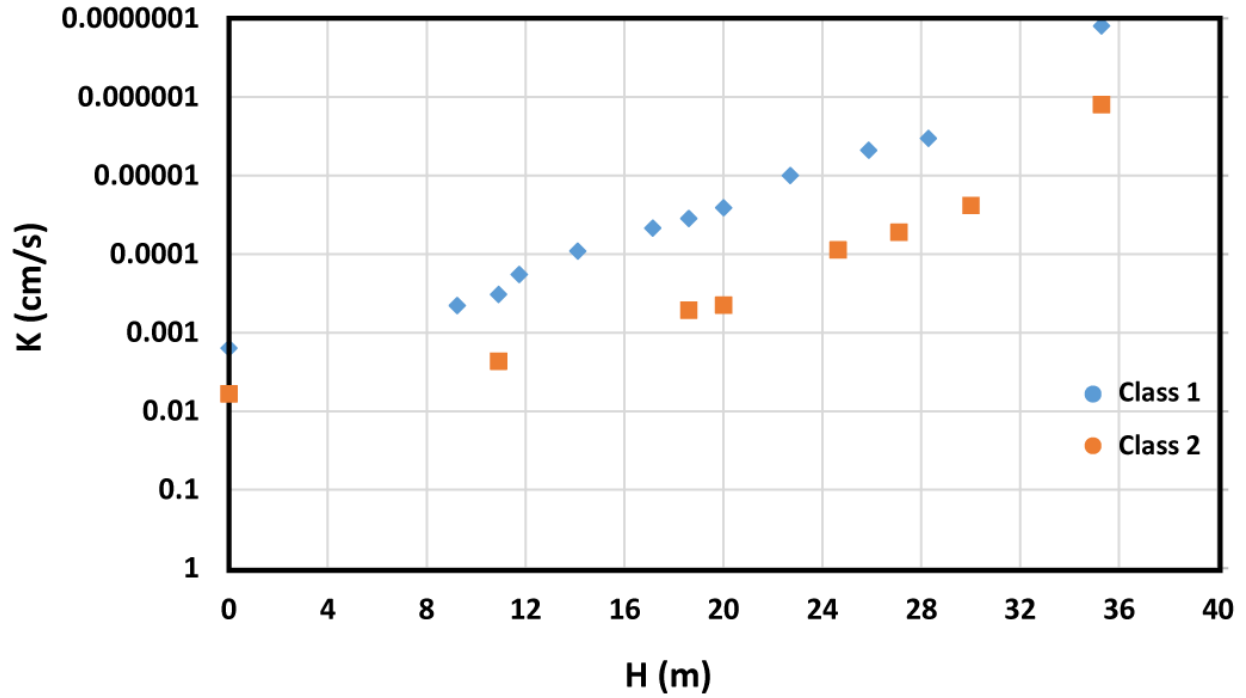


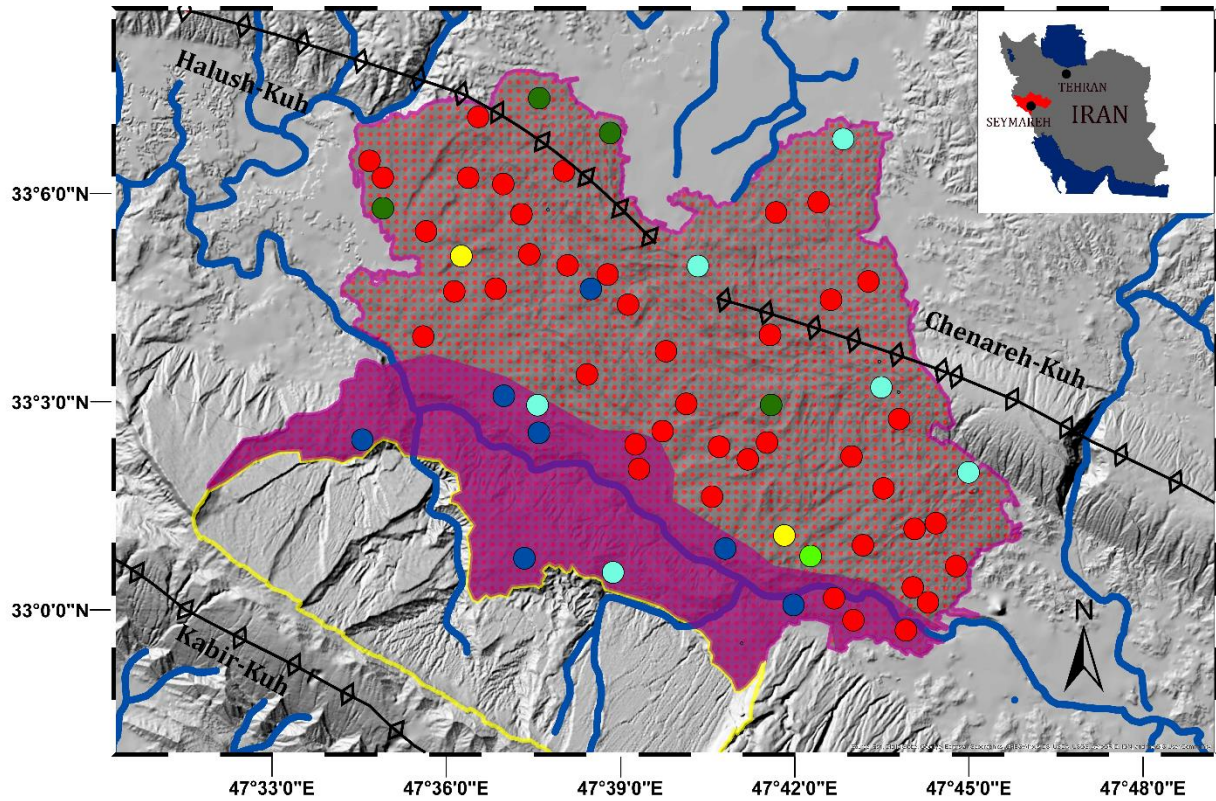
Figure 55 Graph of density vs. depth

4.4 Results

4.4.1 USCS classification

USCS classification system was used to classify the landslide debris matrix. The results of USCS classification are shown in Figure 56. Based on the obtained results, 6 groups of matrix types can be distinguished: high and low compressibility silt (MH and ML), clay of low plasticity (CL), sandy silty clay (CL-ML), clayey sand (SC), silty sand (SM). Fine-grained soils (ML, MH, CL, CL-ML) has the highest amount and mostly are located in the Asmari Formation debris area in the middle and distal portions of the landslide debris while the coarse-grained (SC and SM) soils are mainly distributed within the debris in the proximity of the detachment area of the Seymareh landslide which are the Pabdeh-Gurpi Formation debris area. This could be explained by the original stratigraphic setting of the geological units in the scar area of the landslide. At failure the physic of the rock avalanche emplacement justifies that the Carapace (composed by the Asmari) moved up to and faster than the Pabdeh-Gurpi, this is because:

- 1) it was originally overlayers
- 2) it was stiffer (Vassallo, 2017)



Legend

- Landslide Debris (Asmari Formation) Roberts & Evans 2013
- Landslide Debris (Pabde-Gurpi Formation) Roberts & Evans 2013
- Scar Area Border
- Fold Axis
- Main Streams

Classification of the landslide debris matrix based on USCS ((ASTM, 2000)

- ML
- MH
- SC
- SM
- CL
- CL-ML



Figure 56 USCS classification of all samples

4.4.2 Statistical classification

Combination of data from sieve, X-ray and photographic methods produced grain size distribution curves of Seymareh landslide debris for particle in size range from 1 μ to 50 cm in the Asmari Formation area (Figure 57). The grain size distribution curves of the samples (Figure 57) show very gentle slope in the sand range. Almost all curves are characterized by a typical trend that provides two increasing cumulative trends for size lower than 0.06 mm and higher than 10 mm with an almost constant cumulated value between them. This allows to assume a negligible contribution to the grain particles in a size range between 0.06 mm and 10 mm. Such a trend cannot be recognized in the grain-size curves for samples tested from the Pabdeh-Gurpi Formation deposits (Figure 58); in this case, an almost constant rate of the cumulative curve is generally obtained up to 10 mm, followed by a higher rate increase up to about 500 mm.

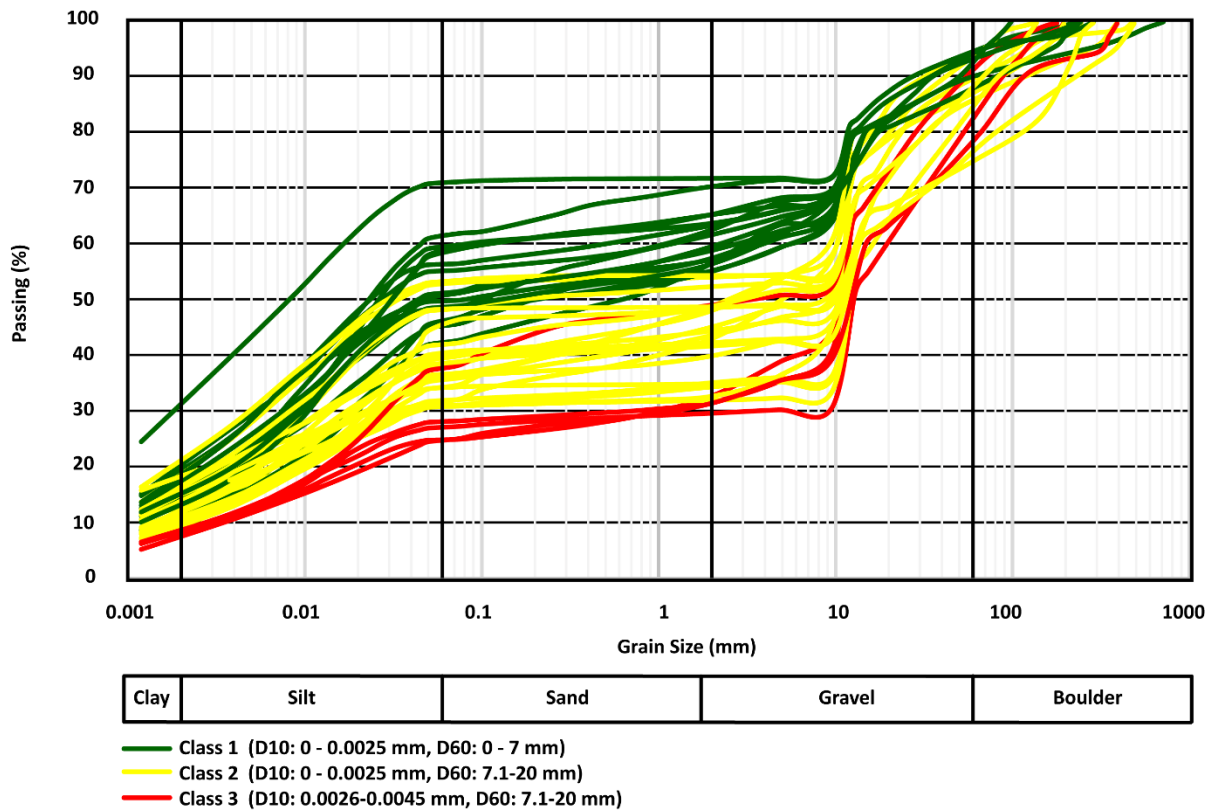


Figure 57 Grain size distribution of samples in the Asmari Formation debris

In order to interpret the distribution trend of the samples taken from the Asmari Formation area, these samples were divided statistically. It means the samples that their D10 and D60 values were focused in an area on the graph of D10-D60 were grouped together. Three groups were recognized, and the results are shown in the Figure 57 based on the value distributions reported in Figure 46 and Figure 47. The samples in the Pabdeh-Gurpi Formation area had close values of D10 and D60. Therefore, it was decided to count all samples in this area as a unique group.

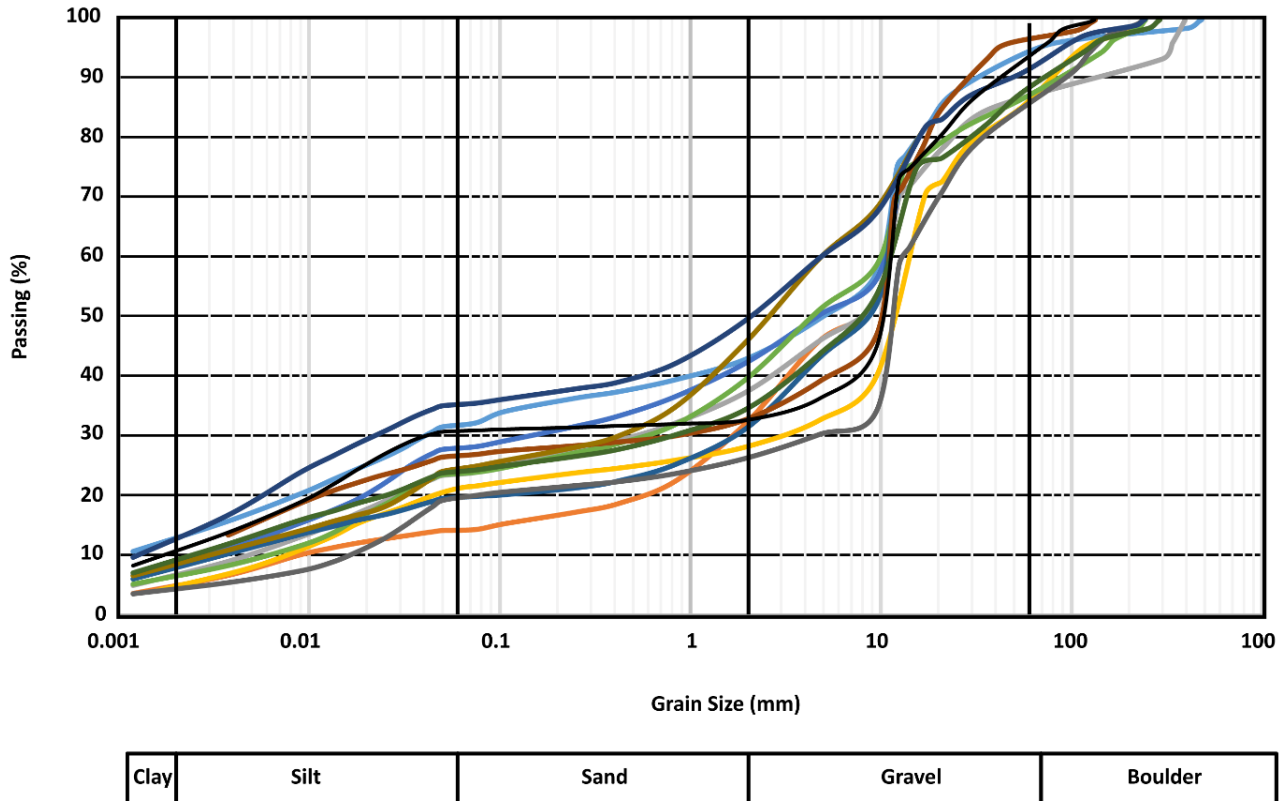


Figure 58 Grain size distribution of samples in the Pabdeh-Gurpi Formation debris

Figure 59 shows the distribution of classified grain size for of Seymareh landslide debris in the Asmari Formation area. As it can be seen, the samples of class 2 which has intermediate particles in size respect to other classes are mainly distributed in the middle of the debris while the samples of finer class (class 1) are distributed in the distal portion in the NW and SE directions; on the other hand, samples with coarser particles (class 3) are almost distributed in different portions of the landslide debris. These results show that there is a change in the grain size distribution along the debris emplacement path. It means that during the event, larger blocks traveled farther and were fragmentated more which results in producing finer particles among huge

blocks in the distal areas. The presence of finer class (class 1) in the SE and NW could be related to the emplacement kinematic of the landslide debris. This, in combination with the performed permeability tests and kinematic indicator will be discussed later.

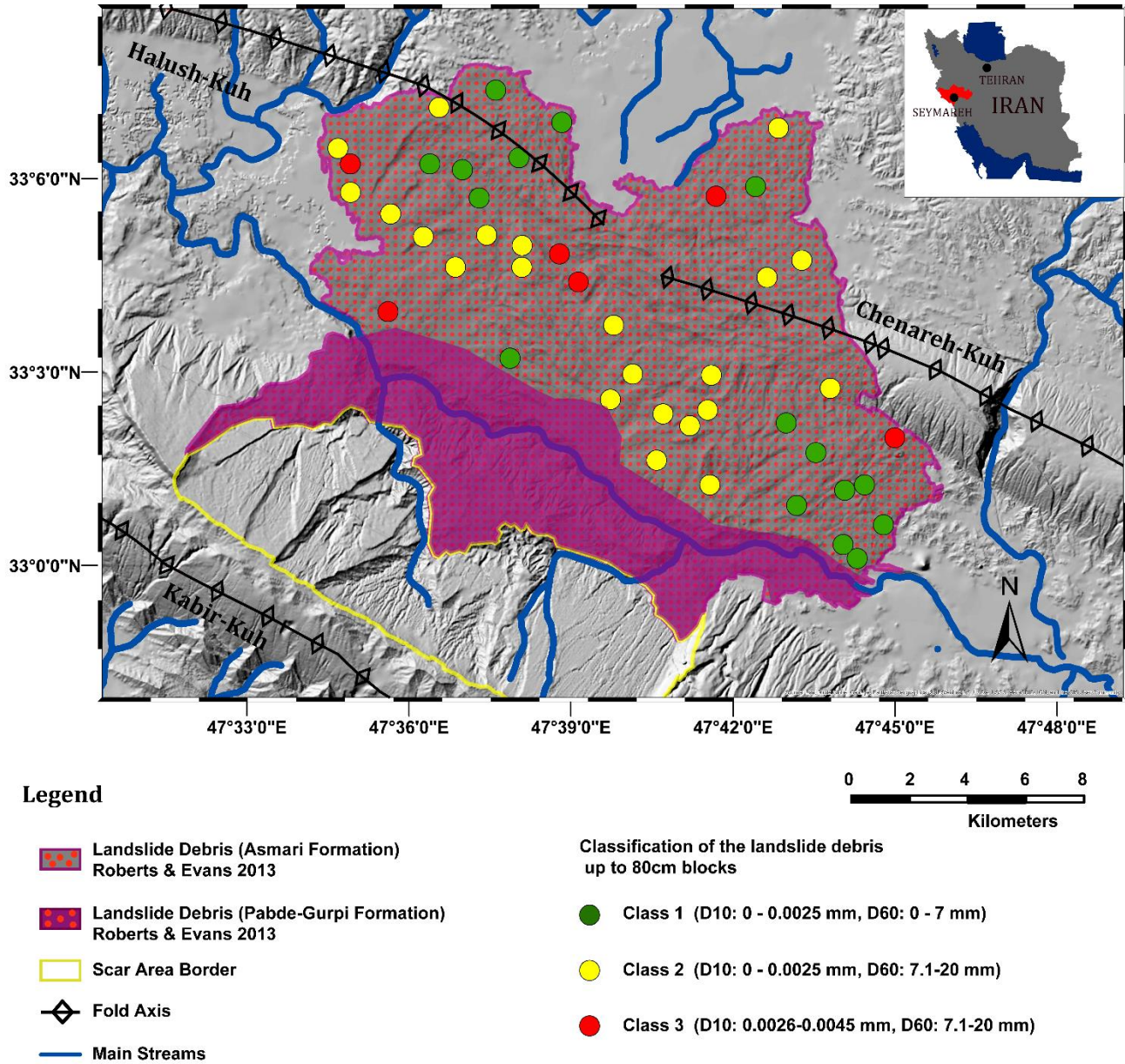


Figure 59 Distribution of grain size classes of the debris matrix in the Asmari Formation area

4.4.3 Permeability tests

The permeability tests carried out on classified soils samples demonstrated that a significant dependency of permeability to density values exists. Since the density change of the debris matrix is not negligible within the effective stress range corresponding to the first 50 m of depth below ground level, it is reliable a variation of permeability within this range of depth. Density value also depends to depth. It means that permeability varied to the depth of the landslide debris. More than 20 permeability tests were performed on the finer grain (passing to the sieve number 40) in the area of the Asmari and Pabdeh-Gurpi Formations debris in order to find a relation between the kinematics of the landslide debris emplacement and the permeability and also to evaluate the possible effect of local geomorphological processes after the landslide event on the original distribution of grain sizes and consequently the permeability. The matrix of the landslide debris in the Pabdeh-Gurpi Formation area are classified as SC and SM based on the USCS classification system. The SC and SM class of USCS are coarse grain. This means the permeability tests which were performed on granular portion finer than sieve number 40 did not consider the coarser grain of samples and therefore they cannot represent the actual permeability values for the matrixes of this area of the landslide debris. The results (Figure 60) show that based on the findings two regions on the landslide debris can be recognized, related to different classes of permeability values. The NE and East regions on the Asmari Formation area of the landslide debris with the permeability in the range of 10^{-2} - 10^{-6} cm/s (class 2) are more permeable respect to the center, NW and West regions with the permeability in the range of 10^{-3} - 10^{-7} cm/s (class 1). The value of permeability for the Pabdeh-Gurpi Formation area in the South part of the landslide debris is similar to the center, NW and West part of the landslide debris in the Asmari Formation area, likely to what resulted for the grain size distribution cases. This can be justified by considering the sandy part of the samples in the Pabdeh-Gurpi Formation area, the whole landslide debris would have three different values of permeability. The order of permeability in different areas on the landslide debris are as follow, from higher to lower permeability. The South area of the landslide debris (Pabdeh-Gurpi Formation area) reveals higher values respect to the NE, East and SE area of the landslide debris (Asmari Formation area) while the center, NW and West area of the landslide debris reveals the lowest values. The explanation for the higher permeability in the NE, East and SE area is related to the kinematics of the landslide debris emplacement. During the emplacement of the debris due to the presence of the Chenareh-Kuh ridge, a part of the debris stopped after

crushing against the hills, a part of debris with higher energy overpassed these two anticlines and the rest of debris swept back in the Seymareh paleo-valley. The samples in the NE, East and SE were taken from the surface and because of sweeping on the debris stopped by crushing the anticlines, these samples represent higher permeability. The NW and West area have lower permeability because they were compressed after crushing the Halush-Kuh. Figure 60 and Figure 61 demonstrate this concept.

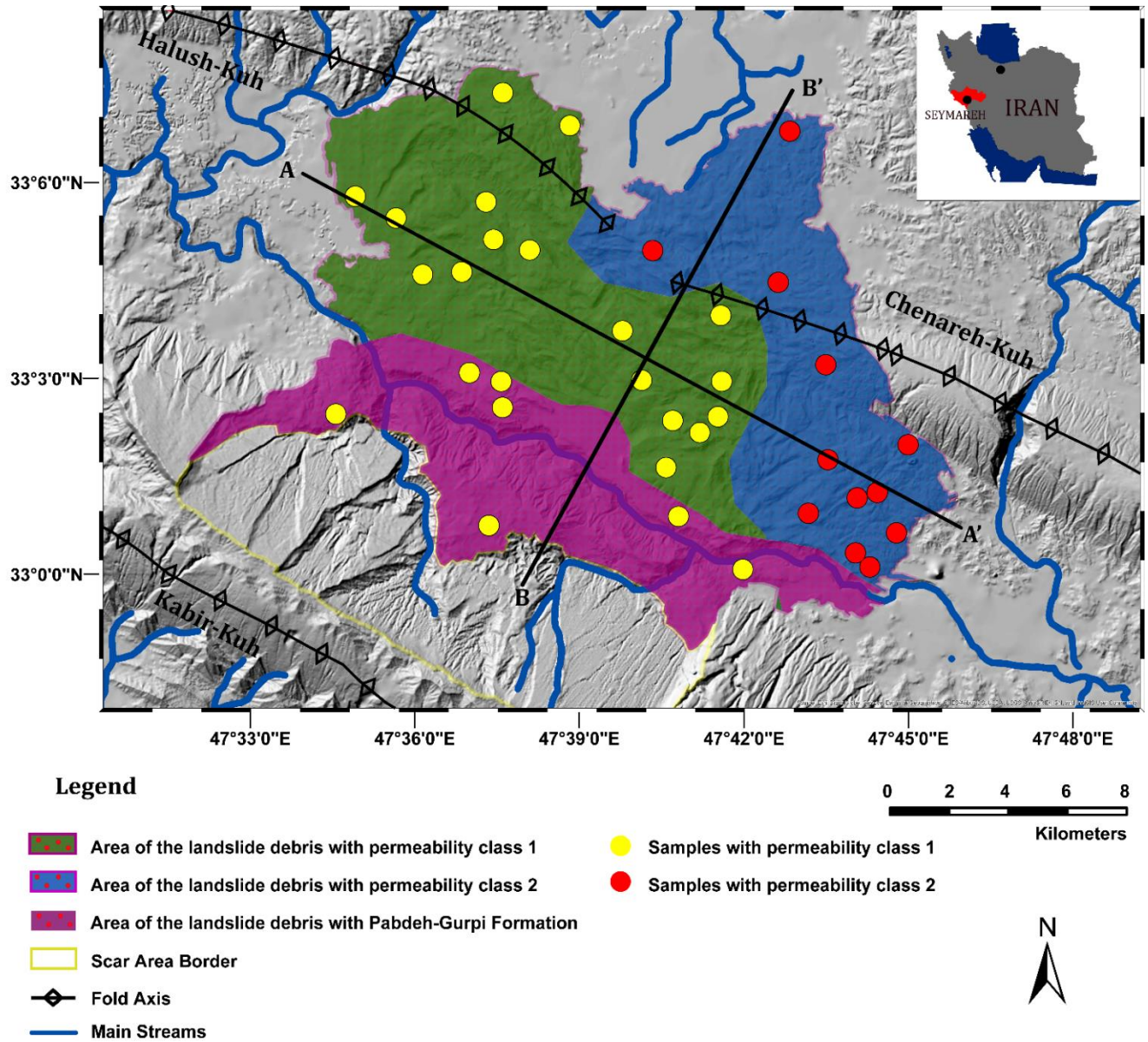
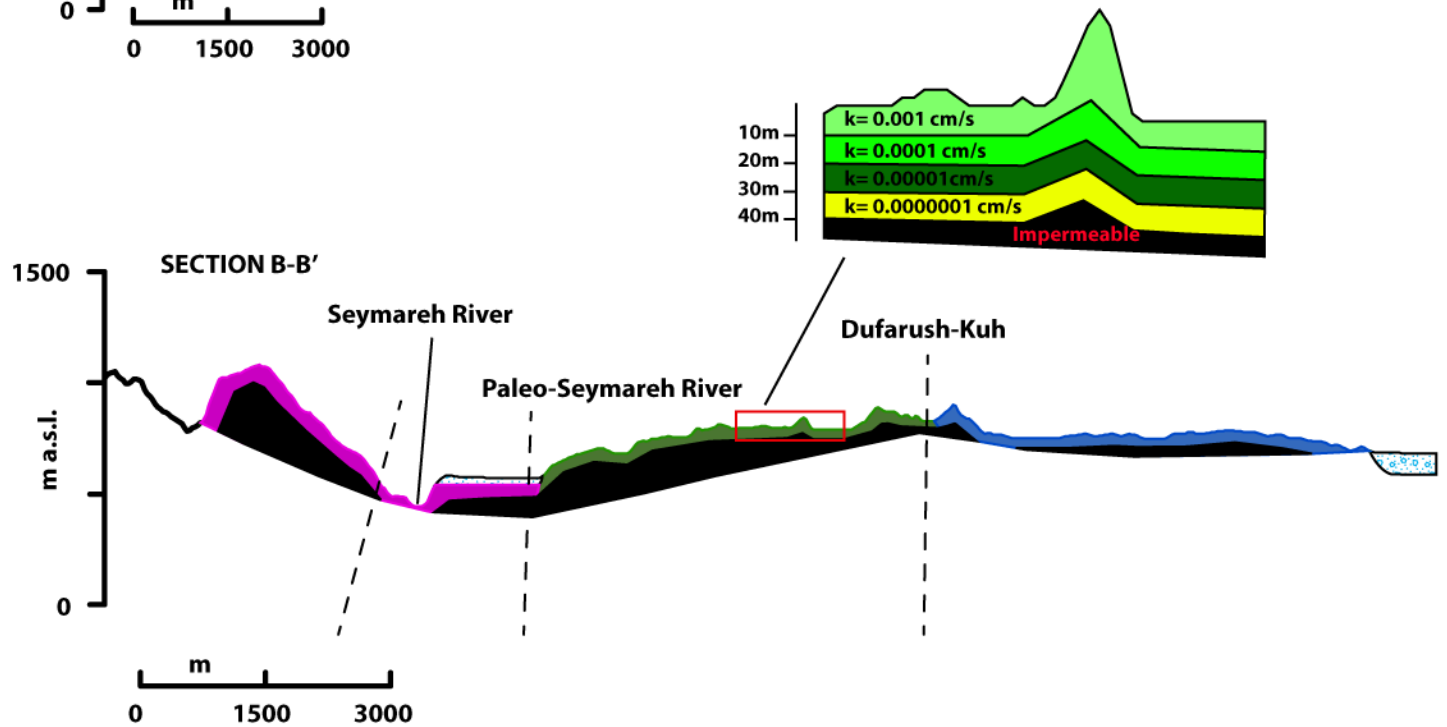
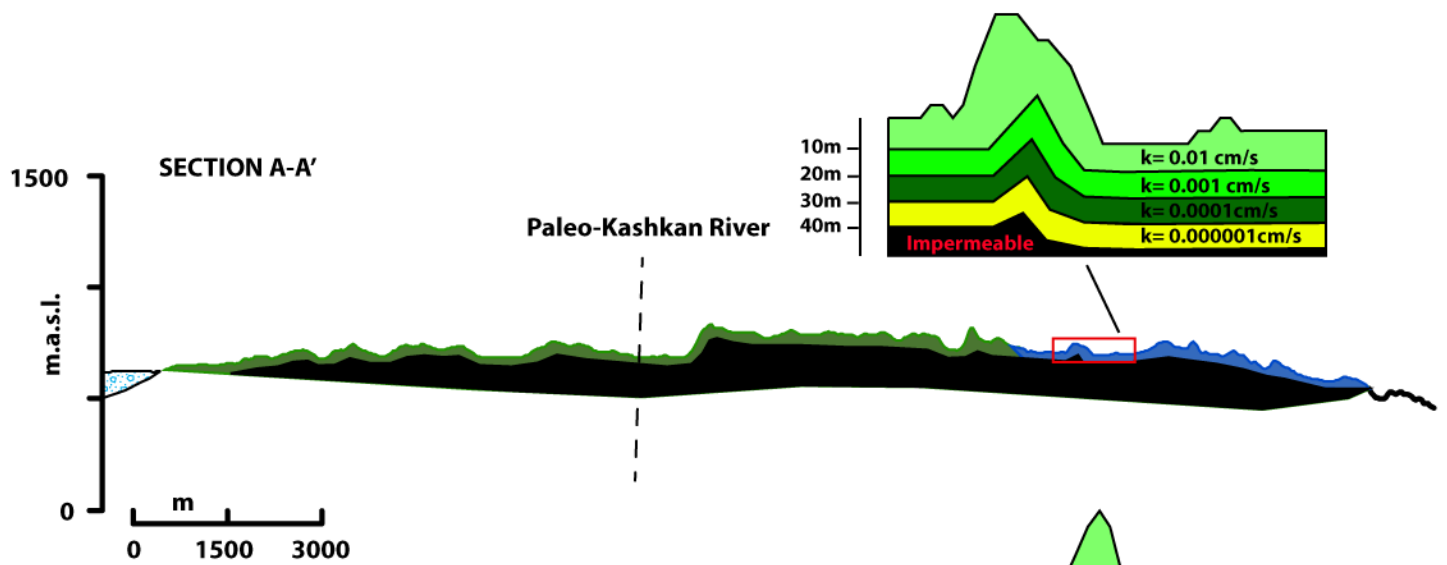


Figure 60 Areas with different permeability based on the laboratory tests performed on the samples of debris matrix



Legend

- Area of the landslide debris with permeability class 1 (Asmari Formation)
- Area of the landslide debris with permeability class 2 (Asmari Formation)
- Area of the landslide debris with Pabdeh-Gurpi Formation
- Impermeable area
- Lacustrine deposits

Figure 61 Permeability section on the debris

Chapter 5- Geological model of the landslide debris

5.1 Material and methodology

Recognizing the topographic condition under landslides debris and estimation of their volume is possible using the combination of geological field investigation, the remote surveying-based approaches and morphometric analyses. Deduced emplacement kinematics of the landslide debris by ridges and blocks density led to the recognition of buried part of the Chenareh-Kuh and Halush-Kuh under the landslide debris. The landslide debris particles distribution and the permeability tests result also confirms the proposed emplacement kinematics of the landslide debris. Therefore, based on these evidences and some outcrops of Gachsaran Formation observed during field surveys (Figure 62 and Figure 63), the basal contact of the landslide debris with the geological substratum was recognized and allowed to speculate on the paleo-valley hidden morphology.



Figure 62 Out crops of Gachsaran Formation along the Seymareh River

Once the paleo-valley hidden morphology was speculated, 7 sections in the NE-SW direction (Figure 63) and 6 sections in the NW-SE direction (Figure 63) were drawn. Then, using DEM with a vertical accuracy of 10m and spatial analyst tools in ArcGIS, the elevation value on the landslide debris surface for each section was extracted. These elevational values for each section were transferred to AutoCAD and the landslide debris vertical limits for each section was estimated (Figure 64, Figure 65, Figure 66, Figure 67, Figure 68, Figure 69 and Figure 70).

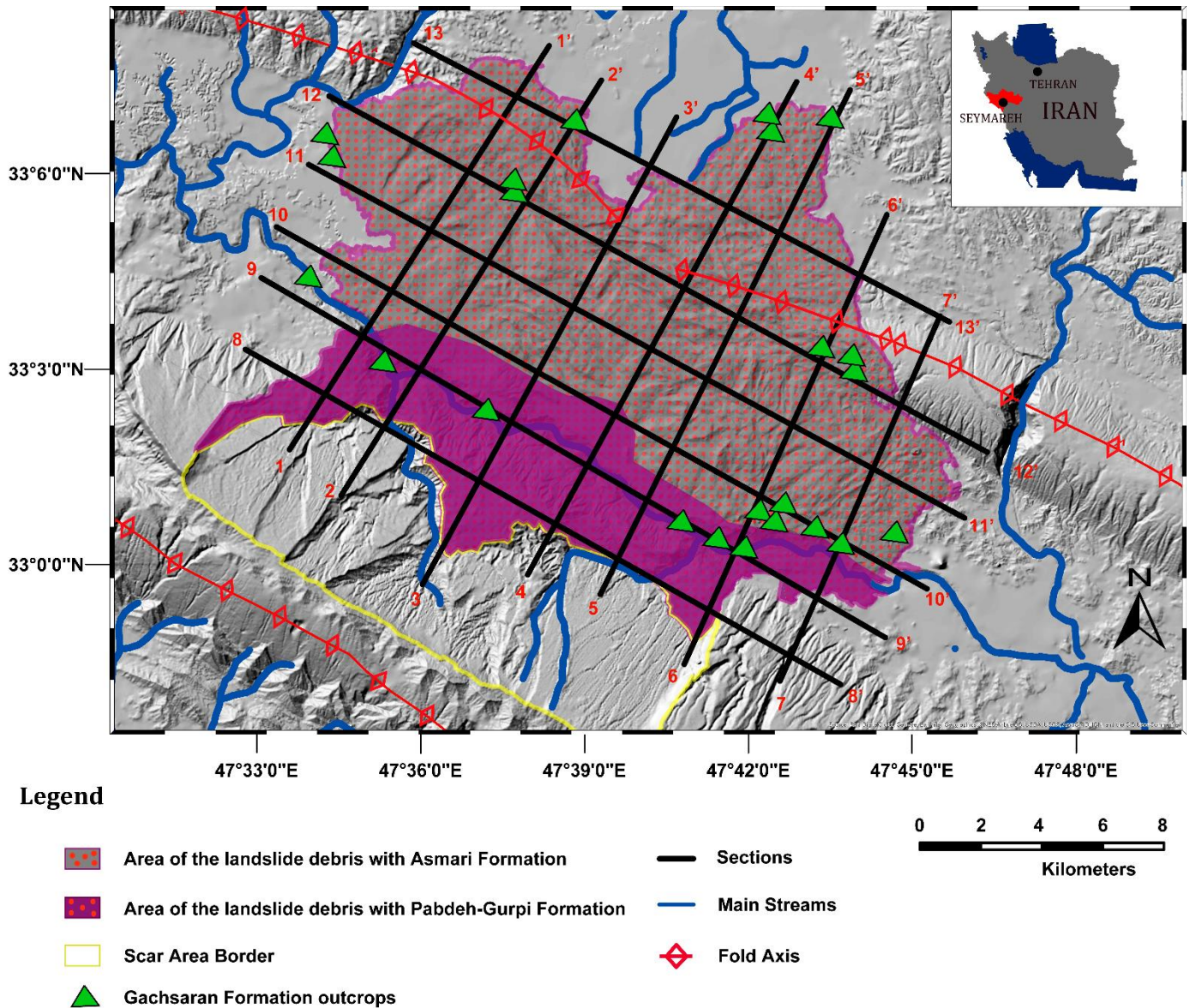


Figure 63 The location of outcrops of Gachsaran Formation and sections

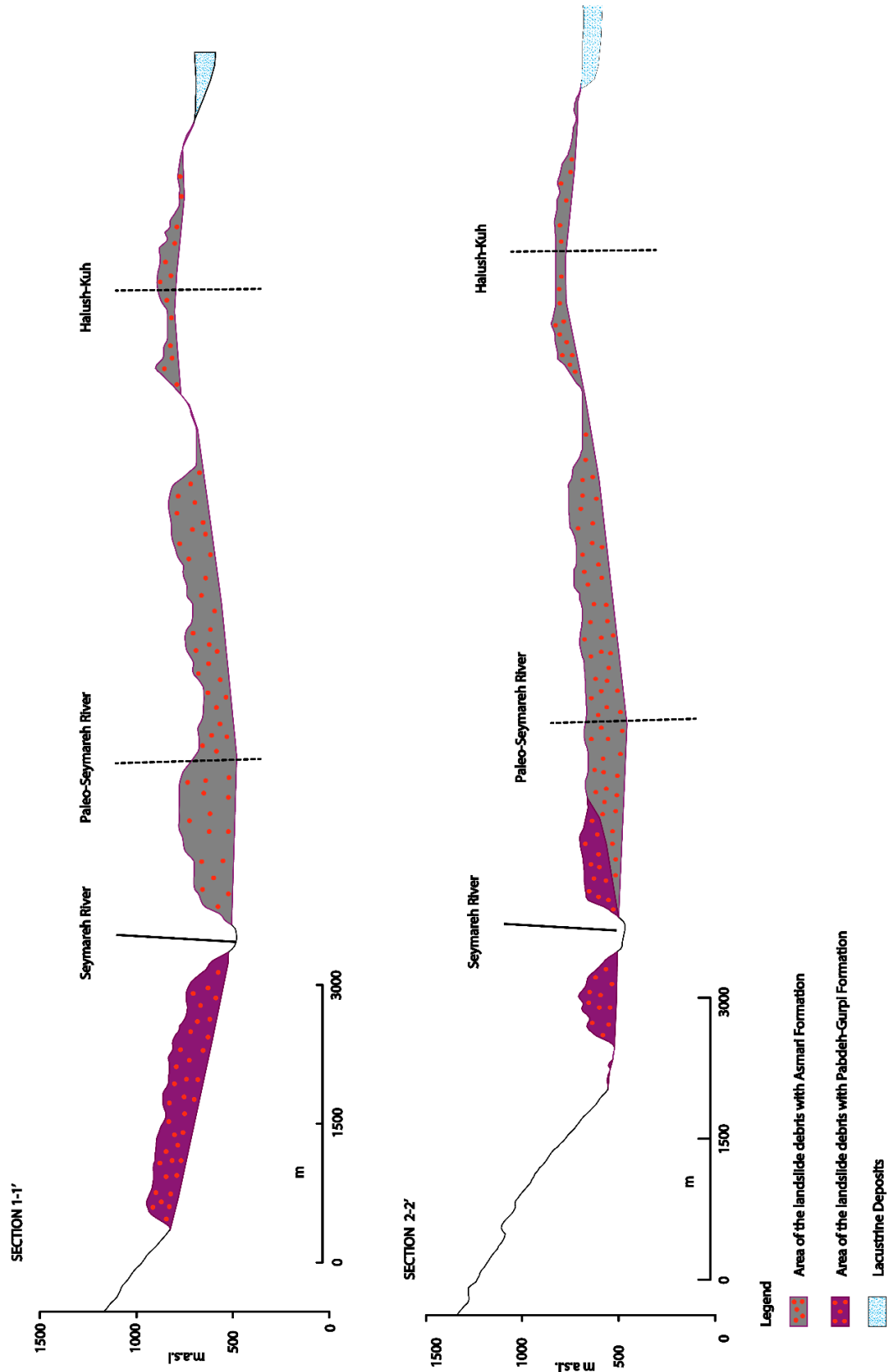


Figure 64 Section 1-1' and 2-2'

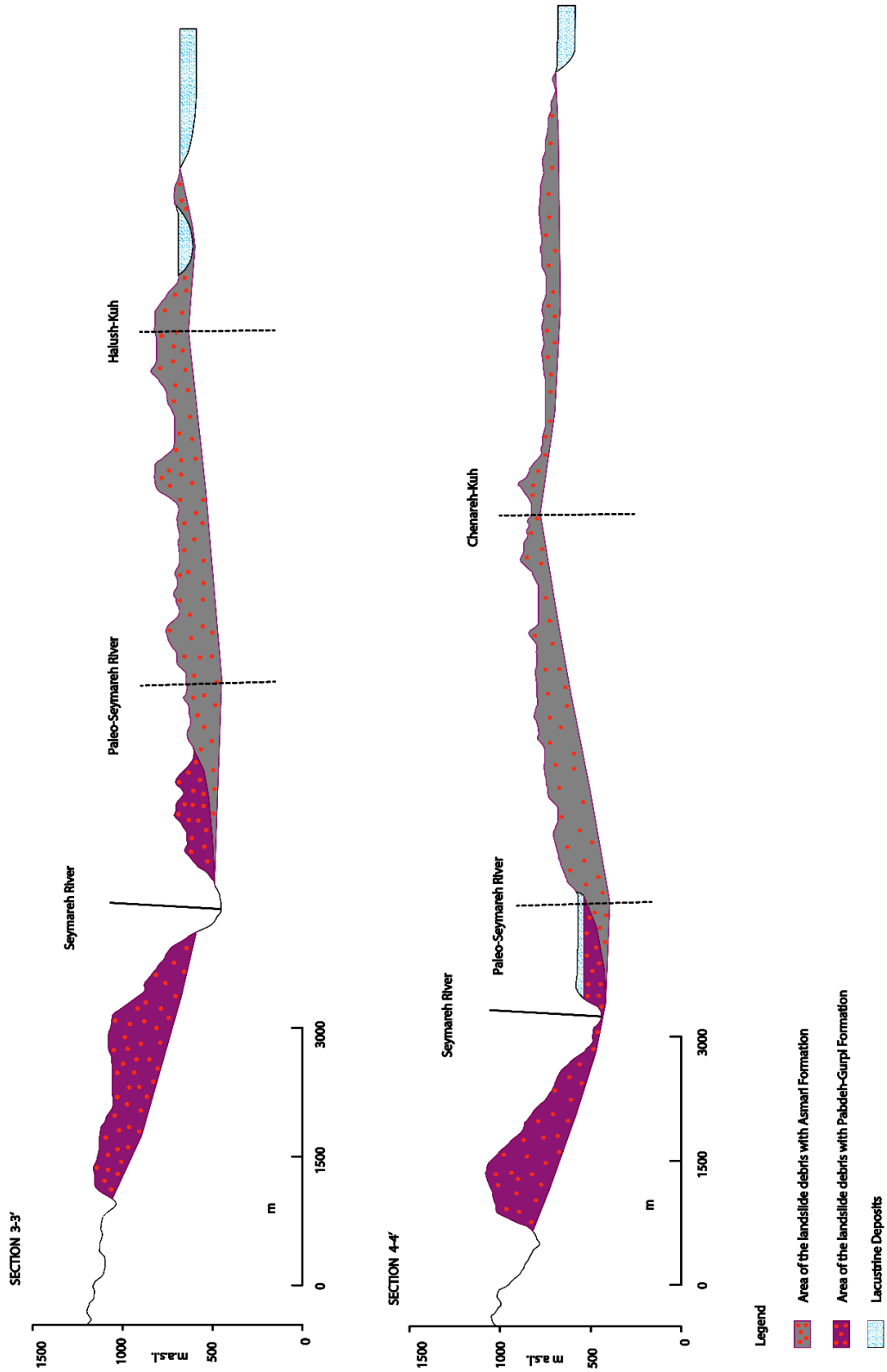


Figure 65 Section 3-3' and 4-4'

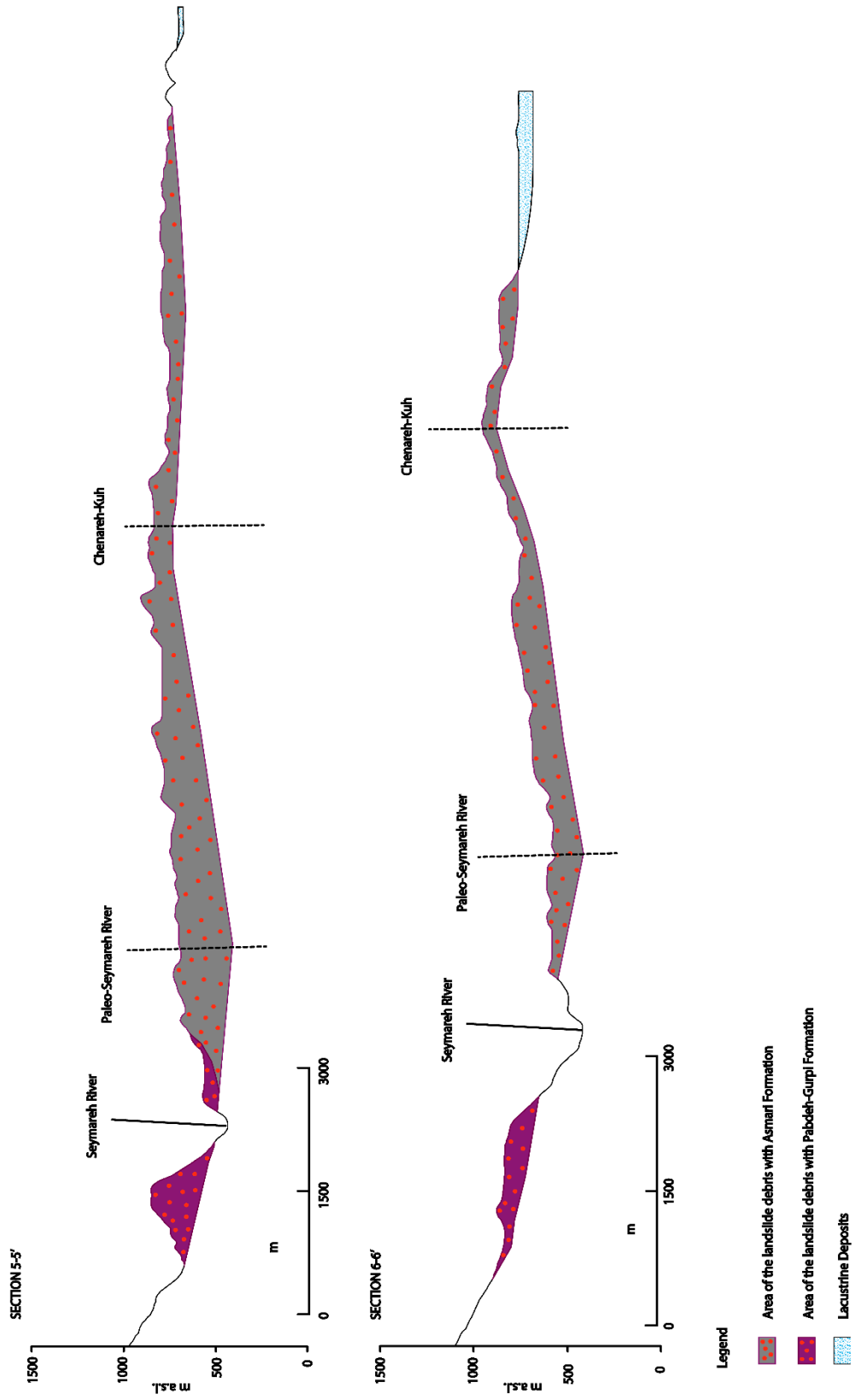


Figure 66 Section 5-5' and 6-6'

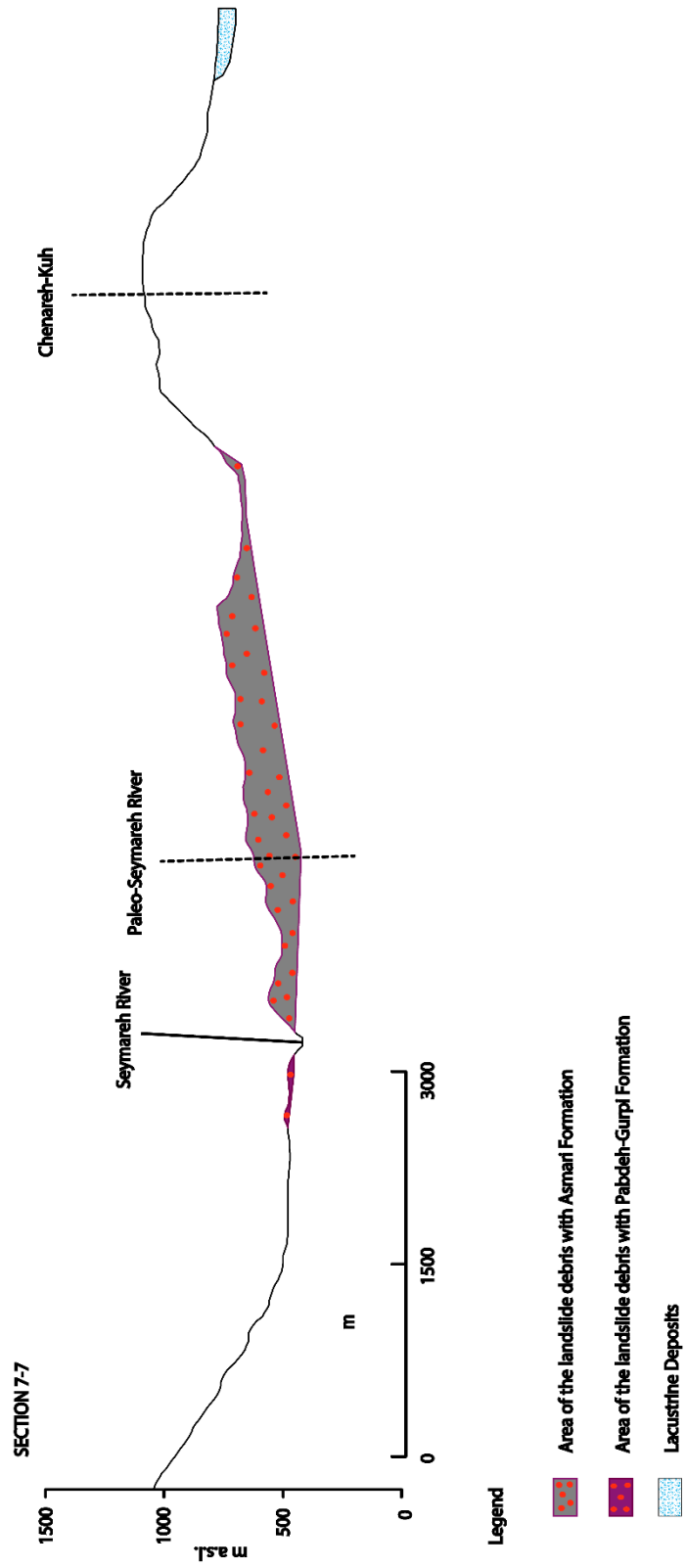


Figure 67 Section 7-7'



Figure 68 Section 8-8' and 9-9'



Figure 69 Section 10-10' and 11-11'

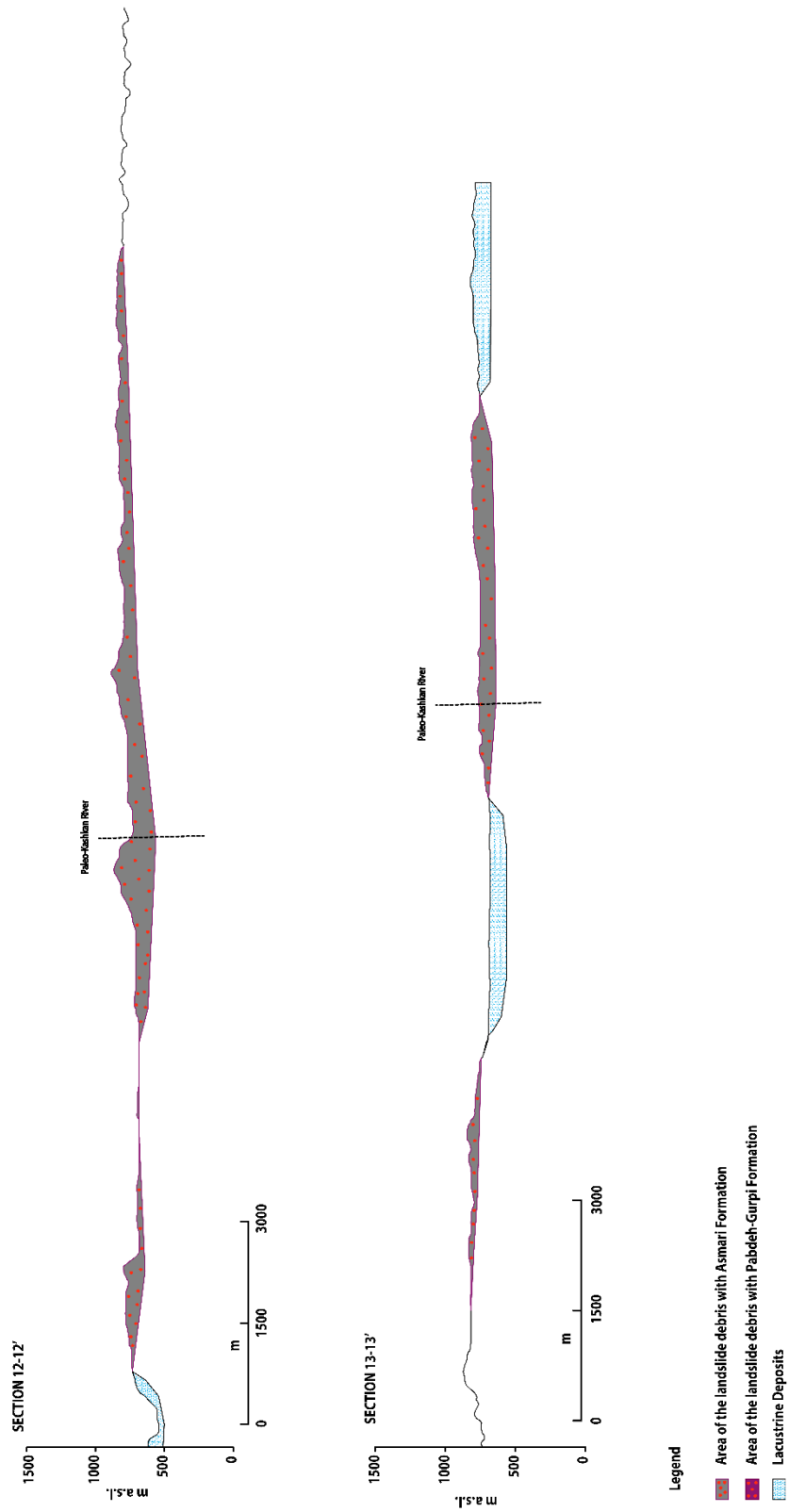


Figure 70 Section 12-12' and 13-13'

5.2 Results

The total area of Seymareh landslide debris was estimated as 188.12 km², 135.36 km² of which belong to the Asmari Formation area and 52.76 km² is shared with the Pabdeh-Gurpi Formation area. The landslide debris has a maximum thickness of 300 and 380 meter in the Asmari and Pabdeh-Gurpi Formation area, respectively. The maximum thickness of the Asmari and Pabdeh-Gurpi Formation area as measured in section 5 and 4 in the middle and proximal portions, respectively. The debris thins toward the edges.

It was measured that the debris has a maximum length of 15 km parallel to runout and 21 km perpendicular to runout. The debris travelled a maximum distance of 19 km from the head scarp of detached area.

It was estimated that the landslide debris have a total volume of 43.97 km³ with 35.76 and 8.20 km³ of the Asmari and Pabdeh-Gurpi Formation debris, respectively. The average thickness of total debris was 233 m. It was calculated that the Asmari Formation debris has an average thickness of 264 m. The landslide dam was cut in the Pabdeh-Gurpi Formation area and a huge volume of the debris belonging to this formation were eroded during cutting. Therefore, it was not logical to calculate the average thickness of Pabdeh-Gurpi Formation debris.

The so derived reconstruction of the paleo valley morphology indicates that paleo Seymareh river was flowing to the NE of the present river gorge (about 2.5km). It also confirms that a part of Halush-Kuh and Chenareh-Kuh are buried under the landslide debris. It is estimated that the landslide debris in the buried part of Halush-Kuh and Chenareh-Kuh have a maximum thickness of about 50 and 130m, respectively. The landslide debris in the paleo valley location which consist of Asmari Formation area has a maximum thickness of 300 meter and decreases along the direction of the debris emplacement. The variation of the debris thickness is related to the presence of Halush-Kuh and Chenareh-Kuh with in the travelling pass of the debris. The kinematics of the debris emplacement, statistical classification and the measured permeability of the debris confirms that during the landslide debris emplacement, the presence of Halush-Kuh and Chenareh-Kuh caused a part of the debris overpasses these two ridges and the rest of the debris swip back to the paleo valley. The results of the permeability tests show that in the areas were the debris swept back, the permeability value is more respect to the rest of the debris area. The statistical classification of the debris also demonstrates the finer material in the same area which confirm the presence of these two ridges in the travelling pass of the debris.

Chapter 6- Discussion

Mechanism of ancient landslides are generally difficult to be studied and deduced since there is not enough data available from the pre-landslide event period (Shoaei 2014). On prehistoric landslide dams there are original and deformed surface features because of erosion process by different natural phenomena and differential movement between landslide dam and the underlying material. Different types of surface features can be recognized on the landslide debris, including ridges, gullies, denudation scarps and blocks. The coincidence of ridges, gullies and blocks at different location on the landslide debris give clues that there is a relationship between these features. By defining some conditions between these features, I was able to identify the original and deformed regions on the landslide debris. Analyzing some of these surface features on the original and deformed regions of a landslide debris were useful for understanding the emplacement of landslide debris and they provide insights for the zonation of debris in sectors characterized by different behavior helping to better constrain failure mechanisms.

So far, few attentions have been given to the Seymareh landslide (Roberts and Evans, 2013) debris as a possible indicator of its emplacement kinematics after the slope collapse. Recognizing the primary and secondary zones within a landslide debris is relevant for understanding where the landforms were not modified by morphogenetic processes which followed the debris emplacement. Therefore, the emplacement kinematics of the Seymareh landslide debris can be inferred from the collected geomorphological evidences within the accumulation area in the primary zones, i.e. kinematic indicators as ridges and blocks (Figure 71). To this aim, the ridges curvature and direction respect to the north were measured. As shown in Figure 71, kinematic arrows deduced from the ridge orientation analysis in the primary zones only, show two main orientation, NE-SW and NW-SE which agree with the proposed emplacement kinematics of the Seymareh landslide debris by Shoaei 2014. The block distribution also revealed that a back and forward motion involved the landslide debris during its emplacement as the huge blocks are distributed not only along the front of the landslide mass but also in its middle zone, where the Chenareh-Kuh ridge is expected to be buried. These evidences led us to confirm what was already been stated in the previous studies (Harrison and Falcon 1937; Watson and Wright 1969; Roberts 2008; Roberts and Evans 2013; Shoaei 2014) that a part of the Chenareh-Kuh and Halush-Kuh anticlines in front of Kabir-Kuh are buried under the landslide debris. It means that during landslide debris emplacement a part of the debris stopped after crushing against the hills, a part of debris

with higher energy overpassed these two anticlines and the rest of debris swept back in the Seymareh paleo-valley. The results of the grain-size distribution analysis as well as of the permeability laboratory tests (Figure 60 and Figure 61) confirm that the part of the debris that overpassed the anticlines as well as the part which swept back to the paleo valley are characterized by similar features: a finer grain-sizing and a lower permeability respect the remnant portion of the Seymareh landslide debris.

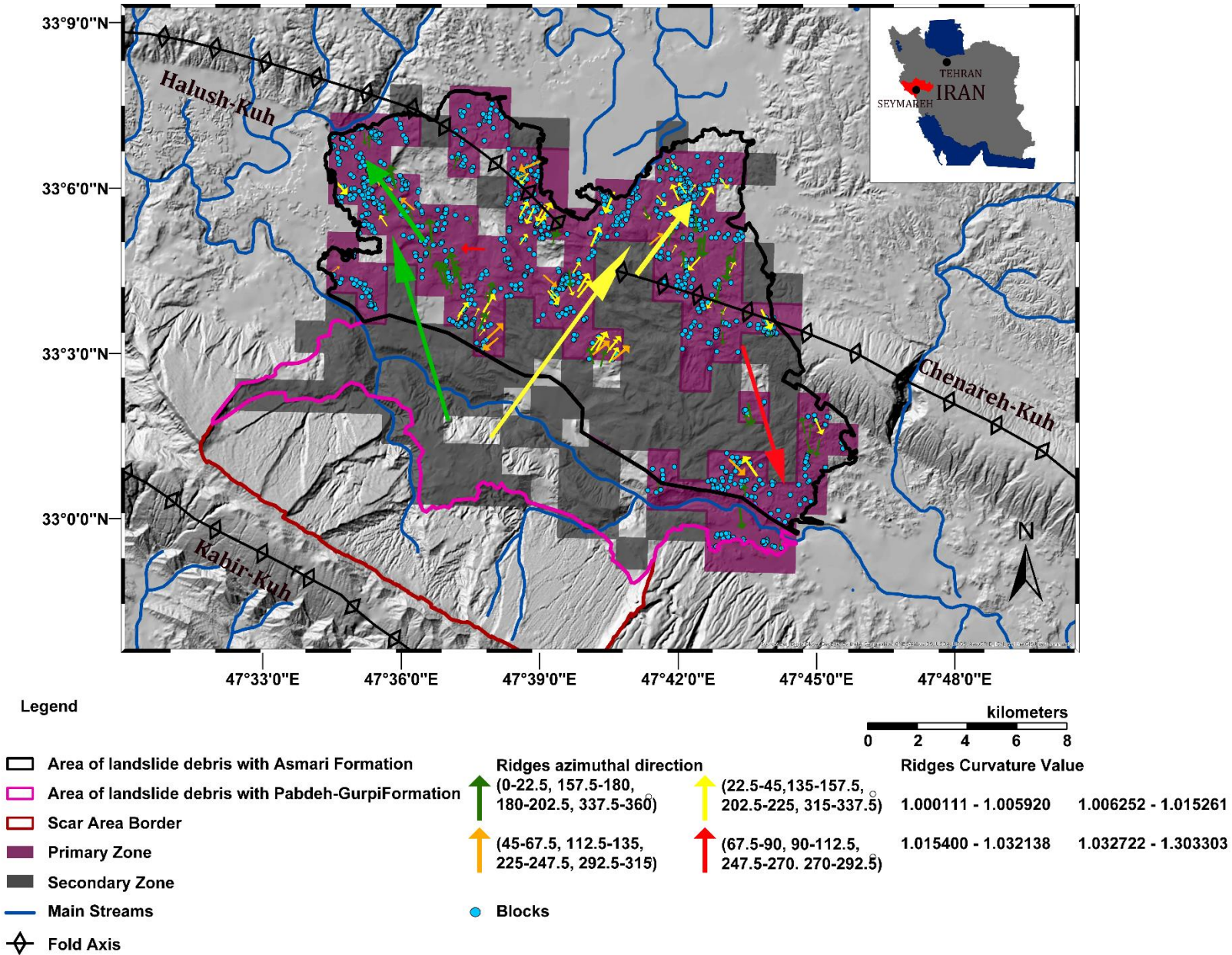


Figure 71 Kinematic indicators on the Seymareh landslide debris

Recognition of the ridges on the surface of the Seymareh landslide debris allowed the identification of three distinct direction of the rock avalanche debris propagation during its emplacement (Figure 72). A possible correlation among the different movement directions and zones of the landslide debris related to specific regime of mass emplacement introduced in literature can also be identified (Dufresne et al. 2010, 2012; Longchamp et al. 2016). The first zone is located in the middle area of the debris and reflects the extension regime during mass emplacement. The ridges in this zone have longer distances from each other and are perpendicular to the run-out direction. The second zone is located at the lateral margins of the landslide debris in the left and right which reflects the compression affecting this area during mass emplacement. The ridges in this zone are close to each other with a tendency to become parallel to the run-out direction. The third zone is located in the distal margins of the landslide debris which reflects shearing and has ridges both parallel and perpendicular to the run-out direction. The results show that the largest ridges are in the medial (and eastern) zone, changing into smaller ridges in the distal part (Dufresne et al. 2010).

Rock avalanche debris such as Seymareh are characterized by poorly sorted grain size distribution, that spatially vary originating relevant heterogeneities within the debris (Pollet and Schneider 2004, Davies and McSaveney 2009, Dufresne and Dunning 2017). Results of grain size distribution analyses of such highly heterogeneous deposits are sensitive to the choice of location and the measurement techniques employed (Konert and Vandenberghe 1997, Beuselinck et al. 1998, Casagli et al. 2003).

Based on the obtained results of USCS classification for the Seymareh landslide debris matrixes, 6 groups of soils were distinguished: high and low compressibility silt (MH and ML), clay of low plasticity (CL), sandy silty clay (CL-ML), clayey sand (SC), silty sand (SM) (Figure 56). Fine-grained soils (ML, MH, CL, CL-ML) has the highest amount and mostly are located in the Asmari Formation debris area in the middle and distal portions of the landslide debris while the coarse-grained (SC and SM) soils are mainly distributed within the debris in the proximity of the detachment area of the Seymareh landslide which are the Pabde-Gurpi Formation debris area.

Classified grain size distribution of Seymareh landslide in the Asmari Formation (Figure 59) debris area demonstrate that the particles with intermediate size (D10:0-0.0025 mm and D60:7.1-20 mm) are mainly distributed in the middle of the debris while the finer particle are distributed in the distal portion in the NW and SE directions. Because the finer particles (D10:0-

0.0025 mm and D60:0-7 mm) in the distal portion of the landslide debris in the NE are buried under the lacustrine deposit of Kashkan Lake (Nooryazdan and Ghobadi 2019), there is no evidence of the finest particles at this portion of the landslide debris. The coarser (D10:0.0026-0.0045 mm and D60:7.1-20 mm) are almost distributed in different portions. Classified grain size distribution in the Pabdeh-Gurpi Formation area shows almost one class of coarse particle (D10:0.0026-0.0045 mm and D60:7.1-20 mm). The huge blocks are distributed not only along the front of the landslide mass but also in its middle zone where the Chenareh-Kuh ridge is expected to be buried.

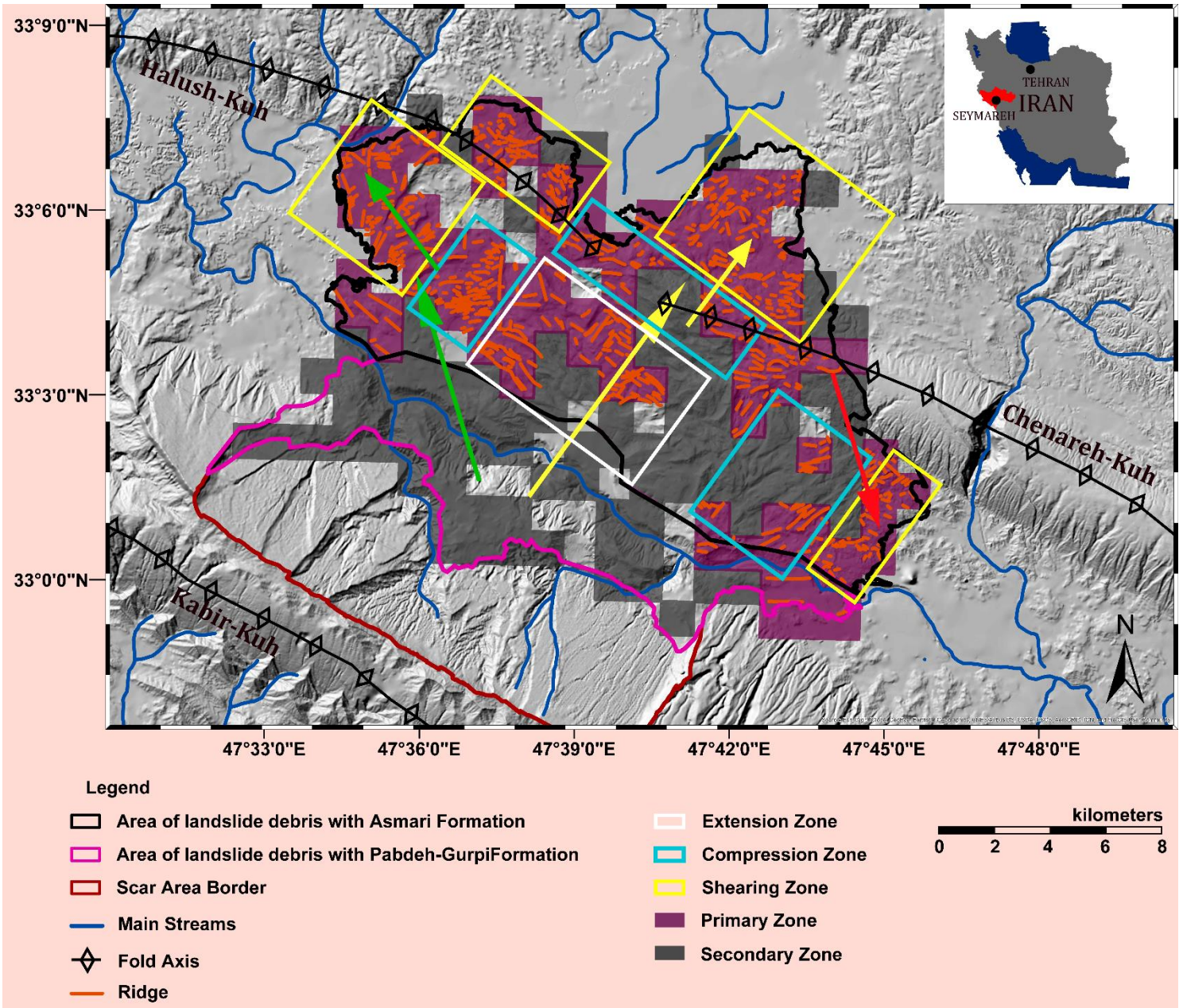


Figure 72 Stress zones formed on the landslide debris during mass emplacement

The similar grain size distribution was interpreted as inverse grading by Cruden and Hungr, 1986. Gray and Thornton 2005 formulated a model for kinetic sieving and proved that the fine particles percolated through the matrix and support less pressure than they should, which had been carried by the coarse particles. The table-top experiment in Pudasaini and Hutter 2007 indicated that the small particles fell through spaces between the coarse particles under the action of gravity. Their observations showed that more and more solid particles were transported to the front and side of the debris flow as the mass moved downslope. They found that shearing caused by different vertical velocities also contributed to the phase-separation during this moving process. Dunning and Armitage 2011 pointed out that the interior of the Falling Mountain and other four rock-avalanche deposits are not inversely graded, and the carapace facies may show inverse grading, but this is only a near surface phenomena. Ren et al. 2018 explored the grain size distribution of Touzhai rock avalanche debris using field investigations, in-situ sieve testing, laboratory screening, X-ray diffraction and scanning electron microscope observations and concluded that inverse grading does not exist in the Touzhai rock avalanche deposit. The presence of large particles on the surface and smaller particles in the lower part of the deposit is the result of rainfall leaching. The bedding planes, columnar joints and vesicular-amygdaloidal defects, combined with tectonic discontinuities and weathering products create pre-fractures in the un-disaggregated source rock mass, which plays a decisive role in the deposit gradation, texture and composition.

Recent literature agree that inverse grading is a false impression and any inverse grading is limited to the upper deposit parts (Dunning 2006, Genevois et al. 2006, Crosta et al. 2007, Dunning and Armitage 2011, Weidinger et al. 2014).

The results of particle size distribution on 63 matrix sampled within the Seymareh Landslide debris surface show that there is a change in the grain size distribution along the event path. It means during the event, larger blocks traveled farther and were fragmentated more which results in producing finer particles among huge blocks in the distal areas.

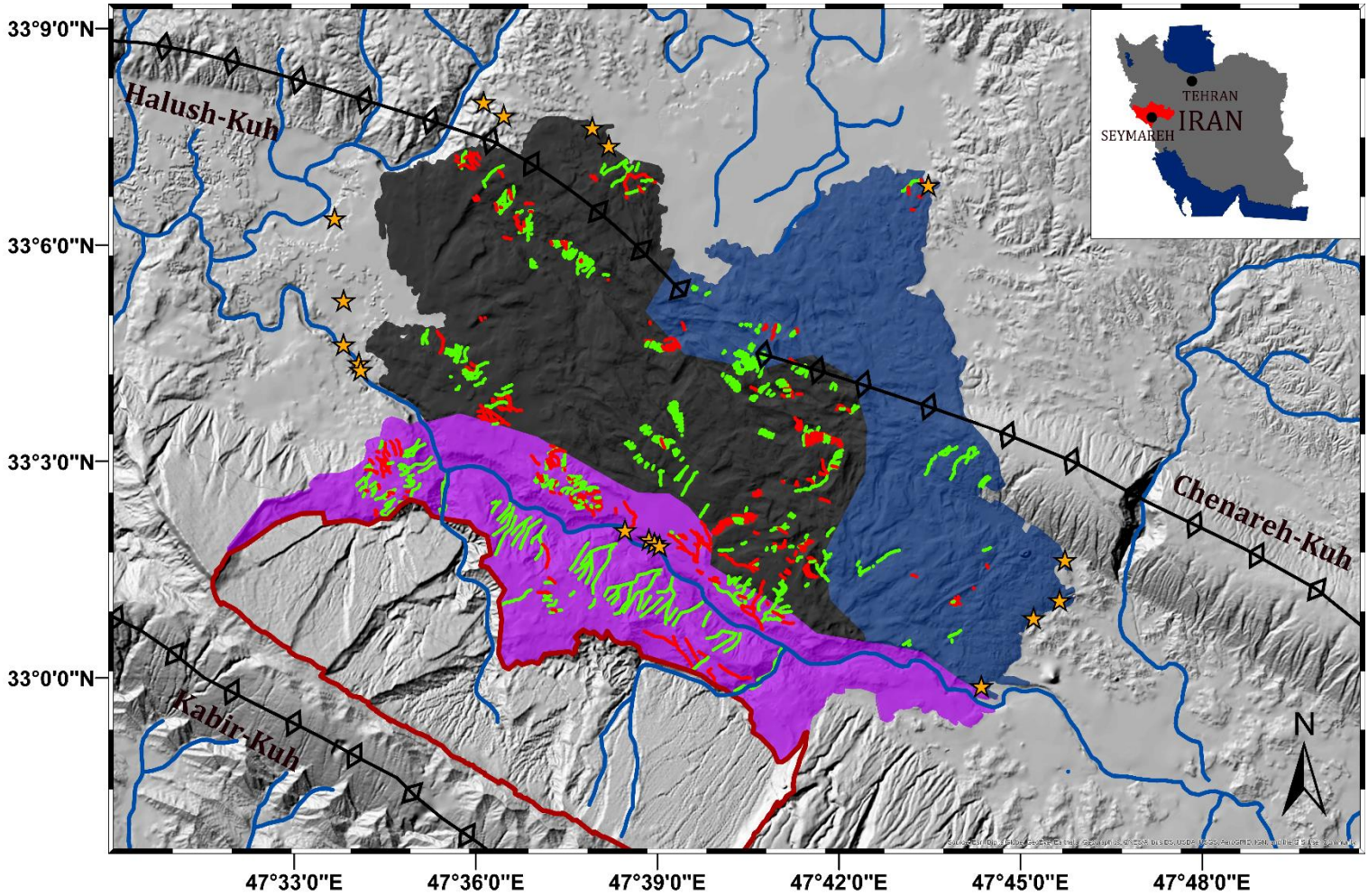
Such an evidence coupled with the kinematic indicators and the Asmari Formation blocks distribution confirms what stated by Roberts and Evans (2013), i.e. that during initial failure the Asmari Formation limestone (upper plate) overrode the lower plates to travel the farthest. Lower weaker plates were involved in the slope collapse immediately after the stiffer plate of the Asmari Formation. The lack of preservation of intact portions of the collapsed stratified rocks, the intense fragmentation of the involved rocks in the landslide debris, the huge block cluster distribution

which reveals a coarsening forward sizing and the main concentration of the huge blocks all along the perimetral zone of the landslide debris justify that the Seymareh landslide resulted in a rock avalanche; moreover, the kinematic indicators coupled with the huge blocks distribution also outline that such a rock avalanche consisted in an instantaneous and single event of generalized slope failure. Nevertheless, as discussed before, the debris emplacement resulted in a complex spatial pattern as directions of flow propagation (and corresponding kinematic zones) are differentiated.

The paleo valley morphology of the Seymareh landslide, reconstructed on the basis of the field evidence collected for this research, allows to estimate the volume of the debris and allowed to recognize undisturbed outcrops of the Gachsaran Formation and their location at the original elevation; moreover, the distribution of the kinematic indicators extracted from ridges direction as well as the block clusters location within the landslide mass suggest the position of the depocenter of the Seymareh valley before the landslide emplacement. This paleo-morphology indicates that paleo Seymareh River was flowing to the NE of the present river gorge which agrees with Roostai et al. 2018. The estimated volume of the landslide debris (43.97 km^3) calculated by reconstruction of paleo valley morphology is in good accordance with the estimated volume of the debris by Roberts et al. 2013 which shows high accuracy of reconstructed paleo morphology of the Seymareh landslide debris area in the current research.

Calculating the direction of the gullies in the secondary regions, where the erosion process erodes the landslide debris surface and created the modified landforms, in combination with grain size analysis and permeability tests helps us to better interpret the movement process which terminated to the landslide dam cutting. As it can be seen in Figure 73, in one hand the gullies in the south part of the debris in the Pabdeh-Gurpi Formation area in the left side of the river mainly have a direction between 0-90 degree and the gullies in the right side of the river are between 90-180 which are perpendicular to other side of the river. On the other hand, this area is the boundary between Pabdeh-Gurpi and Asmari Formations debris. There are several springs in this area too. Based on the results of permeability laboratory tests, a not negligible change in the debris permeability can be observed within the landslide debris and related to the upper part of the debris in the Asmari Formation area. There is another change of the permeability related to the intersection of the Asmari Formation and Pabdeh Gurpi Formation.

Moreover, it can be deduced that overflowing of the Seymareh lake water on the landslide debris and the surface erosion of the debris by gullies in combination with the change of the permeability and springs effect from basement led to the complete failure of the Seymareh landslide dam.



Legend

- | | | |
|-----------------------------------------------------------------------------------------------------------------------------------------------------------------------------------------------------------------------------------------------------------------------------------------------------------------------------------------------------------------------------------------------------------------------------------------------------------------------------------------------------------------------------------------------------------------------------------------------------------------------------------------------------------------------|---------------------------------------------------------------------------------------------------------------------------------------------------------------------------------------------------------------------------------------------------------------------------------------------------------------------------------------------------------------------------------------------------------------------------------------------------------------------------------------------------------------------------------------------------------------------------------------|----------------------------------------------------------------------------------------------------------------------------------------------------------------------------------------------------------------------------------------------------------------------------------------------------------------------------------------------------------|
| <ul style="list-style-type: none"> Area of the landslide debris with Asmari Formation and permeability class 1 Area of the landslide debris with Asmari Formation and permeability class 2 Area of landslide debris with Pabdeh-Gurpi Formation and Permeability class 1 | <ul style="list-style-type: none"> Scar Area Border Fold Axis Main Streams Spring | <ul style="list-style-type: none"> Gullies with azimuthal direction between 0-90 between 90-180 |
|-----------------------------------------------------------------------------------------------------------------------------------------------------------------------------------------------------------------------------------------------------------------------------------------------------------------------------------------------------------------------------------------------------------------------------------------------------------------------------------------------------------------------------------------------------------------------------------------------------------------------------------------------------------------------|---------------------------------------------------------------------------------------------------------------------------------------------------------------------------------------------------------------------------------------------------------------------------------------------------------------------------------------------------------------------------------------------------------------------------------------------------------------------------------------------------------------------------------------------------------------------------------------|----------------------------------------------------------------------------------------------------------------------------------------------------------------------------------------------------------------------------------------------------------------------------------------------------------------------------------------------------------|



Figure 73 Evidences that helps to recognize the failure mechanism of the landslide debris (gullies azimuthal direction in the secondary regions, springs and permeabilities)

For the forecasting of the landslide dam stability, Canuti et al. (1998) and Casagli and Ermini (1999), Ermini and Casagli (2003), Tacconi Stefanelli et al. 2016 proposed four indexes that are the Blockage Index, Dimensionless Blockage Index, Morphological Obstruction Index and Hydromorphological Dam Stability Index (Table 16). In order to evaluate the efficiency of these indexes, the formation and the stability of the Seymareh and Kashkan landslide dams using the parameters presented in Table 16 were evaluated. The results are presented in Table 17.

Table 16 Morphometric Parameters of the Seymareh Landslide

Morphometric Parameters	Seymareh landslide dam	Kashkan Landslide dam
The landslide dam volume, V_d (km ³)	43.97	43.97
The catchment area, A_b (km ²) (Report of Iranian Ministry of Energy)	974.9	2073
The maximum crest height of the landslide dam, H_d (m)	380	230
The landslide volume, V_l (km ³) (Roberts and Evans, 2013)	38	38
The width of the dammed valley, W_v (km)	12	14
The local longitudinal slope of the channel bed, S	0.0012	0.011

Table 17 Evaluation of the Seymareh and Kashkan landslide dams by some indices

Index	Landslide dam stability	Index values for Seymareh landslide dam	Index values for Kashkan landslide dam
Blockage Index	BI = 3 threshold ratio for formation lakes 4 > BI > 3 unstable dams 5 > BI > 4 uncertainties BI > 5 stable and existing lakes	7.65	7.32
Dimensionless Blockage Index	DBI < 2.75 stability domain 2.75 < DBI < 3.08 uncertain domain DBI > 3.08 instability domain	0.92	1.03
Morphological Obstruction Index	MOI > 4.60 formed dam 3 < MOI < 4.60 uncertain evolution MOI < 3 not formed dam	6.5	6.43
Hydromorphological Dam Stability Index	HDSI > 7.44 stable dam 5.74 > HDSI < 7.44 formed uncertain evolution HDSI < 5.74 unstable dam	10.51	9.22

Blockage Index, $BI = \log \frac{V_d}{A_b}$ where V_d is the landslide dam volume (m³) and A_b the catchment area (km²), Dimensionless Blockage Index, $DBI = \left(\frac{A_b \times H_d}{V_d} \right)$ where A_b is the catchment area (m²), H_d the maximum crest height of

landslide dam (m) and V_d is the landslide dam volume (m^3), Morphological Obstruction Index, $MOI = \log \frac{V_l}{W_v}$ where V_l is the landslide volume (m^3) and W_v the width of the dammed valley (m), Hydro morphological Dam Stability Index, $HDSI = \log \frac{V_l}{A_b \times S}$ where V_l is the landslide volume (m^3), A_b the catchment area (km^2) and S the local longitudinal slope of the channel bed.

As it can be seen in Table 17, the BI and MOI indexes correctly predicted the formation of the Seymareh and Kashkan landslide dams. In the case of their stability, all these indexes correctly predicted the stability of the Kashkan landslide dam but for the Seymareh landslide dam, none of these indexes were able to correctly predict its stability. Based on different proposed indexes for the evaluation of the formation and stability of landslide dams, the stability of landslide dams is depends on the morphology (Casagli, and Ermini, 1999, Hermanns et al. 2004, Hewitt 1998), volume of the debris (Tacconi Stefanelli et al. 2016), composition of the material including different lithological behavior (Costa and Schuster, 1998) as well as the rates of sedimentation and/or transport of alluvial sediments in the lake (Weidinger, 2011). The analysis of Seymareh and Kashkan landslide dams presented in this thesis shows that there are other additional important factors affecting the stability of landslide dams including:

- 1- kinematics of the debris emplacement and travelling distance
- 2- the involved lithologies and their fragmentation rate
- 3- grain, boulder and block size distribution of the material composing the landslide dam
- 4- permeability of the material composing the landslide dam

Therefore, a more comprehensive index for evaluating the formation and evolution of the landslide dam should be probably taken into consideration all these effective parameters.

Chapter 7- Conclusions

The current PhD thesis aims to find key interpretative elements and parameters for describing the longevity, emplacement kinematics and the rupture style of the giant Seymareh landslide dam (western Zagros Mts., Iran), as a function of dam morphometry, sedimentology and geotechnical properties.

To this aim, this thesis proposed a statistical approach based on the analysis of landforms like ridges, gullies and blocks to distinguish primary (original) and secondary (modified) regions within the Seymareh landslide debris. Based on the new statistical approach and analyzing the kinematic indicators (like ridges and blocks) in the primary region on the Seymareh landslide debris, it was possible to detail the mechanism of the landslide debris emplacement.

Based on the distribution of huge blocks and the orientation of the kinematic indicators it was deduced that the Seymareh landslide was a single-event rock avalanche filling a paleo valley enclosed between two anticline ridges (the Chenareh ridge and the Halush ridge).

By understanding the emplacement sequence and evidences of the Gachsaran Formation outcrops along the Seymareh river in the cut area of the debris, the topography of the landslide debris area before the event was reconstructed. By utilizing the reconstructed paleo morphology of the debris area before the event and several section on the debris, it was possible to estimate the volume of the landslide debris. It also helped to recognize the paleo Sermareh and Kashkan River location.

The USCS classification of the matrix sampled within the landslide debris allowed to recognize SC, SM, CL, CL-ML, MH and ML soils. Fine-grained soils (CL, CL-ML, MH and ML) mainly compose the debris matrix in the middle to distal portions, while the coarse-grained (SC and SM) soils are mainly distributed within the debris in the proximity of the detachment area of the Seymareh landslide. This could be explained by a composed sequence of debris emplacement which involved the fragmented stiff plate of the Asmari Formation, filled the paleo valley of the Seymareh River so favoring, in a following step, the run out of the Pabdeh-Gurpi Formation.

Classification of the debris for particle up to 50cm, from the debris surface down to a depth of 5m allowed to recognize that on the surface of the landslide debris there is inverse grading which took place during its emplacement.

By performing the permeability tests on the finer part of the landslide debris (passing from sieve #40) and understanding the kinematics of the mass emplacement, it was possible to

understand that the finer part of the debris which are from the same formation of original rock mass have the same permeability but the area of the debris that during emplacement of the debris swept back to the paleo valley is characterized by a lower permeability, similarly to the most distal zone of the landslide debris.

In order to test the efficiency of some indexes proposed in the literature for evaluating the formation and stability of landslide dams, parameters (e.g. the local longitudinal slope of the channel bed, the width of the dammed valley, the landslide volume, the maximum crest height of the landslide dam, the catchment area, the landslide dam volume) related to the Seymareh landslide were collected or calculated to be applied to these indexes. Some of these indexes correctly predicted the formation of the Seymareh and Kashkan landslide dams. In the case of their stability, all these indexes correctly predicted the stability of the Kashkan landslide dam but for the Seymareh landslide dam, none of these indexes were able to correctly predict its stability. Based on different proposed indexes for the evaluation of the formation and stability of landslide dams, the stability of landslide dams depends on the morphology (Casagli, and Ermini, 1999, Hermanns et al. 2004, Hewitt 1998), volume of the debris (Tacconi Stefanelli et al. 2016), composition of the material including different lithological behavior (Costa and Schuster, 1998) as well as the rates of sedimentation and/or transport of alluvial sediments in the lake (Weidinger, 2011). The analysis of Seymareh and Kashkan landslide dams presented in this thesis shows that there are other additional important factors affecting the stability of landslide dams including:

- 1- kinematic of the debris emplacement and travelling distance
- 2- the involved lithologies and their fragmentation rate
- 3- grain, boulder and block size distribution of the material composing the landslide dam
- 4- permeability of the material composing the landslide dam

Therefore, a comprehensive index for evaluating the formation and evolution of the landslide dam should take into consideration all these effective parameters.

References

- Aghanabati, A. (2004). Geology of Iran. Geological survey of Iran, Tehran. pp, 578-582.
- ASTM. (2017). Standard D2487-17, Standard Practice for Classification of Soils for Engineering Purposes (Unified Soil Classification System), ASTM International, West Conshohocken, PA, www.astm.org. DOI: 10.1520/D2487-17
- ASTM. (2017). Standard D4318-17e1, Standard Test Methods for Liquid Limit, Plastic Limit, and Plasticity Index of Soils, ASTM International, West Conshohocken, PA, 2017, www.astm.org. DOI: 10.1520/D4318-17E01
- ASTM. (2007). Standard D422-63(2007) e2, Standard Test Method for Particle-Size Analysis of Soils (Withdrawn 2016), ASTM International, West Conshohocken, PA, 2007, www.astm.org. DOI: 10.1520/D0422-63R07E02
- ASTM. (2015). Standard D2167-15, Standard Test Method for Density and Unit Weight of Soil in Place by the Rubber Balloon Method, ASTM International, West Conshohocken, PA, 2015, www.astm.org. DOI: 10.1520/D2167-15
- ASTM. (2006). Standard D2434-68(2006), Standard Test Method for Permeability of Granular Soils (Constant Head) (Withdrawn 2015), ASTM International, West Conshohocken, PA, 2006, www.astm.org. DOI: 10.1520/D2434-68R06
- Agard, P., Omrani, J., Jolivet, L., & Mouthereau, F. (2005). Convergence history across Zagros (Iran): Constraints from collisional and earlier deformation, *Int. J. Earth Sci.*, 94(3), 401–419.
- Alavi, M. (2004). Regional stratigraphy of the Zagros fold-thrust belt of Iran and its pro-foreland evolution. *Am. J. Sci.*, 304(1), 1-20
- Azimi, S. (2012). The effect of seymareh's large slip on the formation and evolution of lake terraces. Degree (MSc) diss., University of Tehran. (Published in Persian)
- Baharvand, S. (2008). Seismicity analysis of Poledokhtar area and its relationship to the Seymareh landslide. Degree (PhD) diss., Islamic Azad University, science and research branch. (Published in Persian)
- Beiranvand, H., Entezari, M., & Seif, A. (2016). Analysis the morphometric features of Kabirkooch Landslide. *Geographical Sciences Journal*, 16(41): 31-53. (Published in Persian).
- BHRC. (2007). Iranian Code for Seismic Resistant Design of Buildings, Standard No 2800, Third Edition 2007, Building and Housing Research Centre, Iran. (Published in Persian).
- Bolongaro-Crevenna, A., Torres-Rodriguez, V., Sorani, V., Frame, D., & Ortiz, M. A. (2005). Geomorphometric analysis for characterizing landforms in Morelos State, Mexico. *Geomorphology*, 67(3-4), 407-422.
- Bonnard, C. (2011). Technical and human aspects of historic rockslide-dammed lakes and landslide dam breaches. In: EVANS S., HERMANN S., STROM A., SCARASCIA-MUGNOZZA G. (EDS.). *Natural*

and Artificial Rockslide Dams. *Lecture Notes in Earth Sciences*, 101-122, Springer, New York, London, Dordrecht, Heidelberg.

Blott, S. J., & Pye, K. (2001). GRADISTAT: a grain size distribution and statistics package for the analysis of unconsolidated sediments. *Earth surface processes and Landforms*, 26(11), 1237-1248.

Canny, J., 1986. A computational approach to edge detection. *IEEE Transactions on Pattern Analysis and Machine Intelligence*, 8(6), 679–698.

Casagli, N., & Ermini, L. (1999) Geomorphic analysis of landslide dams in the Northern Apennine. *Trans Jpn Geomorphol* 20(3):219–249.

Casagli, N., Ermini, L., & Rosati, G. (2003). Determining grain size distribution of the material composing landslide dams in the Northern Apennines: sampling and processing methods. *Engineering geology*, 69(1-2), 83-97.

Chen, X. Q., Cui, P., Li, Y., & Zhao, W. Y. (2011). Emergency response to the Tangjiashan landslide-dammed lake resulting from the 2008 Wenchuan Earthquake, China. *Landslides*, 8(1), 91-98.

Church, M. (2013). Refocusing geomorphology: Field work in four acts. *Geomorphology*, 200, 184-192.

Coblentz, D., Pabian, F., & Prasad, L. (2014). Quantitative geomorphometrics for terrain characterization. *International Journal of Geosciences*, 5(3), 247.

Coico, P., Calcaterra, D., De Pippo, T., & Guida, D. (2013). A preliminary perspective on landslide dams of Campania region, Italy. In *Landslide Science and Practice* (pp. 83-90). Springer, Berlin, Heidelberg.

Cooper, L.R., Haverland, R.L., Vendricks, D.M., & Knisel W.G. (1984). Microtac particle-size analyzer: An alternative particle-size determination method for sediment and soils. *Soil, Science*, 138(2), 138-146.

Costa, J. E., & Schuster, R. L. (1988). The formation and failure of natural dams. *Geological society of America bulletin*, 100(7), 1054-1068.

Cruden, D. M., & Varnes, D. J. (1996). *Landslides: investigation and mitigation*. Chapter 3-Landslide types and processes. *Transportation research board special report*, (247).

Cui, P., Zhu, Y. Y., Han, Y. S., Chen, X. Q., & Zhuang, J. Q. (2009). The 12 May Wenchuan earthquake-induced landslide lakes: distribution and preliminary risk evaluation. *Landslides*, 6(3), 209-223.

Dal Sasso, S. F., Sole, A., Pascale, S., Sdao, F., Bateman Pinzón, A., & Medina, V. (2014). Assessment methodology for the prediction of landslide dam hazard. *Natural Hazards and Earth System Sciences*, 14(3), 557-567.

De Blasio, F. V., & Crosta, G. B. (2014). Simple physical model for the fragmentation of rock avalanches. *Acta Mechanica*, 225(1), 243-252.

Dehn, M., Gärtner, H., & Dikau, R. (2001). Principles of semantic modeling of landform structures. *Computers & Geosciences*, 27(8), 1005-1010.

- Delchiaro M., Della Seta M., Martino M., Dehbozorgi M. & Nozaem R. (2019a). Reconstruction of river valley evolution before and after the emplacement of the giant Seymareh rock avalanche (Zagros Mts., Iran). *Earth Surf. Dynam.*, 7, 929–947, <https://doi.org/10.5194/esurf-7-929-2019>.
- Delchiaro, M., Rouhi, J., Della Seta, M., Martino, M., Dehbozorgi, M., & Nozaem, R. (2019b). Geostructural and geomorphic constraints for landscape evolution modeling and stress-strain numerical analysis of the giant Seymareh landslide (Zagros Mts., Iran). *Proceedings of the 2019 EGU General Assembly*. 7-12 April 2019, Wien, Austria.
- Della Seta, M., Esposito, C., Marmoni, G. M., Martino, S., Mugnozsa, G. S., & Troiani, F. (2017). Morpho-structural evolution of the valley-slope systems and related implications on slope-scale gravitational processes: New results from the Mt. Genzana case history (Central Apennines, Italy). *Geomorphology*, 289, 60-77.
- De Mets, C., Gordon, R.G., Argus, D.F., and Stein, S. (1994). Effects of recent revisions to the geomagnetic reversal time scale on estimates of current plate motions, *Geophys. Res. Lett.*, 21, 2191-2194.
- DeMorgan, J. (1895). *Mission scientifique en Perse: Etudes Geogr.*, v. 2, 331 p.
- Detert, M., & Weitbrecht, V. (2012). Automatic object detection to analyze the geometry of gravel grains—a free stand-alone tool. In *River flow* (pp. 595-600). Taylor & Francis Group London.
- Detert, M., & Weitbrecht, V. (2013). User guide to gravelometric image analysis by BASEGRAIN. In *12th International Symposium on River Sedimentation (ISRS)* (pp. 165-165).
- Do Couto Fernandes, M., dos Santos, T. L. C., Coura, P. H. F., de Menezes, P. M. L., & Graça, A. J. S. (2013). Modeled surface observations for spatial analysis of landscape dynamics. *Journal of Geographic Information System*, 5(04), 409.
- Drăguț, L., & Blaschke, T. (2006). Automated classification of landform elements using object-based image analysis. *Geomorphology*, 81(3-4), 330-344.
- Dufresne, A., Davies, T. R., & McSaveney, M. J. (2010). Influence of runout-path material on emplacement of the Round Top rock avalanche, New Zealand. *Earth Surface Processes and Landforms: The Journal of the British Geomorphological Research Group*, 35(2), 190-201.
- Dufresne, A. (2012). Granular flow experiments on the interaction with stationary runout path materials and comparison to rock avalanche events. *Earth Surface Processes and Landforms*, 37(14), 1527-1541.
- Dufresne, A., Bösmeier, A., & Prager, C. (2016). Sedimentology of rock avalanche deposits—case study and review. *Earth-science reviews*, 163, 234-259.
- Dufresne, A., & Dunning, S. A. (2017). Process dependence of grain size distributions in rock avalanche deposits. *Landslides*, 14(5), 1555-1563.

- Dufresne, A., Geertsema, M., Shugar, D. H., Koppes, M., Higman, B., Haeussler, P. J., ... & Gulick, S. P. S. (2018). Sedimentology and geomorphology of a large tsunamigenic landslide, Taan Fiord, Alaska. *Sedimentary Geology*, 364, 302-318.
- Duman, T. Y. (2009). The largest landslide dam in Turkey: Tortum landslide. *Engineering Geology*, 104(1-2), 66-79.
- Dunning, S. A., Petley, D. N., Rosser, N. J., & Strom, A. L. (2005, May). The morphology and sedimentology of valley confined rock-avalanche deposits and their effect on potential dam hazard. In *Proceedings of the International Conference on Landslide Risk Management*, Edited by O. Hungr, R. Fell, R. Couture, and E. Eberhardt. Taylor & Francis, Balkema, London (pp. 691-701).
- Dunning, S. A. (2006). The grain size distribution of rock-avalanche deposits in valley-confined settings. *Italian Journal of Engineering Geology and Environment*, 1, 117-121.
- Dunning, S. A., Rosser, N. J., Petley, D. N., & Massey, C. R. (2006). Formation and failure of the Tsatichhu landslide dam, Bhutan. *Landslides*, 3(2), 107-113.
- Dunning, S. A., & Armitage, P. J. (2011). The grain-size distribution of rock-avalanche deposits: implications for natural dam stability. In *Natural and artificial rockslide dams* (pp. 479-498). Springer, Berlin, Heidelberg.
- Elyasi, A., Goshtasbi, K., Saeidi, O., Torabi, S.R. (2014). Stress determination and geomechanical stability analysis of an oil well of Iran, Sadhana, *Acad. Proc. Eng. Sci.*, 39(1), 207–220.
- Ermini, L., & Casagli, N. (2003). Prediction of the behavior of landslide dams using a geomorphological dimensionless index. *Earth Surface Processes and Landforms: The Journal of the British Geomorphological Research Group*, 28(1), 31-47.
- Etzelmüller, B., & Sulebak, J. R. (2000). Developments in the use of digital elevation models in periglacial geomorphology and glaciology. *Physische Geographie*, 41, 35-58.
- Evans, S. G., Delaney, K. B., Hermanns, R. L., Strom, A., & Scarascia-Mugnozza, G. (2011). The formation and behavior of natural and artificial rockslide dams; implications for engineering performance and hazard management. In *Natural and artificial rockslide dams* (pp. 1-75). Springer, Berlin, Heidelberg.
- Fan, X., van Westen, C. J., Xu, Q., Gorum, T., & Dai, F. (2012). Analysis of landslide dams induced by the 2008 Wenchuan earthquake. *Journal of Asian Earth Sciences*, 57, 25-37.
- Fan, X., Tang, C. X., Van Westen, C. J., & Alkema, D. (2012). Simulating dam-breach flood scenarios of the Tangjiashan landslide dam induced by the Wenchuan Earthquake. *Natural hazards and earth system sciences*, 12(10), 3031.
- Fan, X., van Westen, C. J., Korup, O., Gorum, T., Xu, Q., Dai, F., & Wang, G. (2012). Transient water and sediment storage of the decaying landslide dams induced by the 2008 Wenchuan earthquake, China. *Geomorphology*, 171, 58-68.

- Fan, X., van Westen, C. J., Xu, Q., Gorum, T., Dai, F., Wang, G., & Huang, R. (2013). Spatial distribution of landslide dams triggered by the 2008 Wenchuan earthquake. In *Landslide science and practice* (pp. 279-285). Springer, Berlin, Heidelberg.
- Fan, X., Rossiter, D. G., van Westen, C. J., Xu, Q., & Görüm, T. (2014). Empirical prediction of coseismic landslide dam formation. *Earth Surface Processes and Landforms*, 39(14), 1913-1926.
- Fan, X., Xu, Q., van Westen, C. J., Huang, R., & Tang, R. (2017). Characteristics and classification of landslide dams associated with the 2008 Wenchuan earthquake. *Geoenvironmental Disasters*, 4(1), 12.
- Fasani, G. B., Di Luzio, E., Esposito, C., Martino, S., & Scarascia-Mugnozza, G. (2011). Numerical modelling of Plio-Quaternary slope evolution based on geological constraints: a case study from the Caramanico Valley (Central Apennines, Italy). *Geological Society, London, Special Publications*, 351(1), 201-214.
- Fasani, G. B., Di Luzio, E., Esposito, C., Evans, S. G., & Mugnozza, G. S. (2014). Quaternary, catastrophic rock avalanches in the Central Apennines (Italy): Relationships with inherited tectonic features, gravity-driven deformations and the geodynamic frame. *Geomorphology*, 211, 22-42.
- Gallagher, K. (2012). Uplift, denudation, and their causes and constraints over geological timescales.
- Golonka, J. (2004). Plate tectonic evolution of the southern margin of Eurasia in the Mesozoic and Cenozoic. *Tectonophysics*, 381(1-4), 235-273.
- Harrison, J. V., & Falcon, N. L. (1937). The Saidmarreh landslip, south-west Iran. *Geographical Journal*, 42-47.
- Harrison, J. V., & Falcon, N. L. (1938). An ancient landslip at Saidmarreh in southwestern Iran. *The Journal of Geology*, 46(3, Part 1), 296-309.
- Hermanns, R. L., Folguera, A., Penna, I., Fauqué, L., & Niedermann, S. (2011). Landslide dams in the Central Andes of Argentina (northern Patagonia and the Argentine northwest). In *Natural and artificial rockslide dams* (pp. 147-176). Springer, Berlin, Heidelberg.
- Homke, S., Vergés, J., Garcés, M., Emami, H., Karpuz, R., 2004. Magnetostratigraphy of Miocene-Pliocene Zagros foreland deposits in the front of the Push-e Kush Arc (Lurestan Province, Iran), *Earth Planet. Sci. Lett.*, 225(3-4), 397-410.
- Hungr, O., & Evans, S. G. (2004). Entrainment of debris in rock avalanches: an analysis of a long run-out mechanism. *Geological Society of America Bulletin*, 116(9-10), 1240-1252.
- Hungr, O., Leroueil, S., & Picarelli, L. (2014). The Varnes classification of landslide types, an update. *Landslides*, 11(2), 167-194.
- Jakobsen, V. U., 2016. An empirical approach for determining the evolution and behavior of rockslide dams. Degree (MSc) diss., NTNU.

Jackson, J.A. (1992). Partitioning of Strike-Slip and Convergent Motion between Eurasia and Arabia in Eastern Turkey and the Caucuses, *Journal Geophys. Research*, 97, 12471-12479.

James, G. A., & Wynd, J. G. (1965). Stratigraphic nomenclature of Iranian oil consortium agreement area. *AAPG Bulletin*, 49(12), 2182-2245.

Karwariya, S. K., Tripathi S., & Shiva, S. (2013). Remote sensing and GIS applications in determination of geomorphological mapping of Achanakmar Amarkantak biosphere reserve using multispectral satellite data. *International Journal of Remote Sensing & Geoscience*, 2(4), 44-49.

Kent, P. E. (1966). The transport mechanism in catastrophic rock falls. *The Journal of Geology*, 74(1): 79-83. DOI: 10.1086/627142.

Khoshboresh, A. R. (2013). A study on deformation of tunnels excavated in fractured rocks, Université Laval, First Edition, Quebec, Canada, 139.

Korup O. (2004). Geomorphometric characteristics of New Zealand landslide dams. *Engineering Geology*, 73(1-2):13-35. DOI: 10.1016/j.enggeo.2003.11.003.

Lacombe, O., Grasemann, B., & Simpson, G. (2011). Introduction: geodynamic evolution of the Zagros. *Geological Magazine*, 148(5-6), 689-691.

Lindsay, J. B., & Newman, D. R. (2018). Hyper-scale analysis of surface roughness. *PeerJ Preprints*, 6, e27110v1.

Macleod, J.H. (1970). Kabir Kuh, 1:100000 Geological Map. Iran Oil Operating Companies, Geological Exploration Division, Tehran.

Maghsoudi, M., Sharafi, S., Yamani, M., Moghadam, A., & Zamanzadeh, S. M. (2015). Environmental changes after Kabirkuh landslide and its impact in formation of archaeological sites in Jaydar Lake area. *MATLAB*, 2012. www.mathworks.com (2012/12/31).

McCave, I. E., & Syvitski, J. M. P. (1991). Principles and methods of geological particle size analysis. In: *Principles, Methods and Application of Particle Size Analysis*, J. M. P. Syvitski, 1991, Ed., Cambridge University Press, Cambridge, UK, 3-21.

Moghadam, A., Javan-Mardzadeh, A., Abdolvand, Sh., Ghorbani, H. (2007). *Seymare Archeology Project - Chapter 2*, Research Institute of Cultural Heritage, Handicrafts and Tourism, Archaeological Research Center.

Mouthereau, F., Lacombe, O., & Vergés, J. (2012). Building the Zagros collisional orogen: Timing, strain distribution and the dynamics of Arabia/Eurasia plate convergence, *Tectonophysics*, 532–535, 27–60.

Mustafa, Ö. Z. E. R., & ORHAN, M. (2015). Determination of an appropriate method for dispersion of soil samples in laser diffraction particle size analyses. *International Journal of Computational and Experimental Science and Engineering*, 1(1), 19-25.

- Nash, T. R. (2003). Engineering geological assessment of selected landslide dams formed from the 1929 Murchison and 1968 Inangahua earthquakes. Degree (MSc) diss., University of Canterbury.
- Nash, T., Bell, D., Davies, T., & Nathan, S. (2008). Analysis of the formation and failure of Ram Creek landslide dam, South Island, New Zealand. *New Zealand journal of geology and geophysics*, 51(3), 187-193.
- Nicoletti, P. G., & Sorriso-Valvo, M. (1991). Geomorphic controls of the shape and mobility of rock avalanches. *Geological Society of America Bulletin*, 103(10), 1365-1373.
- Nooryazdan, A., Gobadi, M. (2019). The formation and deterioration landslide lake of Jaydar in south Lorestan province. *Scientific Quarterly Journal of Iranian Association of Engineering Geology*, 11(4), 89-107. (Published in Persian).
- Oberlander, T. M. (1965). *The Zagros streams; a new interpretation of transverse drainage in an orogenic zone*. Syracuse Geographical Series. Syracuse University Press, New York.
- Okeke, A. C. U., & Wang, F. (2016). Hydromechanical constraints on piping failure of landslide dams: an experimental investigation. *Geoenvironmental Disasters*, 3(1), 4.
- Petitta, M., Scarascia Mugnozza, G., Barbieri, M., Bianchi Fasani, G., & Esposito, C. (2010). Hydrodynamic and isotopic investigations for evaluating the mechanisms and amount of groundwater seepage through a rockslide dam. *Hydrological processes*, 24(24), 3510-3520.
- Peng, M., & Zhang, L. M. (2012). Breaching parameters of landslide dams. *Landslides*, 9(1), 13-31.
- Piégay, H. (2016). Quantitative geomorphology. *International Encyclopedia of Geography: People, the Earth, Environment and Technology: People, the Earth, Environment and Technology*, 1-3.
- Pirocchi, A. (1992) Laghi di sbarramento per frana nelle Alpi: tipologia ed evoluzione. *Atti I convegno Nazionale Giovani Ricercatori in Geologia Applicata* 93, 128–136. (Published in Italian).
- Roberts, N. J., & Evans, S. G. (2013). The gigantic Seymareh (Saidmarreh) rock avalanche, Zagros Fold–Thrust Belt, Iran. *Journal of the Geological Society*, 170(4), 685-700.
- Roostai, Sh., Azimi-Rad, S., Mokhtari, D., Hejazi, A., & Yamani, M. (2018). Morphometry of the Seymareh landslide and reconstruction of its landform effects in late Quaternary (Zagros Mountains in Iran). *Hydrogeomorphology*, 4 (16), 119-138. (Published in Persian).
- Ren, Z., Wang, K., Yang, K., Zhou, Z. H., Tang, Y. J., Tian, L., & Xu, Z. M. (2018). The grain size distribution and composition of the Touzhai rock avalanche deposit in Yunnan, China. *Engineering Geology*, 234, 97-111.
- Rouhi, J., Delchiaro, M., Della Seta, M., & Martino, S. (2019). Emplacement kinematics of the Seymareh rock-avalanche debris (Iran) inferred by field and remote surveying. *Italian Journal of Engineering Geology and Environment*, Special Issue 1. DOI: 10.4408/IJEGE.2019-01. S-16

- Ruiz-Carulla, R., Corominas, J., & Mavrouli, O. (2015). A methodology to obtain the block size distribution of fragmental rockfall deposits. *Landslides*, 12(4), 815-825.
- Schilirò, L., Esposito, C., De Blasio, F. V., & Mugnozza, G. S. (2019). Sediment texture in rock avalanche deposits: insights from field and experimental observations. *Landslides*, 1-15.
- Schillaci, C., Braun, A., & Kropáček, J. (2015). 2.4. 2. Terrain analysis and landform recognition. *Geomorphological Techniques (Online Edition)*.
- Shafiei, A., & Dusseault, M. B. (2008, January). Geomechanical properties of a conglomerate from Iran. In *The 42nd US Rock Mechanics Symposium (USRMS)*. American Rock Mechanics Association.
- Sharafi, S. (2016). *The Geoarchaeology of the Saymareh River Basin in the Territory of the Lake Terraces of Holocene Period*. Degree (PhD) diss, University of Tehran. (Published in Persian).
- Shayan, S. (2006). *New Geomorphologic Observation on Dating an Old Grand Landslide, Seimareh (Kabir-Kuh), Zagros Mountains, Southwest Iran*. *The International Journal of Humanities*, 13(1), 71-92.
- Setudehnia, A., Perry, J. T. O. B. (1967). *Dal Parri. 1:100000 Geological Map*. Iran Oil Operating Companies, Geological Exploration Division, Tehran.
- Shoaei, Z., & Ghayoumian, J. (2000). Seymareh landslide, western Iran; One of the world's largest complex landslides. *Landslide News*, 13, 23–27.
- Shoaei, Z. (2014). Mechanism of the giant Seimareh Landslide, Iran, and the longevity of its landslide dams. *Environmental Earth Sciences*, 72(7): 2411-2422. DOI: 10.1007/s12665-014-3150-8.
- Shugar, D. H., & Clague, J. J. (2011). The sedimentology and geomorphology of rock avalanche deposits on glaciers. *Sedimentology*, 58(7), 1762-1783.
- Singer, J. K., Anderson, J. B., Ledbetter, M. T., McCave, I. N., Jones, K. P. N., & Wright, R. (1988). An assessment of analytical techniques for the size analysis of fine-grained sediments. *Journal of Sedimentary Research*, 58(3), 534-543.
- Sparks BW (1986): *Geomorphology*. Longman Group, Essex, UK.
- Stampfli, G. M., & Borel, G. D. (2002). A plate tectonic model for the Paleozoic and Mesozoic constrained by dynamic plate boundaries and restored synthetic oceanic isochrons, *Earth. Planet. Sc. Lett.*, 196(1), 17-33.
- Stefanelli, C. T., Catani, F., & Casagli, N. (2015). Geomorphological investigations on landslide dams. *Geoenvironmental Disasters*, 2(1), 21.
- Stefanelli, C. T., Segoni, S., Casagli, N., & Catani, F. (2016). Geomorphic indexing of landslide dam's evolution. *Engineering geology*, 208, 1-10.
- Stefanelli, C. T., Vilímek, V., Emmer, A., & Catani, F. (2018). Morphological analysis and features of the landslide dams in the Cordillera Blanca, Peru. *Landslides*, 15(3), 507-521.

- Stokes, G. G. (1851). On the effect of the internal friction of fluids on the motion of pendulums (Vol. 9, p. 8). Cambridge: Pitt Press.
- Straumann, R. K., Purves, R. S., Gruber, S., & Hengl, T. (2009). Experiences in developing landform ontologies.
- Summerfield, M. A (1991) Global geomorphology. An introduction to the study of landforms. Longman, Harlow, UK.
- Sundell, K. A., & Fisher, R. V. (1985). Very coarse-grained fragmental rocks: A proposed size classification. *Geology*, 13(10), 692-695.
- Takin, M., Akbari, Y., Macleod, J.H. (1970). Pul-E Dukhtar. 1:100000 Geological Map. Iran Oil Operating Companies, Geological Exploration Division, Tehran.
- Talbot, C. J., Alavi, M. (1996). The past of a future syntaxis across the Zagros, *Geol. Soc. London, Spec Publ.*, 100(1), 89–109.
- Varnes, D. J. (1978). Slope movement types and processes. Special report, 176, 11-3.
- Vassallo, V. (2017). Ruolo dell'assetto geologico e della reologia nell'insacco della frana di Seymareh (Iran), attraverso modellazione geologico tecnica e numerica. Degree (MSc) diss., Sapienza University of Rome. (Published in Italian).
- Swanson, F. J., Oyagi, N., & Tominaga, M. (1986, April). Landslide dams in Japan. In *Landslide dams: processes, risk, and mitigation* (pp. 131-145). ASCE.
- Wang, F., Dai, Z., Okeke, C. A. U., Mitani, Y., & Yang, H. (2018). Experimental study to identify premonitory factors of landslide dam failures. *Engineering Geology*, 232, 123-134.
- Wassmer, P., Schneider, J. L., Pollet, N., & Schmitter-Voirin, C. (2004). Effects of the internal structure of a rock-avalanche dam on the drainage mechanism of its impoundment, Flims sturzstrom and Ilanz paleo-lake, Swiss Alps. *Geomorphology*, 61(1-2), 3-17.
- Watson, A., & Wright, H.E. (1969) The Saidmarreh Landslide, Iran. *United States Contributions to Quaternary Research; Papers Prepared on the Occasion of the VIII Congress of the International Association for Quaternary Research Paris, France*, 123: 115–140. DOI: 10.1130/SPE123-p115.
- Weidinger, J. T., Korup, O., Munack, H., Altenberger, U., Dunning, S. A., Tippelt, G., & Lottermoser, W. (2014). Giant rockslides from the inside. *Earth and Planetary Science Letters*, 389, 62-73.
- Wen, B., Aydin, A., & Duzgoren-Aydin, N. S. (2002). A comparative study of particle size analyses by sieve-hydrometer and laser diffraction methods. *Geotechnical Testing Journal*, 25(4), 434-442.
- Yamani, M., Goorabi, A., & Azimirad S. (2012). Large Saymarreh landslide and lake terraces sequence. *Physical Geography Research Quarterly*, 44(4): 43-60. (Published in Persian).
- Yang, Y., Cao, S. Y., Yang, K. J., & Li, W. P. (2015). Experimental study of breach process of landslide dams by overtopping and its initiation mechanisms. *Journal of Hydrodynamics*, 27(6), 872-883.

- Zhang, J., Guo, Z. X., Cao, S. Y., & Yang, F. G. (2012). Experimental study on scour and erosion of blocked dam. *Water Science and Engineering*, 5(2), 219-229.
- Zhang, M., Yin, Y., & McSaveney, M. (2016). Dynamics of the 2008 earthquake-triggered Wenjiagou Creek rock avalanche, Qingping, Sichuan, China. *Engineering geology*, 200, 75-87.
- Zhou, G. G., Cui, P., Chen, H. Y., Zhu, X. H., Tang, J. B., & Sun, Q. C. (2013). Experimental study on cascading landslide dam failures by upstream flows. *Landslides*, 10(5), 633-643.
- Zhu, X., Peng, J., Jiang, C., & Guo, W. (2019). A Preliminary Study of the Failure Modes and Process of Landslide Dams Due to Upstream Flow. *Water*, 11(6), 1115.

Web Site References

<https://data.irimo.ir/>

<http://irsc.ut.ac.ir/>

<http://sdi.frw.ir/>

<http://wrs.wrm.ir/>

<https://www.amar.org.ir/>

<https://basement.ethz.ch/download/tools/basegrain.html>

Annex A

Table 18 Location of the photos

Figure Number	Latitude	Longitude
6	33° 6'21.79"N	47°41'30.66"E
7	33° 5'39.17"N	47°42'8.91"E
8	33° 5'12.26"N	47°42'24.32"E
9	33° 2'55.06"N	47°36'14.33"E
10	32°59'40.45"N	47°35'51.03"E
11	33° 4'29.80"N	47°39'6.95"E
12	33° 9'26.76"N	47°42'41.65"E
13	33° 5'6.40"N	47°27'8.75"E
14	32°57'43.82"N	47°44'15.51"E
17	33° 2'11.43"N	47°38'39.82"E
18	33° 5'32.92"N	47°34'11.31"E
19	33° 3'17.02"N	47°41'31.75"E
20	33° 4'43.67"N	47°39'4.58"E
21	33° 4'25.06"N	47°36'39.83"E
23	33° 1'11.81"N	47°42'50.56"E
24	33° 0'42.13"N	47°43'58.12"E
25	33° 1'33.72"N	47°41'44.19"E
59A	33° 2'9.49"N	47°37'32.56"E
59B	33° 6'49.51"N	47°43'28.33"E
59C	32°59'55.86"N	47°43'48.23"E
59D	33° 3'5.96"N	47°35'11.85"E

Table 19 Details of the samples

Sample Number	Latitude	Longitude	Weight (gr)	LL	PI	Sand (%)	Gravel (%)	Passing Sieve N. 200	Passing Sieve N.4	Group Symbol
N1	33° 5' 52.576" N	47° 42' 24.828" E	1074.1	42	12	21.4	12.3	66.28	98.21	ML
N2	33° 0' 38.000" N	47° 44' 47.000" E	1093	36.68	10.7	19	18.2	62.77	87.48	ML
N3	33° 3' 34.732" N	47° 43' 27.686" E	—	—	—	—	—	—	—	—
N4	33° 3' 8.297" N	47° 43' 47.314" E	—	—	—	—	—	—	—	—
N5	33° 1' 38.000" N	47° 40' 35.000" E	1117.7	35	8	13	5.7	81.27	99.41	ML
N6	33° 2' 56.963" N	47° 37' 34.412" E	1099.94	30	10	32.2	42.4	25.37	81.55	SC
N7	33° 4' 35.353" N	47° 36' 8.685" E	1197	30.33	4.8	27.8	9.9	62.27	95.00	ML
N8	33° 4' 57.352" N	47° 40' 20.359" E	1160.8	27.65	14	24	34	42.0417	80.87	SC
N9	33° 5' 42.000" N	47° 37' 18.000" E	1062.1	38	9	10.4	10.5	79.16	96.52	ML
N10	33° 5' 45.765" N	47° 37' 45.410" E	—	—	—	—	—	—	—	—
N11	33° 6' 46.855" N	47° 42' 50.322" E	1139.96	31.82	11.9	16.8	33.3	49.90	76.96	SC
N12	33° 4' 28.073" N	47° 42' 37.722" E	1171.46	32.59	6.7	13.9	20.4	65.61	85.21	ML
N13	33° 1' 10.000" N	47° 44' 4.000" E	1011.54	37.26	8.9	7.9	21.4	70.71	83.74	ML
N14	33° 0' 52.988" N	47° 40' 48.385" E	1156.8	50.7	11.3	11.5	51.2	37.31	56.40	SM
N15	33° 0' 55.937" N	47° 43' 10.496" E	1102.1	38.62	7.8	5.3	12.5	82.15	90.57	ML
N16	33° 0' 6.611" N	47° 44' 17.915" E	1160.19	33.13	8.4	11.6	3.4	84.99	98.20	ML
N17	33° 1' 4.360" N	47° 41' 49.461" E	850.9	55	14	1.7	6.5	91.82	94.32	MH
N18	33° 0' 19.592" N	47° 44' 2.199" E	1056.93	32	6	0.8	1.4	97.72	98.64	ML
N19	33° 0' 46.495" N	47° 42' 16.574" E	1162.4	28.52	6.5	14.1	10.6	75.26	94.60	CL-ML

N20	33° 1' 15.000" N	47° 44' 26.000" E	1210.24	42	11	11.5	24.2	64.32	81.29	ML
N21	33° 1' 58.875" N	47° 44' 59.572" E	1221.15	25.71	12	22.7	32.3	45.01	80.27	SC
N22	33° 2' 45.000" N	47° 43' 48.000" E	963.96	36	5.6	19.2	22	58.85	86.18	ML
N23	33° 3' 12.406" N	47° 43' 29.669" E	1140.4	28	10	25.3	36.3	38.14	81.68	SC
N24	33° 4' 44.031" N	47° 43' 16.256" E	1050.75	44	12	18.9	17.7	63.39	88.86	ML
N25	33° 5' 43.691" N	47° 41' 40.982" E	1086.9	35	9.8	7.7	3.5	88.77	98.43	ML
N26	33° 4' 50.000" N	47° 38' 47.000" E	1192.2	37.28	7.6	16.1	32.3	51.63	80.10	ML
N27	33° 4' 37.532" N	47° 38' 29.642" E	1104.09	42.15	15.6	2.9	46.6	50.50	59.21	SM
N28	33° 4' 57.868" N	47° 38' 5.562" E	1126.3	36.3	11.1	9	5.4	85.60	97.39	ML
N29	33° 5' 7.438" N	47° 37' 26.197" E	1233	42.8	15.6	8.3	3.3	88.40	99.27	ML
N30	33° 4' 23.932" N	47° 39' 7.964" E	1146	40.52	11.2	7	34.6	58.45	72.98	ML
N31	33° 6' 52.189" N	47° 38' 49.663" E	1167.3	33.85	10.8	18.1	13.8	68.11	90.49	CL
N32	33° 6' 19.362" N	47° 38' 2.069" E	1072.21	40.96	9.5	9.3	23	67.68	82.83	ML
N33	33° 6' 8.222" N	47° 36' 59.283" E	1055.92	32.8	6.2	10.8	17.8	71.44	88.54	ML
N34	33° 7' 6.091" N	47° 36' 33.226" E	1104.35	35	6.8	13.6	31.2	55.13	76.62	ML
N35	33° 2' 34.555" N	47° 39' 43.696" E	1080.6	46.01	10.5	3.8	3.7	92.52	98.24	ML
N36	33° 2' 23.011" N	47° 39' 15.790" E	1110.71	45	11	10.6	11.4	78.01	93.04	ML
N37	33° 3' 23.541" N	47° 38' 23.956" E	1057.2	46.93	11.4	9.6	10.8	79.54	92.77	ML
N38	33° 4' 37.755" N	47° 36' 51.423" E	939.65	48.5	19.2	2.3	12	85.69	89.18	ML
N39	33° 5' 5.923" N	47° 36' 15.845" E	989.95	50.23	14.5	1.5	3.8	94.65	97.06	MH
N40	33° 5' 27.241" N	47° 35' 39.443" E	1113.7	42.03	13.5	1.6	0	98.43	100.00	ML
N41	33° 6' 13.648" N	47° 34' 54.609" E	1049.3	41.79	9.7	19.8	9.8	70.44	93.40	ML
N42	33° 5' 47.193" N	47° 34' 54.870" E	1127.4	35.52	11.7	7.1	3.7	89.21	97.55	CL
N43	33° 6' 28.072" N	47° 34' 40.966" E	1056.45	36.45	11.2	12.1	10.1	77.80	94.98	ML
N44	33° 1' 45.000" N	47° 43' 32.000" E	1249.6	41.17	13.8	8.1	7.2	84.66	96.88	ML
S45	33° 7' 22.115" N	47° 37' 36.226" E	1062.75	31.54	11.3	10.2	23.5	66.27	83.32	CL
S46	33° 6' 13.671" N	47° 36' 23.068" E	1048.8	31.21	7.02	8.8	6.6	84.57	95.69	ML
S47	33° 3' 56.238" N	47° 35' 36.606" E	1054.77	38	7.8	14.9	26.3	58.76	82.97	ML
S48	33° 3' 5.107" N	47° 36' 59.796" E	883.6	35.01	8.7	20.6	44.1	35.24	76.57	SM
S49	33° 2' 33.191" N	47° 37' 35.947" E	969.87	34.5	9.6	40.6	41.6	47.75	69.47	SM
S50	33° 2' 2.008" N	47° 39' 19.288" E	1080.97	36.77	9.1	18.1	26.1	55.85	86.07	ML
S51	32° 59' 42.437" N	47° 43' 54.999" E	990	44.8	15	9.5	11.2	79.24	95.71	ML
S52	33° 2' 10.058" N	47° 41' 11.784" E	943.3	49.07	17.9	7.3	19	73.68	86.56	ML
S53	33° 2' 57.218" N	47° 41' 35.743" E	1094.98	29.09	7.6	9.1	9.9	80.97	93.70	CL
S54	33° 2' 21.176" N	47° 40' 42.051" E	1101.2	39.67	12.4	4.1	1.6	94.23	99.80	ML
S55	33° 2' 24.763" N	47° 41' 31.678" E	1082.51	40.93	14.3	0.6	1.2	98.23	99.11	ML
S56	33° 2' 58.294" N	47° 40' 8.253" E	1051.52	46.49	17.7	3.6	2.3	94.13	98.54	ML
S57	33° 3' 43.569" N	47° 39' 47.205" E	900.8	48	18	7.8	2.4	89.81	99.15	ML
S58	33° 3' 57.770" N	47° 41' 34.754" E	1130	37.82	11.3	2.3	2.6	95.15	99.41	ML
S59	33° 2' 12.652" N	47° 42' 58.928" E	961.77	42	13.5	10.8	16.4	72.74	88.40	ML
S60	32° 59' 51.120" N	47° 43' 0.810" E	998.66	38.5	12	16.4	29.7	53.94	78.91	ML
S61	33° 0' 4.352" N	47° 41' 58.926" E	1213.81	26.89	1.7	15.5	35.7	48.87	73.88	SM
S62	33° 0' 10.161" N	47° 42' 40.893" E	1059.83	27.8	4.6	17.5	30.5	51.95	80.07	ML
S63	32° 59' 31.032" N	47° 41' 5.764" E	-	-	-	-	-	-	-	-
S64	33° 0' 32.492" N	47° 38' 52.493" E	1076.5	35	12.2	28.6	37.7	33.69	80.79	SC
S65	33° 0' 44.689" N	47° 37' 20.939" E	991.75	40.83	12.3	19.2	32.8	47.98	80.91	SM
S66	33° 2' 27.107" N	47° 34' 33.575" E	1089.01	25	2	16.2	48.9	37.93	68.27	SM
S67	33° 4' 28.073" N	47° 42' 37.722" E	951.76	50.43	14.2	7.4	28.8	63.79	78.00	MH

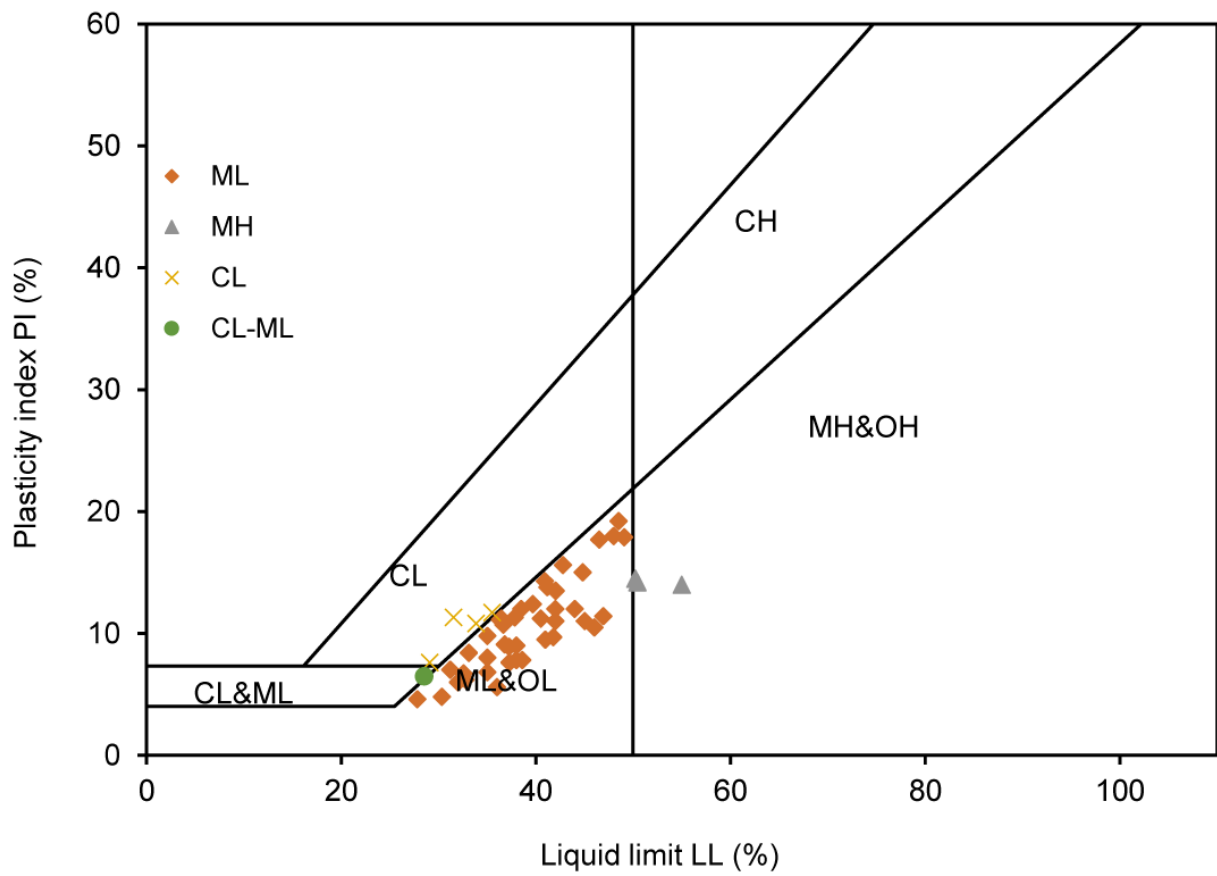


Figure 74 USCS classification of the Fine-Grained samples

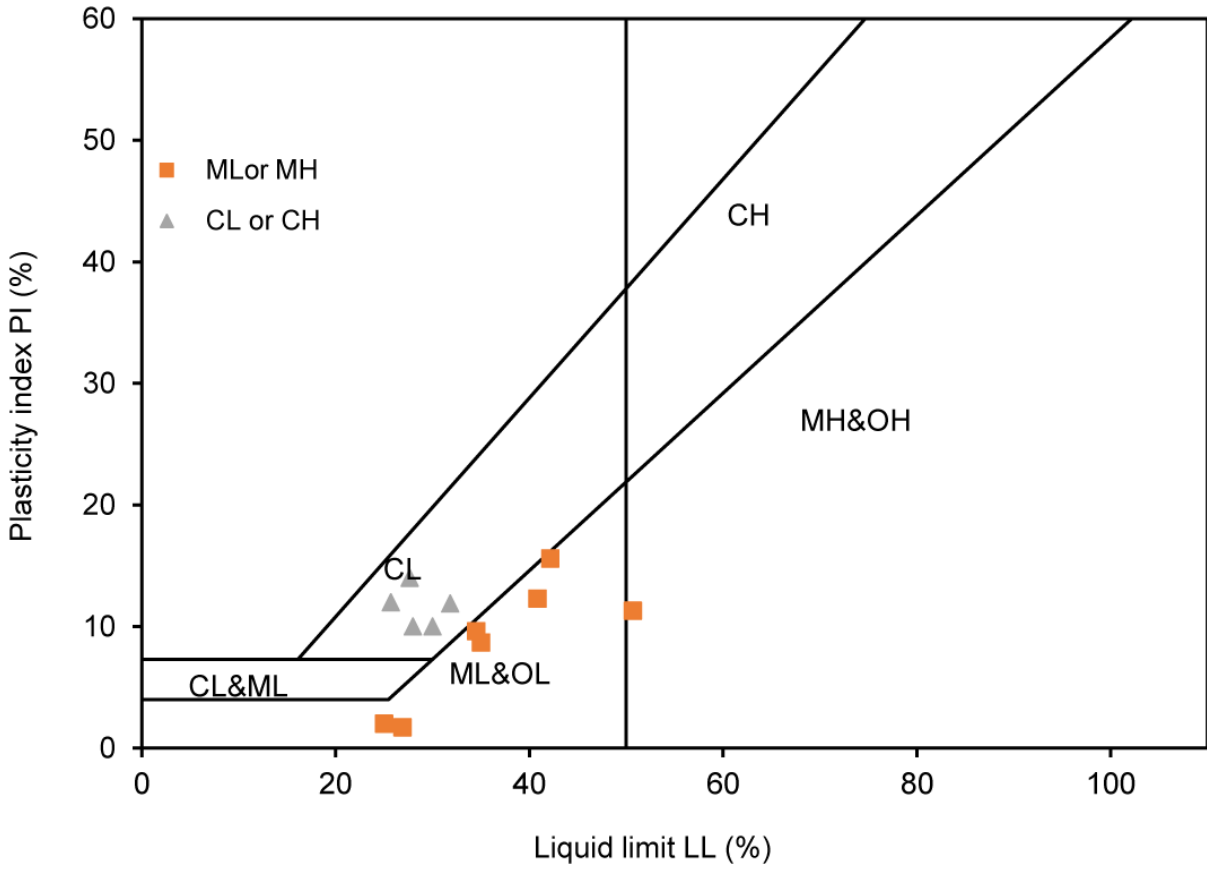


Figure 75 USCS classification of the fine part of the Coarse-Grained samples